

## ABSTRACT

KIM, KYUNGHOON. Understanding Thermal and Spin Transport in Anisotropic Materials (Under the direction of Dr. Jun Liu).

The ever-increasing density of transistors on a microchip with continually shrinking characteristic sizes poses a great challenge to manage the heat. Further improvement of the chip performance now depends on the novel solutions to alleviate the thermal management challenge due to the high-power density. In this dissertation, I focus on one specific structural form of the material – anisotropic materials – to explore whether they can provide a new platform or function to resolve the thermal management issues.

There are two possible strategies to tackle this challenge: (1) spread the heat effectively and direct or guide it to the heat sink; (2) suppress the heat generation. I will first present studies on two different anisotropic materials to explore the possibility of using anisotropic materials as directional heat spreaders. Directional heat spreaders can dissipate the heat more efficiently to the heat sink and protect certain areas simultaneously, which is superior to the isotropic heat spreader in modern designs, especially when the three-dimensionally stacked integrated circuits are employed. I will then present the recent study on how the heat generation can be significantly suppressed by a paradigm shift from the electronics to spintronics, focusing on a specific effect that might transform the information processing using spintronics.

First, I focused on one form of the directional heat spreader – two-dimensional materials. I theoretically studied the two-dimensional layered materials and heterostructures because they are the promising directional heat spreader due to a large bonding and structural anisotropy. I have studied how the topology of disorders would affect thermal conductivity and thermal transport. I found that the most effective mass disorder pattern is the structures with through-

plane and hybrid random mass disorder. I found that the mass pattern, especially the asymmetry of the mass distribution, can play a vital role in thermal transport.

Second, I experimentally explored the thermal transport in another form of the anisotropic materials - polymer fibers. Bulk polymers usually have low thermal conductivity, traditionally viewed as thermal insulators. But their low-dimensional and anisotropic form, polymer fibers, can potentially have very high thermal conductivity compared to the bulk form. Thermal conductivity of a few commercial polymer fibers has been measured in the axial direction. There is also a recent measurement of the strain effect of the thermal conductivity in the radial direction. However, a direct measurement of the anisotropic thermal conductivity of one polymer fiber has not been demonstrated in the literature. I measured the axial and radial thermal conductivity of polyethylene fibers without any deformation to study the influence of the distribution of defects on the thermal conductivity.

Finally, I experimentally studied one effect for spintronics in anisotropic materials in order to transform the current approach for information processing. The current charge-based devices have the limitations for thermal management whereas the electron spin-based devices are promising to overcome these limitations. The spintronic device uses the status of the spins to process information: spin-up (1) and the spin-down (0). A specifically selected hybrid organic-inorganic materials platform is used to experimentally understand the fundamental mechanism of the chiral induced spin selectivity (CISS) effect, which creates polarized spin (up or down) depending on the handedness of organic component. The ultrafast-laser based time-resolved Magneto-Optic Kerr Effect (MOKE) approach is used to measure the time-dependent response of the CISS effect.

© Copyright 2020 by Kyunghoon Kim

All Rights Reserved

Understanding Thermal and Spin Transport in Anisotropic Materials

by  
Kyunghoon Kim

A dissertation submitted to the Graduate Faculty of  
North Carolina State University  
in partial fulfillment of the  
requirements for the degree of  
Doctor of Philosophy

Mechanical Engineering

Raleigh, North Carolina  
2020

APPROVED BY:

---

Dr. Jun Liu  
Committee Chair

---

Dr. Xiaoning Jiang

---

Dr. Yong Zhu

---

Dr. Dali Sun

## **DEDICATION**

Dedicated to my family, who laughed and cried together  
whenever and wherever during my long journey.

## **BIOGRAPHY**

Kyunghoon Kim is currently a Ph.D. candidate in the Department of Mechanical and Aerospace Engineering at North Carolina State University (Raleigh, NC, USA) and has been working at the Nanoscale Thermal Transport Laboratory since 2015.

He earned a B.S. and an M.S. in mechanical and automotive engineering from Kookmin University (Seoul, South Korea) under the guidance of Prof. Jung Kyung Kim. He was a researcher in the Biomedical Device Laboratory (Seoul, South Korea) from 2014 to 2015.

Kyunghoon is interested in the research on thermal and spin transport phenomena in nanomaterials. More specifically, his projects are directly related with a time-domain thermo-reflectance (TDTR) method for the thermal conductivity characterization in nanoscale layered structures and time-resolved opto-magnetic Kerr effect of the electron spin in the inorganic and organic hybrid materials. Moreover, he would like to develop numerical and experimental tools for understanding nanoscale thermal transport with molecular dynamics simulations of thermal transport in 2D materials.

He also would like to bolster his knowledge of mechanical engineering and to innovate new ways of applying engineering techniques to solve industrial and medical problems. He intends to pursue a position as an advanced research scientist in industry or at an educational institution.

Outside of work, he enjoys movies, baseball, and reading. Furthermore, he teaches Korean to students interested in the Korean culture at the regional Catholic Church (Apex, NC, USA) on Friday.

## ACKNOWLEDGMENTS

I still remember the first time when I met with Dr. Liu and sit in the lab. There were only experimental tables and chairs, and me. After five years, a lot of experimental equipment have filled in this space, and here are three desks and chairs with three lab mates. Thus, I suddenly feel that I am in the emotional sea when I write down this part. More than anything else, I would like to express my greatest thanks to Dr. Jun Liu, my advisor. He guides me on my long journey with an unlimited passion, deep insight, and brilliant ideas, and plants the seeds of the enthusiasm and the inspiration for new research topics to me as well.

Next, I give my sincerest gratitude to my committee members, Dr. Xiaoning Jiang, Dr. Yong Zhu, and Dr. Dali Sun, for their faithful encouragement, helpful advice, and insightful discussion about my research based on experience and expertise.

I am very grateful to my labmates in our group, Jixiong He, Yunjian Wu, Banu Ganeshan, Jincheng Yang, Harish Subramanyan, Yangchao Wang, Weiye Zhang, Tingyu Lu, and Ankit Negi, for all their help. We asked each other a lot of questions about the fundamental theories of thermal transport together and fall in the discussion sea to find the answers. Jixiong has shared skillful and technical ideas in the theoretical problems together. Ankit has endured lots of complicated experiments due to experimental obstacles together. I cannot forget these moments: we had been frustrated together when we failed the experiments and had overcome those hurdles together.

I appreciate my collaborators, Dr. Dali Sun and Eric Vetter, for their tremendous experimental support. Eric has prepared all experimental samples, especially the metal deposition, so I cannot do any research without his sample deposition. If there is no advice of the spintronics from Dr. Sun, I could wander around the desert of research without the GPS.

I am also grateful to my friends, Namwoo Joseph Cho, Hyukchan Jung, Dr. Daniel Chin, Dr. Jinwook Kim, Dr. Howuk Kim, and Dr. Taeyang Kim. When I was disappointed and frustrated, they have encouraged me not to give up.

Finally, I thank my family. Their physical and mental dedication and support motivate me to study and research whenever and wherever. I will keep in my mind in my whole life the sentence in the bible:

"Remember that these forty years the LORD your God led you in the wilderness."

## TABLE OF CONTENTS

LIST OF TABLES .....	viii
LIST OF FIGURES .....	ix
<b>Chapter 1: Introductions</b> .....	1
1. Thermal management challenges and two strategies.....	1
2. Thermal transport in anisotropic materials and topology of disorders .....	3
3. Spin transport and topology effect.....	6
4. Objective of the Dissertation .....	9
5. Organization of the Dissertation .....	11
<b>Chapter 2: Theoretical methods and experimental tools</b> .....	13
1. Introductions .....	13
2. Molecular dynamics simulation.....	14
A. Non-equilibrium molecular dynamics (NEMD) method .....	17
B. Equilibrium molecular dynamics (EMD) method.....	20
3. Time-domain thermo-reflectance (TDTR) method .....	20
A. Optical techniques for the thin films with nanoscale thickness .....	20
B. Theoretical model for TDTR.....	25
4. Time-resolved magneto-optical Kerr effect (TR-MOKE) method.....	30
5. Summary .....	32
<b>Chapter 3: Disorder enhanced thermal conductivity anisotropy in 2D materials and van der Waals heterostructures</b> .....	33
1. Introduction.....	33
2. Materials models and computational details.....	35
3. Result and discussions .....	41
A. Thermal conductivity .....	41
B. Thermal anisotropy ratio .....	48
C. Phonon transport analysis.....	48
4. Summary .....	55
<b>Chapter 4: Mass disorder pattern in anisotropic heterostructures</b> .....	57
1. Introduction.....	57
2. Materials models and computational details.....	60
3. Result and discussions .....	61
4. Summary .....	68
<b>Chapter 5: Thermal conductivity of the high modulus polymer fiber along the axial and radial direction</b> .....	69
1. Introduction.....	69
2. Materials and methods .....	70
A. Sample preparation .....	70
B. Time-domain thermo-reflectance (TDTR) method.....	73
3. Data analysis and thermal transport modeling.....	74
4. Results and discussion .....	80

5. Summary .....	82
<b>Chapter 6: Ultrafast spin Current driven by thermally assisted Chirality Induced Spin Selectivity Effect in layered chiral hybrid perovskite .....</b>	<b>83</b>
1. Introduction.....	83
2. Materials and methods .....	86
3. Results and discussion .....	90
A. TDTR signals of the chiral molecules.....	90
B. TR-MOKE signals with the in-plane magnetization.....	91
C. TR-MOKE signals with the in-plane magnetization depending on the laser modulation frequency and the laser heating power .....	95
D. TR-MOKE signals with the 45-degree external magnetic field .....	98
4. Summary .....	105
<b>Chapter 7: Future works.....</b>	<b>107</b>
REFERENCES .....	109
APPENDICES .....	125

## LIST OF TABLES

Table 3.1	Summary of the simulation models with structural or mass disorders, hetero-atom mass, and the calculated thermal anisotropy ratio in our study.....	38
-----------	---	----

## LIST OF FIGURES

Figure 2.1	The schematic of the process about molecular dynamic (MD) simulation.....	16
Figure 2.2	NEMD simulations (a) A general periodic boundary conditions model for the calculation of thermal conductivity of graphene. Red region is heat source areas and blue regions are heat sink area. (b) Temperature distribution in thermal transport simulations. The temperature of original graphene (roughly 140 Angstroms). The black close circle is the average temperature after relaxation from the NEMD simulations, and the dash red line is the fitted slope of the data...	18
Figure 2.3	The schematic of the time domain thermo-reflectance (TDTR) method for thin film materials. The pump and probe beam irradiate the surface of the sample at the same location. ....	21
Figure 2.4	The schematic of the time domain thermo-reflectance (TDTR) method for thin film materials. The pump and probe beam irradiate the surface of the sample at the same location. ....	24
Figure 2.5	The schematic of the time-resolved magneto-optical Kerr effect (TR-MOKE) method for thin film materials. The pump and probe beam irradiate the surface of the sample at the same location. The light green part including all optical components can be inserted in TDTR setup to convert the TR-MOKE set-up.....	31
Figure 3.1	The graphite-like structure models of 2D materials and van der Waals heterostructures. A different color represents a different mass of the hetero atom ( $M_H$ ). (a) Pristine graphite (the atoms in the conventional unit cell are colored green); (b) Turbostratic graphite known as stacking disorder (SD, $\theta = 27.13^\circ$ ); (c) Through-plane mass disorders with one graphene layer and the other layer with heavier mass (TPMD); (d) In-plane superlattice with in-phase pattern (IPSL IP); (e) In-plane superlattice with out-of-phase pattern (IPSL OP); (f) In-plane super lattice with random pattern known as in-plane random alloy (IPRD); (g) Hybrid through-plane random mass disorder (TPRMD); (h) Hybrid graphite with in-plane random alloy (TP+ IPRD); (i) Hybrid graphite with in-plane superlattice (TP+ IPSL). The mass disorders are categorized as the following three types: through-plane disorder (b and c), in-plane disorder (d-f), and hybrid disorder (g-i).....	36
Figure 3.2	The converged thermal conductivity of the pristine graphite. (a) Green-Kubo integration function of thermal conductivity as a function of integral time in the basal plane ( $\Lambda_{xy}$ ) and in the c-axis ( $\Lambda_z$ ). The shaded red and blue areas are the estimated error bar of the integration value in the basal plane and in the c-axis, respectively. (b) Thermal conductivity of the pristine graphite in all directions as a function of in-plane (xy) and c-axis (z) cell sizes. The square is the computed thermal conductivity in the basal plane (the ab-plane), and the circle is that along the c-axis. The shaded red area highlights the converged values.	

	The blue and red symbols are the four and eight unit cells along the z-direction, respectively.....	42
Figure 3.3	Thermal conductivity of graphite-like structures both in the basal-plane and along the c-axis direction. (a) Thermal conductivity of in-plane mass disorder including IP-IP, IP -OP, IPRD, TP+IPRD, and TP+IPSL. The black squares are the thermal conductivity along the x-axis, the red circles are that along the y-axis, and the blue triangles are that along the z-axis. (b) Thermal conductivity of through-plane mass disorder including SD, TPMD, and TPRMD. The number with M means the mass contrast compared with the pristine. The red circles are the computed thermal conductivity in the basal plane (the ab-plane), and the blue triangles are that along the c-axis. ....	44
Figure 3.4	Thermal anisotropy ratio of graphite-like structures. The model ID is defined in Table 1. The in-plane disorders are II- V, the through-plane disorders are VI- IX, and the hybrid disorders are X - XII. To guide the eye, the dash line is the thermal anisotropy ratio for the pristine graphite. ....	47
Figure 3.5	Phonon dispersion of (a) the pristine graphite and the through-plane mass disorder in the $\Gamma$ -K direction (along the ab-plane) (b) in the $\Gamma$ -A direction (along the c-axis). TP 4m and 13m are the through-plane mass disorder structure with hetero atom mass as 4m and 13m, respectively. ....	50
Figure 3.6	Phonon transport analysis for the comparison between pristine graphite and the TPMD graphite with MH=13m along the c-axis. (a) Phonon group velocity $v_g$ , (b) phonon lifetime $\tau_{life}$ , and (c) $v_g^2 \tau_{life}$ . The reduced wavevector K point is from 0.125 to 0.5. Four phonon modes are shown here: transverse acoustic (TA), transverse optical (TO), longitudinal acoustic (LA), and longitudinal optical (LO) modes that are significantly contributed to the thermal conductivity along the c-axis. The pristine graphite is colored by light blue, and the TPMD 13M is light orange. Certain values are too small to show in the plots. ....	54
Figure 4.1	Various mass disorder patterns in the through-plane mass disorder of graphite-like structures. The different mass distribution is following as (a) linear pattern, (b) ramp pattern with the same mass gap each layer, (c) triangle pattern with the same mass gap, (d) random pattern, (e) ramp pattern with the same maximum mass difference, (f) triangle pattern with the same maximum mass difference, (g) exponential difference pattern, (h) error function pattern, (i) damping function pattern, (j) absolute damping function pattern, (k) linear oscillation pattern, and (l) linear trend function, respectively. The mass gap each layer is 1% difference but 0.5% in a red box except for (e) and (f).....	59
Figure 4.2	Thermal conductivity along the z-direction of various mass pattern from (a) to (f). (a) the same mass difference each layer (b) the same maximum mass difference. Light orange, transparent pink, violet is total thermal conductivity, reduction of thermal conductivity, diffuson-related thermal conductivity,	

respectively.....	62
Figure 4.3 Dispersion curves along the z-direction of linear mass pattern depending on the K points: (a) pristine and linear pattern with 1% mass gap, (b) pristine and linear pattern with 4% mass gap. Violet line is the dispersion curve of the pristine graphite with eight layers, orange is that of the linear pattern with 1% mass gap, and the light green is that of the linear pattern with 4% mass gap. ....	64
Figure 4.4 Normalized group velocity along the z-direction of linear graded mass pattern model depending on the mass difference ( $\Delta m$ ). Light green and violet bar is the group velocity and the group velocity squared, respectively. ....	65
Figure 4.5 Various statistical parameters of mass distribution ( $g - l$ ) depending on the thermal conductivity along the z-direction. The light green, light orange, violet line is the various random mass patterns, the linear trend patterns, and additional mass patterns, respectively. ....	67
Figure 5.1 The schematics for the sampler preparation of the polymer fibers. (a) the embedded sample in the epoxy or super-glue, (b) the microtomed surface of the sample embedded in the super-glue (c) the optical image of the sample surface on the CCD camera in TDTR, (d) the aluminum thin film deposited on the sample surface. ....	71
Figure 5.2 The optical image about the microtomed Spectra 900 surface along (a) the axial and (b) the radial on the CCD camera in TDTR. The surface profile of (c) the axial and (d) the radial surface of the sample measured by the confocal laser scanning microscopy. ....	72
Figure 5.3 The schematics for the polymer sample for thermal modeling of TDTR experiments. (a) the cylindrical models for the polymer fiber along the axial direction and (b) Three-dimensional model of the polymer fiber along the radial direction. ....	75
Figure 5.4 The experimental data using TDTR method: (a) Initial time data of the $V_{in-phase}$ measured with 20x objective lens. The arrow indicates the acoustic echo to characterize the aluminum film thickness. (b) Whole-time period of the ratio of $V_{in}$ and $V_{out}$ , $-V_{in} / V_{out}$ . A black circle and red line is the experimental data for the Spectra 900 along the axial direction and the theoretical model, respectively. The arrow indicates the zero-order Lamb mode of the aluminum transducer at 600 ps for a 20x objective lens. ....	78
Figure 5.5 The TDTR measurement results: (a) the initial time delay-dependent thermal conductivity of the Spectra 900 along the axial direction using the TDTR method with 20x objective lens. The x axis is the initial time for the fitting, the y-axis is the extracted thermal conductivity. A green light, violet, yellow, orange, cyan line is the fitted thermal conductivity depending on the modulation	

	frequency of 11.2, 9.8, 7.2, 3.85, 1.82 M Hz, respectively. (b) The frequency-dependent axial thermal conductivity reaching to the constant fitting values. ....	79
Figure 5.6	The modulation frequency-dependent thermal conductivity of the Spectra 900 along the radial direction using the TDTR method with 10x and 20x objective lens. The black and red line is the result with 10x and 20x objective lens, respectively.....	81
Figure 6.1	The schematic of the electron spin. The rotation direction of the spin-down is clockwise along the axis of an electron. The spin's trajectory makes the helix trace depending on the spin states and the propagating direction. The direction of the created effective magnetic field follows the right-hand rule for curve orientation.....	85
Figure 6.2	The schematic of the magnetic precession of the TR-MOKE: The pump heats and creates a temperature gradient along the metallic surface and the chiral samples. The temperature gradient excites the electron flow, and the CISS effect creates the spin current. The spins inject into the metallic firm, and we can monitor the thermally induced spin accumulations using the TR-MOKE method. ....	86
Figure 6.3	The schematic of the chiral molecules and control samples. (a) The chirality of the S-chiral (left-handedness) and R- chiral (right-handedness)- (i) From the de-phased group of spins, the S-chiral selects the down-spin but filters the up-spin, whereas the R-chiral selects the up-spin but filters down-spin. (ii) The $\text{PEA}_2\text{PbI}_4$ with R- and S-phenylethyl ammonium lead iodine (R - $\text{PEA}_2\text{PbI}_4$ and S- $\text{PEA}_2\text{PbI}_4$ ) has magnetic anisotropy along the through-plane. (b) Ni deposited chiral sample on the silicon substrate. (c) Ni deposited the silicon substrate. (d) Cu (100 nm) and Ni (50nm) deposited chiral sample on the silicon substrate. (e) Cu (100 nm) and Ni (50 nm) deposited the silicon substrate. (f) Ni (80 nm) and Cu (10 nm) deposited chiral sample on the silicon substrate. (g) Ni (80 nm) and Cu (10 nm) deposited the silicon substrate. ....	88
Figure 6.4	Contour map derived from the fitting quality of the TDTR data as a function of thermal conductivity and heat capacity. The orange and the green is the thermal conductivity of the R- and the S- chiral sample, respectively.....	91
Figure 6.5	The magnetic precession signals after in-plane magnetization of (a) the nickel deposited chiral samples on the silicon substrate, (b) the copper (100 nm) and nickel (50 nm) deposited chiral samples on the substrate, (c) the nickel (80 nm) and copper (10 nm) deposited chiral samples on the silicon substrate, and (d) the copper (100 nm) and nickel (50 nm) film on the silicon substrate. The measured voltage ( $\mu\text{V}$ ) is the y-axis, and the delay time (ps) is the x-axis. The modulation frequency of the pump laser is 7.2 M Hz. The orange and the green dot line is the R- and S- sample, respectively. ....	93
Figure 6.6	The analysis of the TR-MOKE signals with different power and different	

	frequency of the pulsed pump laser: The power dependence of (a) the amplitude and (b) the frequency of the precession signals with the modulation frequency of 7.2 M Hz. The modulation frequency dependence of (c) the amplitude and (d) the frequency of the precession signals. The light orange colored line is Ni / Cu / Chiral R- chiral samples on the silicon substrate, and the light orange colored line is Ni / Cu / Chiral S- chiral samples on the silicon substrate.....	97
Figure 6.7	The magnetic precession signals of the nickel film on the silicon substrate with (a) the negative magnetic field-dependent signals from 10 to 90 mT and (b) the positive magnetic field-dependent signals from 10 to 90 mT. The pump power is 20 mW, and the probe power is 9 mW in the experiments. The plus and minus symbols indicate the direction of the applied magnetic field. (c) The amplitude of the first oscillation from the signals. (d) The frequency of the oscillation signals. ....	99
Figure 6.8	The time-domain magnetic precession signals of (a) the nickel deposited R-chiral sample on the silicon substrate, (b) the nickel deposited S-chiral sample on the silicon substrate, (c) the nickel and copper deposited R-chiral sample on the silicon substrate, and (d) the nickel and copper deposited S-chiral sample on the silicon substrate applied both the negative and positive 45-degree external magnetic fields from 10 to 90 mT. The pump power is 20 mW, and the probe power is 9 mW in the experiments. The plus (+) and the minus (-) symbols indicate the direction of the applied magnetic field. ....	101
Figure 6.9	The FFT analysis result: The amplitude of (a) the nickel deposited chiral sample and (b) the nickel and copper deposited chiral sample on the silicon substrate. The frequency of (c) the nickel deposited chiral sample and (d) the nickel and copper deposited chiral sample on the silicon substrate. ....	103
Figure 6.10	The 2D contour plot of the amplitude of (a) the nickel deposited R-chiral and (b) S- chiral sample. The 2D contour plot of the signal frequency of (c) the nickel deposited R-chiral and (d) S- chiral sample. The x-axis is the negative and positive 45-degree external magnetic field strength, and the y-axis is the pump laser power. ....	105
Figure A.1	Phonon group velocity of the graphite with the stacking disorder in the (a) ab-plane (b) along the <i>c</i> -axis.....	126
Figure A.2	Group velocity of the pristine graphite and the through-plane mass disorder (13m) (a) in the ab-plane (b) along the <i>c</i> -axis. ....	127
Figure A.3	Frequency-dependent phonon lifetime of the pristine graphite and the through-plane mass disorder (a) in the <i>ab</i> -plane (b) along the <i>c</i> -axis. ....	129

## CHAPTER 1

### 1. Thermal management challenges and two strategies

In modern physics, the knowledge on how to make and control in nanoscale has developed and advanced significantly after Richard Feynman talked the lecture titled “There’s Plenty of Room at the Bottom” on December 29, 1959, in Caltech. Feynman had predicted that the entire 24 volumes of the Encyclopedia Britannica would go into the small pin. A Stanford graduate student had written the opening page of “A Tale Two Cities” on an area 5.9 x 5.9 micrometers and read the contents via an electron microscope. From this, we can start to observe and deal with all the stuff in nanoscale. However, this new world does not follow the classical laws, so there are a lot of questions on how we can bring light to the shade of the complex nanoworld.<sup>1-3</sup>

Why is the nano research special? Because the characteristics of the materials such as the optical, electrical, magnetic properties, melting points, and catalytic reactivity will change when the material size enters into the nanoscale, and this would be useful for the industrial applications.<sup>4,5</sup> Thermal transport in nanoscale is one of the complicated phenomena among these changes. The reader, of course, can have the following questions. Why is the research on the nanoscale thermal transport necessary? To answer that, one example is the thermal management challenges in nanoelectronics because a huge amount of heat will accumulate due to the decrease of the transistor’s size,<sup>3,5</sup> if not properly dissipated, would decrease the performance or even destroy the device. The developed nanotechnology can lead people to invent the complex, high computational, electronic circuits on semiconductors called the integrated circuit.<sup>6</sup> Smaller transistors with a higher packing density can enhance the speed of the computational processing and information transferring in integrated circuit. The integrated

circuit has quickly grown up their performance by following the Moore's laws in the past decades, but researchers face the obstacles to continue to advance them due to the thermal management challenges.<sup>7,8</sup>

The challenges of enhancing its performance come from the limitation of the nano-fabrication process and management of the tremendous heat generation rate due to the extremely dense integrated fine circuit as well.<sup>5,9</sup> To overcome the issue of thermal management when the characteristic size of devices shrinks down, there are two possible strategies:

The first strategy is dissipating heat from the hotspot of transistor to other preferred areas, such as heat sink.<sup>10</sup> This dissipation needs to be in a preferred direction if the hotspots are in three-dimensional space and certain areas need to be protected, such as in the stacked three-dimensional integrated circuits that are currently under development. A directional heat spreader will satisfy this need. Promising materials for the directional heat spreader are anisotropic materials, whose properties have a big contrast among different directions.<sup>11-14</sup> This characteristic is suitable for controlling energy flow efficiently in a designed path.<sup>15</sup> Recently, ultrahigh thermal conductivity in low-dimensional materials has been found and measured.<sup>16-20</sup> According to the recent report, the thermal conductivity of graphene along the in-plane is 3000 - 5300 W m<sup>-1</sup> K<sup>-1</sup>.<sup>21</sup> The opportunities with low-dimensional materials are immense compared with the three-dimensional isotropic bulk materials. The thermal physics of the low-dimensional anisotropic materials is still elusive even though almost all the previous researches have studied various graphite-based materials. Thus, we are motivated to study fundamental thermal transport in anisotropic materials for promising thermal management strategies.

The second strategy is reducing the heat generation rate in nano-electronic devices. Most researchers have studied this by reducing power consumptions such as reducing its electrical

operating parameters<sup>22,23</sup> (voltage, capacitance, and frequency), changing architecture design,<sup>24</sup> and modifying the operation protocol.<sup>25</sup> However, there is a limitation to decrease heat generation because the electronic devices use the charge currents loaded on the circuit. The charge and discharge of the current flow will inevitably induce a considerable amount of heating.<sup>26,27</sup> A new paradigm of the nanoelectronics is necessary to overcome the fundamental issues of these challenges. One of the possible solutions to the challenges of nanoelectronics is to use another important property of electron – spin – to store and process information.<sup>28,29</sup> In electronics, electron flowing through marks as ‘1’ and electron not passing through marks as ‘0’. In spintronics, where spin up and spin down of electrons are utilized as the ‘1’ and ‘0’.<sup>30,31</sup> If a pure spin current, that is current with only one spin polarization, is generated and injected into a ferromagnetic contact, then the spin-transfer-torque (STT) generated in the ferromagnetic contact will store and process the information by reading and writing.<sup>32-36</sup> As a part of this fundamental study, we are interested in studying how to control the spin polarization in multilayered hybrid organic-inorganic anisotropic materials for high-density, fast, low-power memory devices for mass storage of data and fast data processing.

## **2. Thermal transport in anisotropic materials and topology of disorders**

Thermal anisotropy refers to the directional dependence of thermal property, which means that thermal energy in materials can be dissipated differently depending on the directions.<sup>11</sup> When we consider the pristine isotropic crystalline materials or amorphous materials, thermal anisotropy is associated with crystal structures and the directional dependence is usually small.<sup>37,38</sup> When the disorders of materials are arranged in a pattern that the transport has a preferred direction (anisotropic), the directional dependence will be larger. The largest

directional dependence could be from a combination of structural anisotropy and a patterned disorder anisotropy. This would be my focus: low-dimensional materials with patterned disorders.

Low-dimensional materials are attractive for many applications such as optoelectronics,<sup>39,40</sup> thermoelectric devices,<sup>41-43</sup> low power electronics,<sup>44-47</sup> and mechanical sensors.<sup>48-50</sup> Low-dimensional materials have a strong interlayer covalent bonding along with atomic layers, and they are stacked together by weak van der Waals interactions.<sup>51,52</sup> Therefore, they generally have a high thermal conductivity in the bonded direction and a low thermal conductivity in the other direction. If we consider the heterostructure of two-dimensional sheets, we can obtain more variety. Van der Waals heterostructures are the materials consisting of more than two different low-dimensional layers stacked with each other.<sup>52-54</sup> We can regard that there is a topology of mass disorder in the heterostructure because each layer has a different mass along the cross-plane direction.<sup>55-57</sup> If we consider the topology of each layer (mass disorder), this topology could affect the atomic vibrational behaviors, which determine the thermal transport.<sup>58</sup>

The topology of defects and disorders plays a vital role in the material properties.<sup>59-62</sup> Disorders and defects that naturally exist usually reduce thermal conductivity but are recently found to enhance the thermal anisotropy ratio under certain conditions. For example, the lithiated graphite shows the anisotropy can be enhanced twice from the pristine graphite in both molecular dynamics simulations and experiments.<sup>63</sup> Stacking disorders with the rotational alignment in graphite (moiré pattern) can enhance the thermal conductivity anisotropy ratio, which is revealed using the first-principle method.<sup>64</sup> Although researchers have studied the thermal transport in

superlattice heterostructures, the thermal physics in heterostructure layers with disorder patterns remains unknown. This will be my first focus with details in Chapter 3 and 4.

The other focus in this topic is the thermal transport in polymer fibers, which is another type of anisotropic materials with disorders.<sup>65</sup> Polymers are widely used for industrial applications because they are lightweight, corrosion-resistant, stable, shape modifiable, non-toxic, and inexpensive.<sup>66</sup> We apply polymers in applications such as flexible devices,<sup>67</sup> medical-based materials,<sup>68,69</sup> drug delivery,<sup>70-72</sup> and textile.<sup>73,74</sup> The thermal research of polymers is important because the thermal stability is affected by local heat accumulation.<sup>75</sup> The bulk polymers have low thermal conductivity, but the polymer fibers have high thermal conductivity in the axial direction. The thermal anisotropy ratio in polymer fibers can be utilized in thermal management in flexible devices.

There are several trials to experimentally and theoretically enhance thermal conductivity of polymers for several decades. Polymers can have high thermal conductivity values and can be highly anisotropic materials if their polymer lamella are aligned in the same direction. It has been validated by the simple test that the thermal conductivity increases in the stretching direction with increasing strains. Various theoretical simulations have proved that the thermal conductivity of a single polymer chain is high along the chain direction, which can be larger than  $50 \text{ W m}^{-1}\text{K}^{-1}$ .<sup>76,77</sup> Experimental measurements also support that the thermal conductivity of polymers can be high.<sup>78</sup> Recently, Shen *et al.* reported that thermal conductivity of polyethylene (PE) nanofibers can be on the order of  $100 \text{ W m}^{-1} \text{ K}^{-1}$ .<sup>79</sup> However, the measured thermal conductivity might have high uncertainty due to experimental limitations, which are the sample preparation, analysis techniques, and characterization techniques.

The thermal conductivity of polymer fibers along the axial direction has been studied whereas that along the radial direction is still required and less studied. Wang *et al.*<sup>80</sup> reported that the thermal conductivity of commercial high-density polyethylene (HDPE) fibers such as Dyneema, Spectra 900, and Spectra 2000 are 10 - 25 W m<sup>-1</sup> K<sup>-1</sup> using time-domain thermoreflectance (TDTR) method. We know the thermal conductivity of the microfiber along axial direction but need to measure that in radial direction for thermal anisotropy ratio. Lu and Liu *et al.*<sup>81</sup> have measured thermal conductivity in the radial direction of deformed polymer fibers such as polyethylene (PE), poly(p-phenylene-2,6-benzobisoxazole) (PBO) fibers, and poly(methyl methacrylate) (PMMA) fibers. They have measured the deformed fibers by compression, but it is also necessary to measure the thermal conductivity of polymer fibers in the radial direction without any deformation. Moreover, a study on the thermal physics of how defects and alignment affect the thermal anisotropy in microfibers is still required. Typically in polymer fibers, elongated lamellar regions are connected by inter-lamellar chains that can be viewed as defects for thermal transport.<sup>82</sup> I will focus on how these defects affect the anisotropic thermal transport in polymer fibers. This will be my first focus with details in Chapter 5.

### **3. Spin transport and topology effect**

When we had believed that our world works based on the classical theories, we had used the theories related to the mass and charge of electrons for the information and computation. However, we have realized now that the quantum mechanics is a relatively better description when the length scale approaches atomic scale, we could then utilize electron spin, which is an intrinsic angular momentum of electrons, to process information.<sup>30</sup>

The commercial electronic charge-based device, which uses the binary system with 0 and 1, cannot further reduce heat generation rate because the flowing electrons collide with ions in the semiconductors and conductors, are being scattered, and generate heat.<sup>26,27,83</sup> Instead of this, the spintronic device uses two states of spin rather than the flow of electrical charge that is often carried by electrons, so they can reduce heat generation rate by minimizing the electron flow and scattering.<sup>30,35</sup> The effect of spin on the heat reduction is significant because spin manipulation requires much less energy than charging capacitors. Thus, a new paradigm of nanoelectronics is to study how to generate and manipulate spin properties of electrons, which is called spintronics.<sup>84</sup>

It is challenging to invent new spintronic devices much better than the current charge-based transistors. For example, a practical spin transistor requires that generated spin currents should be polarized effectively at room temperature, to be used as a binary system. A high spin polarization efficiency is required, which is defined as the ratio of the amount of pure polarized spin current to the total amount of electrons in the device.<sup>85</sup>

Practical spintronic devices, such as magneto-resistive heads and magnetic memory, have been invented.<sup>86</sup> The magneto-resistive spin valve is a great example of these devices.<sup>87</sup> The magnetic material's electrical resistance can change between two values depending on the relative alignment of the magnetization in the layers. There is a thin non-magnetic layer between two ferromagnetic (FM) layers. The first FM layer (fixed) conserves a magnetic dipole, but the second FM layer (free) changes a dipole by applying an external magnetic field. The magnetic layers of the device align "up" or "down" depending on an external magnetic field. The memory devices based on magneto-resistive spin-valve had been invented and commercialized, but there are limitations for the development for replacing the current nanoelectronics devices. The

devices cannot be at a smaller size because a ferromagnetic can lose its magnetization at the small size (nanometer size).<sup>88,89</sup> This size limitation for the inorganic and metallic materials pushes researchers to find other materials that can avoid this limitation.

Organic materials, which show magneto-resistance effects, can serve as the dielectric layer in GMR like device.<sup>90</sup> They can be used as a medium transferring spin without the alternation of direction. Topology of the organic materials can be used to design the spin devices. The chirality, which is one of topology, is a geometric property of a materials system like mirror plane. Chiral materials cannot be superposed due to their mirror image-like forms.<sup>91,92</sup> Our two hands could be the simple example. When you see your two hands, they are mirror-symmetric shape and distinguished as well. This characteristic can give significant differences in electrical and optical properties in organic materials. The chiral induced spin selectivity (CISS) effect is the effect that films of chiral organic molecules can act as electron spin filters, which can create polarized spin, at room temperature.<sup>93</sup> Thus, it is a significant advancement to inject spin-polarized current without the magnetic element.

An organic-inorganic hybrid perovskite incorporating chiral organic molecules can be promising for new spintronic devices.<sup>92</sup> The current understanding of how a pure spin current is generated through the CISS effect in these hybrid perovskite materials is still elusive. Thus, I am interested in studying spins generation and transport in multilayered anisotropic hybrid materials with the CISS effect, and I want to reveal the detailed mechanism of the thermal-induced spin transfer in perovskite materials incorporating chiral molecules.

#### 4. Objective of the Dissertation

The objective of this Dissertation is to investigate the thermal and spin transport and utilization in anisotropic materials by simulations and characterization. I have investigated into the following three types of anisotropic materials (1) low-dimensional van der Waals heterostructures, (2) polymer microfibers, and (3) anisotropic organic and inorganic hybrid materials with spin selectivity.

The low-dimensional van der Waals heterostructure consists of atomic layers with strong interlayer covalent bonding stacked together by weak van der Waals interactions.<sup>51,52</sup> Computational simulations are aimed to understand the thermal transport in terms of their configuration of layer topology and microscopic interactions between layers, serving as a supplement to the real experimental strategy to build the anisotropic structures with high anisotropy ratio. I built the graphite-like structures and varied only the mass to create heterostructures with mass disorder both in the in-plane and through-plane directions or rotated the graphene layer to create structural disorder without modifying the other parameters such as the potential, temperature, pressure, and so on. The graphite-like model with well-defined atomic structures and interatomic interactions can capture the features of the real heterostructures, enable fair comparisons among different heterostructures, and provide insights on the design of anisotropic materials.

New simulation approaches beyond the finite element approach are required to study the relationship between the topology of multilayer heterostructures and thermal transport in nanoscale because a classical Fourier's law with continuum theory cannot offer any insight into the molecule interactions in the heterostructures.<sup>2,3</sup> Molecular Dynamics (MD) simulation can provide the equilibrium and transport properties in low-dimensional materials, where the motion

of the molecules follows the Newton's law.<sup>94</sup> Although several experiments and simulations have been done to show the fact tuning the thermal conductivity of the 2D materials and van der Waals heterostructures,<sup>12,17,45,48,56,95-100</sup> we should systemically study the fundamental mechanisms of what kind of disorders and how these disorders would change the thermal anisotropy ratio. We also investigate the dominant factors in the thermal conductivity of materials in the classical limit. For this, we compute the phonon behavior of those graphite-like structures using the lattice dynamics, and then analyze the vibrational velocity trajectory to understand the vibrational molecule behaviors.

To measure the anisotropic thermal conductivity of polymer microfibers, I will choose the suitable method for thermal characterization. There are various methods to measure thermal properties and study fundamental thermal transport such as scanning thermal microscopy,<sup>101</sup> bi-material cantilever,<sup>102</sup> microfabricated platform,<sup>103-105</sup> thermoelectrical method (TET,  $3\omega$ ),<sup>106-111</sup> and optical methods.<sup>107</sup> The optical method is to measure the temperature variation by monitoring the temperature-dependent optical properties (photoacoustic, emittance, absorptance, reflectance, and transmittance).<sup>112-117</sup> In this work, we will use the time-domain thermoreflectance (TDTR) method,<sup>118</sup> with several advantages such as the high spatial resolution and low uncertainties. I normally use the TDTR to measure the properties of various materials such as thin films, multilayers, bulk materials, and their interfaces. It is challenging to measure the thermal conductivity of a single polymer fibers with very high aspect ratio and a small diameter, which is very comparable to a single human hair. I am interested to study the frequency-dependence of the thermal transport caused by the pulsed laser in polymer fibers because the thermal penetration depth can be varied in this way so that different defect distributions and concentrations could be probed.

To investigate the fundamental mechanisms of CISS effect, I will design several sample layer configurations to measure spin accumulation and spin transfer torque from a thermally generated spin current. These configurations are detailed in Chapter 6. I will use time-resolved magneto-optical Kerr effect (TRMOKE).<sup>119</sup> The TDTR can be easily modified to the TR-MOKE method because the optical set-up shares most components, which are both used the pump and probe method. The measured signals can be directly linked to the demagnetization of ferromagnetic materials, spin accumulation on non-magnetic layer, and spin transfer torque on ferromagnetic layer.

## **5. Organization of the Dissertation**

In chapter I, I overview the motivation and objective of this Dissertation for thermal and spin transport in anisotropic materials.

In chapter II, I explain theoretical backgrounds for molecular dynamics for thermal transport and describe the experimental method for TDTR and TR-MOKE.

In chapter III, first, I demonstrate *what kinds* of disorders affect the anisotropic thermal conductivity in van der Waals heterostructures using MD simulations. Secondly, I demonstrate *how* disorders affect the anisotropic thermal conductivity in van der Waals heterostructures. Part of this chapter were published in “Disorder Enhanced Thermal Conductivity Anisotropy in Two-Dimensional Materials and van der Waals Heterostructures,” Kyunghoon Kim, Jixiong He, Bane Ganeshan and Jun Liu, *J. APPL. PHYS.*, 124, 055104(2018).

In chapter IV, I then investigate the effect of mass disorder distribution to thermal transport in van der Waals heterostructures using MD simulations.

In chapter V, I study the anisotropic thermal conductivity of the high-density polyethylene microfibers using the TDTR method and discuss about the challenges in dealing with the data processing due to the lamb mode acoustic signals and other acoustic signals caused by thermal stress in polymer fibers.

In chapter VI, I switch gears to investigate the CISS effect. Here, I demonstrate the mechanism of thermal driven STT using the multilayer configurations. I also show the spin polarizations affected by the CISS effect as a function of the temperature rise governed by the laser power, the geometrical condition of the chiral perovskite film, and the laser modulation frequency.

Finally, chapter VII shows the proposed future work.

## CHAPTER 2

In this chapter, I explained theoretical backgrounds for molecular dynamics for thermal transport and describe the experimental method for TDTR and TR-MOKE. Theoretically, nano thermal transport cannot be simulated by the finite element method because the Fourier's law would not generally work at this scale. The length scale of the thermal diffusion at the nanoscale can be comparable to the mean free path and the wavelength of the heat carriers such as photon, phonon, nanoparticle, and electron. In experiments, I also reviewed the thermal conductivity measurement techniques such as time-domain thermoreflectance (TDTR) method. Finally, I demonstrated the technique to study the spin transport in hybrid organic-inorganic materials, which is the time resolved magneto-optical Kerr effect (TR-MOKE) method.

### 1. Introductions

Reducing the size of matters into nanoscale length scale leads to the drastic changes in the transport properties compared to the bulk materials. Thermal properties also fall into this category. Therefore, both simulation and measurement methods are different from the textbook versions. First, I will briefly review the molecular dynamics (MD) methods to calculate thermal conductivity, which includes two approaches: (1) equilibrium molecular dynamics (EMD) method and (2) non-equilibrium molecular dynamics (NEMD) method. They have several advantages and disadvantages compared with each other, and I will discuss them later. Second, I will introduce the experimental technique I chose to study the thermal transport in the polymer fibers. There are many methods to measure thermal conductivity. The steady-state methods are commonly used for the bulk materials, but this method cannot characterize materials in micro and nanoscales and has large errors because it takes long time to reach the steady-state and it is

challenging to prevent the leakage of heat to surroundings. Transient methods are often used for thermal conductivity characterization, such as the pulsed power method, the hot disk method, the transient plane source (TPS) technique, the transient hot strip, the transient hot wire, and the combination of the base transient with the micro platform form, the laser flash method, the microscale thermoelectrical methods, and optical methods. The optical methods are to measure the temperature variation by monitoring the optical properties related to the processes. In the time-domain thermo-reflectance (TDTR) method,<sup>118</sup> we use the surface reflectivity, thermo-reflectance, to characterize the surface temperature rise and thus the thermal conductivity. I chose TDTR method for several reasons: (1) This method has a high spatial resolution with micrometer range and high temporal resolution with picosecond to nanosecond range. The micrometer spot size can measure very small samples or locally on a sample. The ultrafast nature of the laser also helps to neglect the convective and radiative heat loss. (2) Thermal conductivity of thin film and interfacial thermal conductance between materials can be measured simultaneously. Finally, I would like to introduce the time resolved magneto-optical Kerr effect (TR-MOKE) method<sup>120,121</sup> for the spin-related investigations.

## 2. Molecular dynamics simulation

Molecular Dynamics (MD) simulation treats each atom in materials as an individual particle and updates each particle's position and velocity according to the Newton's law.<sup>122,123</sup> The discrete time steps are used to compute numerically the atomic position and velocity. The system of the molecular dynamics has the  $N$  atoms with  $3N$  position and  $3N$  velocity vectors. The atomic position and velocity based on Newton's laws in MD simulations are written as:

$$x_{i+1} = x_i + \delta_t v_i \quad (2.1)$$

The force exerts on each atom is determined by the surrounding atoms. Based on this idea, the force generated by other atoms can be calculated by a given potential energy function, which can be written as:

$$F = -\Delta U(x) \quad (2.2)$$

where  $x$  is the atomic positions of all atoms, and  $U$  is the potential energy function. The velocities are updated by

$$v_{i+1} = v_i + \delta_t \frac{F(x_i)}{m} \quad (2.3)$$

where  $\delta t$  is the discrete time step,  $v$  is the  $i^{\text{th}}$  atomic velocity,  $F(x_i)$  is the  $i^{\text{th}}$  atomic force,  $m$  is the atomic mass,  $i$  is the index of  $N$  atoms, and  $i = 1, 2, 3, \dots, N$ . We can also calculate the energy of the atomic system using the Hamiltonian equation.

$$H(p_i, r_i) = \sum_{i=1}^N \frac{p_i^2}{2m_i} + U(r_i) \quad (2.3)$$

where  $p_i$  is the  $i^{\text{th}}$  atomic momentum,  $r_i$  is the  $i^{\text{th}}$  atomic position,  $m_i$  is the atomic mass,  $U(r_i)$  is the  $i^{\text{th}}$  atomic potential energy,  $i$  is the index of  $N$  atoms, and  $i = 1, 2, 3, \dots, N$ . The total energy is conserved,  $dH/dt = 0$ .

MD is a statistical method that outputs statistical properties using the atomic motions based on the Newton's law. We can set many microscopic statistical ensembles, which are statistical samples of the entire system. There are various types of ensembles by fixing the values of thermodynamic variable: (1) NVE: micro-canonical ensemble is the state fixing the number of atoms, the system volume, and the total energy in the system. (2) NVT: canonical ensemble is the state fixing the number of atoms, the system volume, and the system temperature. (3) NPT: the isothermal-isobaric ensemble is the state fixing the number of atoms, the system pressure, and the

system temperature. The more information about the other ensemble like  $\mu VT$  can be found from the ref [124].

Figure 2.1 shows the process about molecular dynamic (MD) simulation: (1) I set up the system including the structures with atomic positions and velocities, the boundary conditions, and potential energy. (2) The MD simulation runs under the Newton's law. All information including the positions, velocities, and forces of atoms is updated. (3) I can output after the MD simulations. Outputs are the trajectories, force, energy, temperature, pressure, and other statistical data. Total energy consisting of potential, kinetic, and chemical energy should be conserved.

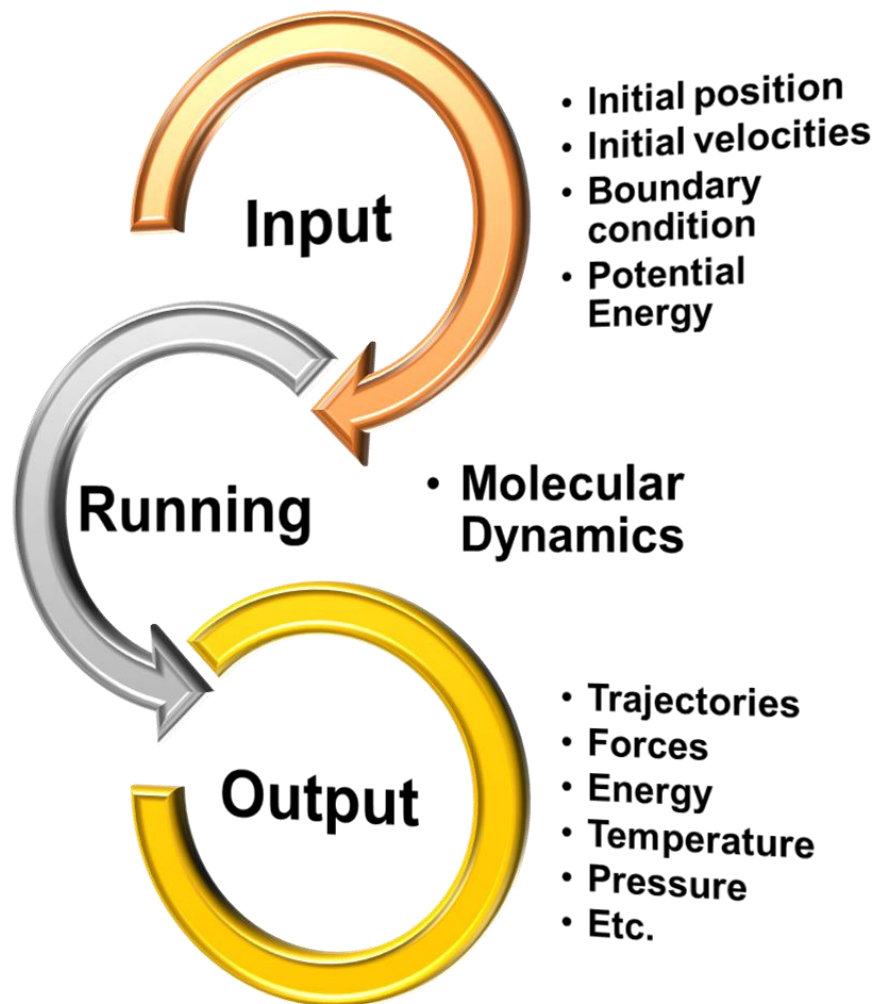


**Figure 2.1.** The schematic of the process about molecular dynamic (MD) simulation.

I chose to use the open-source platform LAMMPS to run MD simulations. In LAMMPS, we can use various potential for materials, which have been developed by other researchers for three decades. In the van der Waals heterostructure work, I will use hybrid potentials to simulate the graphite-like structures, so I introduce the Lennard-Jones (L-J) potential and Tersoff potential<sup>125</sup> here. I used the Tersoff potential for modeling the C-C bond of the in-plane atomic interaction and use the standard Lennard-Jones (LJ) 6-12 potential for modeling the through-plane atomic interactions between each layer. The LJ potential is defined by:<sup>126</sup>

$$V(r_{ij}) = 4\varepsilon \left[ \left( \frac{\sigma}{r_{ij}} \right)^{12} - \left( \frac{\sigma}{r_{ij}} \right)^6 \right] \quad (2.4)$$

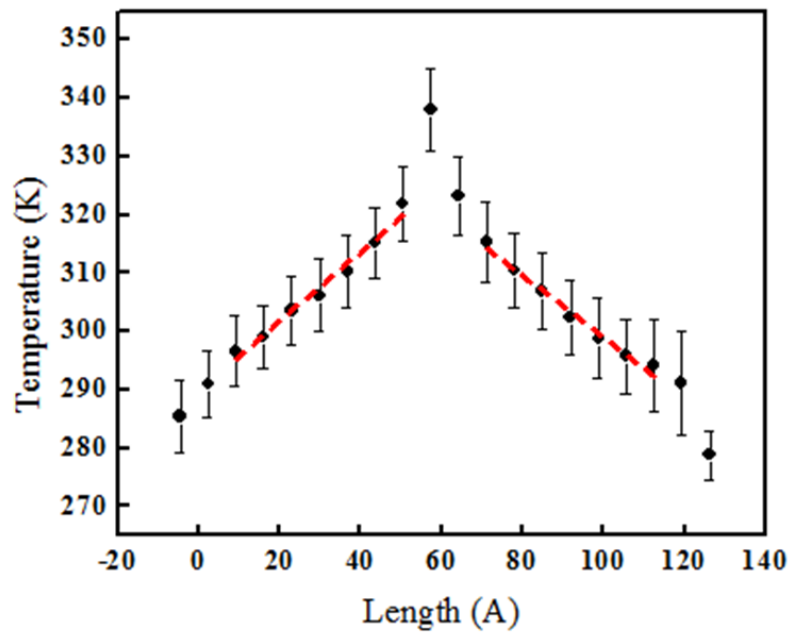
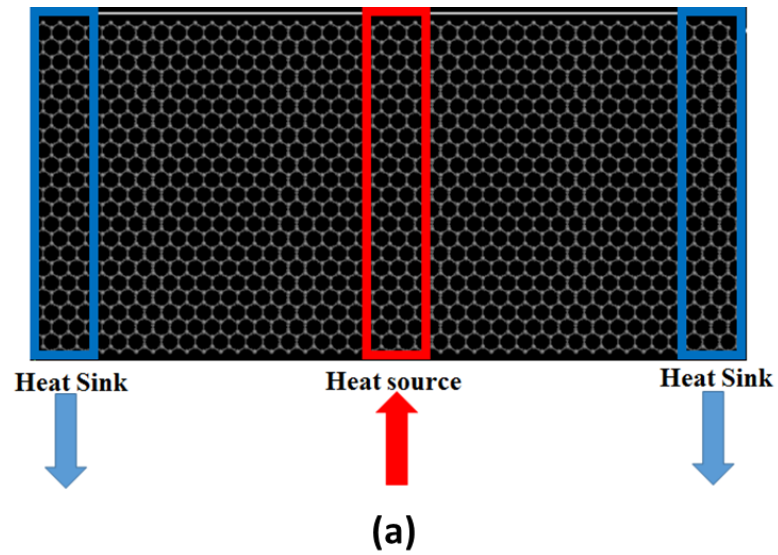
where  $r_{ij}$  is the distance between atoms  $i$  and  $j$ ,  $\sigma$  is the distance where the potential is zero, and  $\varepsilon$  is the potential well depth, which explains the absolute value of the minimum energy.

I have used two different approaches of MD simulations to predict the thermal conductivity: (1) non-equilibrium molecular dynamics (NEMD) method and (2) equilibrium molecular dynamics (EMD) method. The boundary conditions can be applied to the system. There are various boundary conditions such as fixed boundary and periodic boundary condition, so we can apply them into the system.

#### **A. Non-equilibrium molecular dynamics (NEMD) method**

NEMD is very similar to our experiments because we apply a perturbation (external force and flux) to the system, relax the system to be stable, and measure the response. There are several ways applying the perturbation on the system.<sup>94</sup>

We can apply the temperature gradient and the heat flux in the systems steadily or transiently. we used the Langevin heat bath method for anisotropic thermal conductivity. Figure 2.2 shows the simulation model for the calculation of thermal conductivity.



(b)

**Figure 2.2.** NEMD simulations (a) A general periodic boundary conditions model for the calculation of thermal conductivity of graphene. Red region is heat source areas and blue regions are heat sink area. (b) Temperature distribution in thermal transport simulations. The temperature of original graphene (roughly 140 Angstroms). The black close circle is the average temperature after relaxation from the NEMD simulations, and the dash red line is the fitted slope of the data.

We used heat bath method for the calculation of thermal conductivity because it is easier to apply than other method like Muller's perturbation method.<sup>127</sup> In non-equilibrium molecular dynamics (NEMD) simulation, we used the heat bath to set up temperature gradient in the system.

There are two representative approaches for controlling the temperature.<sup>128</sup> Our method is Langevin heat bath which is an example of probabilistic heat bath. The whole system is governed by the equation as:

$$J(x, t) = -\Lambda \nabla T(x, t) \quad (2.5)$$

, where  $\kappa$  is the thermal conductivity of the system. If  $\varepsilon(x, t)$  is represents the local energy density, then this satisfies the continuity equation  $\partial\varepsilon/\partial t + \nabla J = 0$ . We can lead to the heat diffusion equation by using the relation  $\partial\varepsilon/\partial T = c$ , where  $c$  is the specific heat per unit volume:

$$\frac{\partial T(x, t)}{\partial t} = \nabla \left[ \frac{\Lambda}{c} \nabla T(x, t) \right] \quad (2.6)$$

Thus, Fourier's law basically implies diffusive transfer of energy. Using the model in figure 2.2a, we can also lead this term to the simple equation as:

$$\Lambda = \frac{\Delta Q}{2A_{cross} \Delta t} \frac{\Delta z}{\Delta T} \quad (2.7)$$

, where  $\Lambda$  is the thermal conductivity,  $A_{cross}$  is cross-sectional area,  $\Delta T/\Delta z$  is the gradient of temperature distribution and  $\Delta Q/\Delta t$  is heat flux per unit time.

NEMD is commonly used to calculate the interfacial thermal conductance in the system. It directly demonstrates the system response to the applied perturbation, so it is easy to use for large structure and perturbation, and more efficient to calculate the transport coefficient along one direction. However, it has a larger size effect compared to the EMD method, and it has large size effects because of the scattering by the boundaries.

## B. Equilibrium molecular dynamics (EMD) method

The NEMD is used for the interfacial thermal conductance, but the EMD can offers equilibrium state information of the system depending on the discrete time step. Unlike NMED, EMD cannot have any external perturbation, so we should judge the equilibrium system by using the statistical analysis. For this, we can evaluate the thermal transport coefficient in MD by integrating a correlation function depending on time. The thermal conductivity  $\Lambda$  using the Green-Kubo (G-K) relation is written as:

$$\Lambda(\tau) = \frac{V}{k_B T^2} \int_0^\tau \frac{\langle J(\tau)J(0) \rangle}{\langle J(0)J(0) \rangle} d\tau \quad (2.8)$$

where  $\Lambda$  is the thermal conductivity,  $V$  is the material volume of the system,  $k_B$  is the Boltzmann's constant,  $T$  is the temperature,  $J$  is the heat flux, and  $\tau$  is the integration time.  $\langle J(\tau)J(0) \rangle / \langle J(0)J(0) \rangle$  is the normalized heat current auto-correlation functions (HCACF). This concept directly demonstrates the dissipating state consisting of the transport coefficient and differential driving potential for this phenomenon.

EMD simulation can offer thermal conductivity along the three directions. The size effects of the EMD simulations is relatively smaller than that of NEMD, but the computation time is longer than NEMD.

## 3. Time-domain thermo-reflectance (TDTR) method

### A. Optical techniques for the thin films with nanoscale thickness

The time-domain thermo-reflectance (TDTR) technique is a noncontact optical heating and probing method to measure the thermal conductivity and the interfacial thermal conductance of the sample. We can measure the thermal conductivity and the interfacial thermal conductance using the TDTR method with various modulation frequencies.

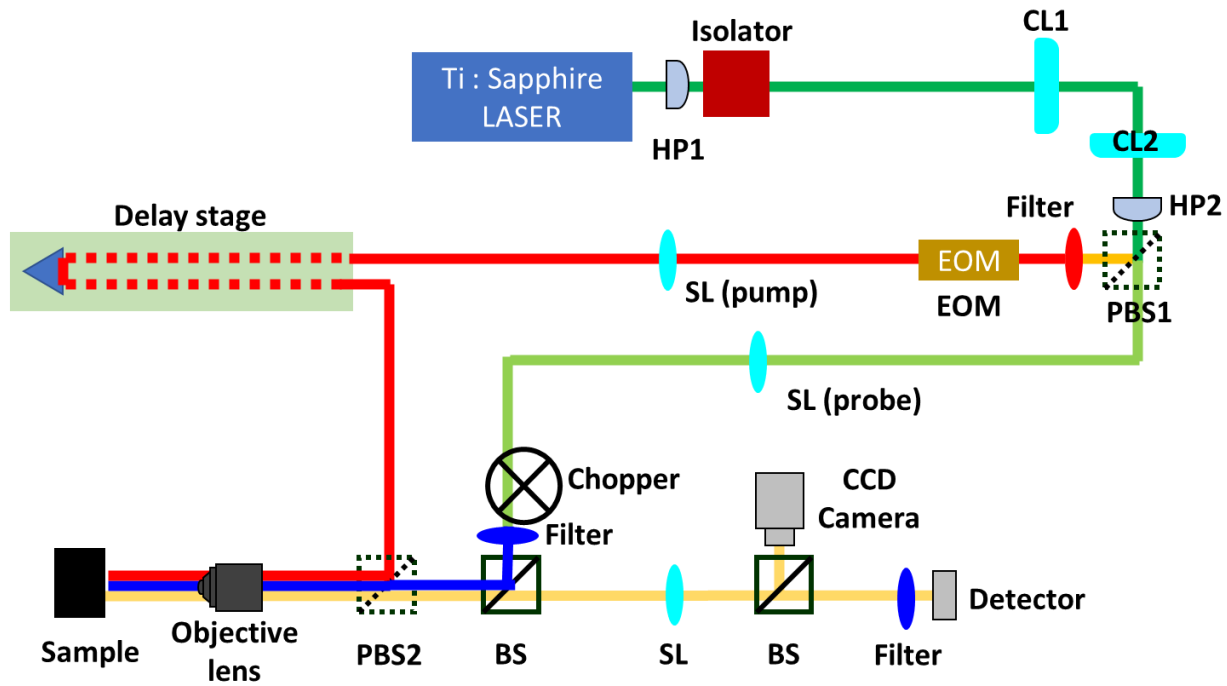


**Figure 2.3.** The schematic of the time domain thermo-reflectance (TDTR) method for thin film materials. The pump and probe beam irradiate the surface of the sample at the same location.

Figure 2.3 shows the schematic of the TDTR method in our lab. TDTR method is essentially a pump-probe method that has two beams: pump beam and probe beam. A Ti:Sapphire Mode-Locked Lasers emit the pulsed laser at a repetition rate of the frequency with 80 M Hz. The beam passes through a half-wave plate and a faraday optical isolator, and we can control the whole beam power of the polarized beam by rotating the wave plate. The beam from another half-wave plate is separated into two beams at the polarized beam splitter, and we can control the ratio of the pump and probe by rotating the second half-wave plate.

We modulate the pulsed pump beam using an electrical optical modulator (EOM) with the modulated frequency, whose controlling signals come from the function generator. The laser beam is a Gaussian beam, so it diverges depending on the distance. The divergence can be measured using the beam profiler. We measured the beam profile from the laser-output head to

several meters. By using this data, we can model how gaussian beam propagates in free space. We should set a certain divergence for making the shape constant and the size of the pump and probe beam nearby the samples by using two vertical and horizontal cylindrical lenses before the polarized beam splitter and one single circular lens after the polarized beam splitter. The reason is that we want to reduce the pump beam shape changes depending on the length modified by the mechanical delay stage. The beam does not follow the perfect divergence trend of the Gaussian beam, so we test the beam shapes. The electro-optic modulator (EOM) can affect the beam divergence, so we also check the divergence after the EOM. We found the proper locations of two cylindrical lenses and a single lens by measuring the all divergence with all optical components such as the cylindrical lens, single lens, and EOM.

The probe beam after the polarized beam splitter passes through the mechanical chopper to eliminate the  $1/f$  noise dominant until several hundred Hertz. The mechanical optical chopper rotates with constant speed and the plate containing several uniform holes, where the frequency of the chopper is 200 Hz.

We align two split beams together after the second polarized beam splitter before beams reach the objective lens. We firstly set the probe beam because the probe does not change its beam path, so it is not only easy to be aligned to be perpendicular to the sample surface but also stable compared to the pump beam. Then we match the alignment of the pump beam based on the probe, and we can easily control the pump beam by using the second polarized beam splitter with the actuators, which can control both horizontally and vertically. In free space, two beams are reflected from the sample surface, which should be sufficiently smooth to reflect perfectly. The reflected beam goes back to the polarized beam splitter, and the pump beam is filtered by the polarized beam splitter because the polarization direction of the pump beam is different from the

second beam splitter. Moreover, the pump beam is secondly filtered by the short pass filter in front of the detector, and we confirm that there is no leakage of the pump in the detector. The reflected probe beam can be focused by the single lens and reach the detector without any disturbance. We install the objective lens to focus the pump and probe beams with the radius of several microns. The beam spot radius with the objective lens with the magnification of 5x, 10x, 20x is 11, 6, 3  $\mu\text{m}$ , respectively.

A pump beam heats the metallic layer up, which can generate the heat and change its thermo-reflectance property depending on the temperature rise, and the other beam, probe, monitors the metallic surface. The reflected probe beam can be captured by the detector, and we can measure the voltage signals, which are proportional to the temperature rise due to thermo-reflectance. ( $\Delta R / R = 1/R (\partial R / \partial T) \Delta T = C_{\text{TR}} \Delta T$ , where the R is the reflectivity and  $\Delta R$  is the reflectivity changes, T is temperature, and  $C_{\text{TR}}$  is the thermo-reflectance coefficient.) The thermo-reflectance coefficient, whose order is from  $10^{-2}/\text{K}$  to  $10^{-5}/\text{K}$ , is the material property related to the illumination wavelength and temperature. The thermo-reflectance phenomena are complicated:<sup>129</sup> (1) Volume thermal expansion decreases the plasma frequency and causes changes in the electron energy bands through changes in the one-electron potential, which cause the Fermi level to shift. (2) Thermal expansion can cause shear strains, which affect the Fermi level due to the energy band changes. (3) The increase of the phonon populations decreases electron relaxation times, which affect the energy bands through the electron-phonon interaction. (4) Temperature changes caused by current flow displaces the distribution function. All the above can change the imaginary parts of the dielectric constant, changing the optical properties.

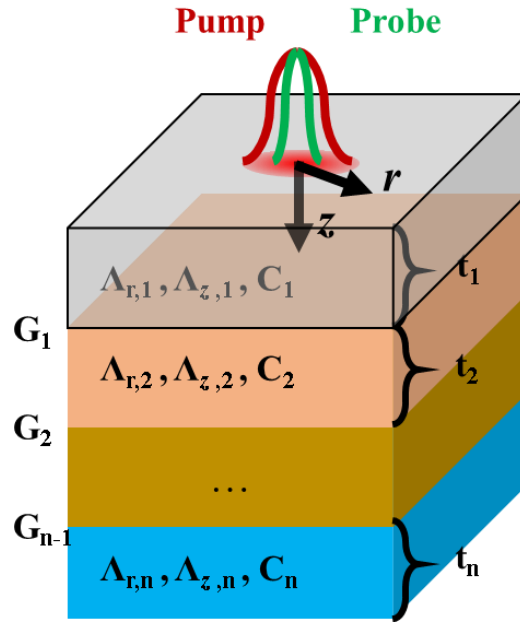


**Figure 2.4.** The schematic of the time domain thermo-reflectance (TDTR) method for thin film materials. The pump and probe beam irradiate the surface of the sample at the same location.

We used the aluminum metallic layer because the thermo-reflectance of the aluminum is a peak value at the wavelength of nearby 800 nm, which is roughly matched to our laser wavelength ( $\sim 785$  nm). The time among the pulsed pump laser with 80 MHz is 12.5 ns, so we can monitor the time-domain thermo-reflectance signals by changing the distance of the pump path through the mechanical delay stages traveling the distance of 600mm (Aerotek, Hanover, MD, USA). We set the exposure time of the detectors is 500 ms, and the average the gained data set at one time points. We scan 100 data linearly from -20 ps to 80 ps to measure the acoustic echo, which can offer us information to judge the thickness of the aluminum film, and then scan 100 data exponentially from 80 ps to 3400 ps. The propagating acoustic strain waves in the materials are shifted to a  $\pi$ -phase depending on the acoustic impedance of the first and second layers. When the impedance of the first layer is lower than that of the second layer, the waves are

$\pi$ -shifted and show the downward signals in the time-domain. When there are opposite configurations, the wave shows a zero-phase shift of the strain wave.

Figure 2.4 shows the schematic of TDTR method for five layers including the metallic film, the thin film and substrate with interface between each material. Samples are usually coated with a metal film like aluminum and tungsten, whose reflectance changes with the temperature rise. The thermal response can then be obtained by monitoring the reflectance change. The time domain thermo-reflectance (TDTR) method measures the thermo-reflectance response as a function of the time delay between the arrival of the probe and the pump pulses at the same location on the sample. The sample heated by the frequency modulated pump laser. The change in the temperature dependent reflectance of the metal transducer is measured by the probe laser delayed in a picosecond to nanosecond time scale.

## B. Theoretical model for TDTR

TDTR method can measure not only the thermal conductivity but also the interfacial thermal conductance, where both are calculated by fitting with the theoretical model.<sup>118,130</sup> The governing equation in cylindrical coordinates for a multilayered system using a quadrupole approach is written as:

$$C \frac{\partial T}{\partial t} = r \frac{\partial T}{\partial r} + r \frac{\partial^2 T}{\partial z^2} \quad (2.9)$$

, where  $\Lambda_r$  is thermal conductivities of the polymer in the radial,  $\Lambda_z$  is that along the axial direction, and C is the volumetric heat capacity. We can rewrite the governing equation by applying the Fourier transform to the time variable and the Hankel transform to the radial coordinate as:

$$\frac{\partial^2 \Theta}{\partial z^2} = \lambda^2 \Theta \quad (2.10)$$

$$\lambda^2 = \left( 4\pi^2 k^2 \frac{\Lambda_r}{\Lambda_z} + \frac{i\omega C}{\Lambda_z} \right) \quad (2.11)$$

where  $\Theta$  is the frequency domain temperature,  $k$  is the Hankel transform variable, and  $\omega$  is the angular frequency. The general solution of equation 2.11 can be expressed as:

$$\Theta = e^{\lambda z} B^+ + e^{-\lambda z} B^- \quad (2.12)$$

where  $B^+$  and  $B^-$  are complex constants to be determined based on the boundary conditions.

According to the Fourier's law, the heat flux can be calculated by the equation  $Q = -\Lambda_z (d\Theta/dz)$ , which can be expressed as:

$$Q = -\Lambda_z \lambda (e^{\lambda z} B^+ - e^{-\lambda z} B^-) \quad (2.13)$$

It can also be re-expressed eqn. 2.12 and 2.13 using a matrix form as:

$$\begin{bmatrix} \Theta \\ Q \end{bmatrix}_{i,z=L} = \begin{bmatrix} 1 & 1 \\ -\Lambda_z \lambda & \Lambda_z \lambda \end{bmatrix} \begin{bmatrix} e^{\lambda L} & 0 \\ 0 & e^{-\lambda L} \end{bmatrix} \begin{bmatrix} B^+ \\ B^- \end{bmatrix} = N_i \begin{bmatrix} B^+ \\ B^- \end{bmatrix}_i \quad (2.14)$$

When  $z = 0$ , we can obtain the constants  $B^+$  and  $B^-$  from the surface temperature and heat flux of that layer. It can be also written as:

$$\begin{bmatrix} B^+ \\ B^- \end{bmatrix}_i = \frac{1}{2\Lambda_z \lambda} \begin{bmatrix} \Lambda_z \lambda & -1 \\ \Lambda_z \lambda & 1 \end{bmatrix} \begin{bmatrix} \Theta \\ Q \end{bmatrix}_{i,z=0} = M_i \begin{bmatrix} \Theta \\ Q \end{bmatrix}_{i,z=0} \quad (2.15)$$

When we consider heat flow across the interface, we can write a matrix to relate the temperature and heat flux at the interface as:

$$\begin{bmatrix} \Theta \\ Q \end{bmatrix}_{i+1,z=0} = \begin{bmatrix} 1 & \frac{-1}{G} \\ 0 & 1 \end{bmatrix} \begin{bmatrix} \Theta \\ Q \end{bmatrix}_{i+1,z=L} = L_i \begin{bmatrix} \Theta \\ Q \end{bmatrix}_{i,z=L} \quad (2.16)$$

where  $G$  is the interfacial thermal conductance between the two layers.

Finally, we can write the temperature and heat flux from top to bottom:

$$\begin{bmatrix} \Theta \\ Q \end{bmatrix}_{i=n, z=L_n} = N_n M_n \dots L_i N_i M_i \dots L_1 N_1 M_1 \begin{bmatrix} \Theta \\ Q \end{bmatrix}_{i=1, z=0} \quad (2.17)$$

$$\begin{bmatrix} \Theta \\ Q \end{bmatrix}_{i=n, z=L_n} = \begin{bmatrix} A & B \\ C & D \end{bmatrix} \begin{bmatrix} \Theta \\ Q \end{bmatrix}_{i=1, z=0} \quad (2.18)$$

When we apply the boundary condition with the bottom of the substrate as a semi-infinite solid,  $Q(z \rightarrow \infty) = 0$ , the equation is  $C \Theta_{i=1, z=0} + D Q_{i=1, z=0} = 0$ . With the Green's function  $\hat{G}(k, \omega)$

$$\hat{G}(k, \omega) = \frac{\Theta_{i=1, z=0}}{Q_{i=1, z=0}} = -\frac{D}{C} \quad (2.19)$$

The boundary condition of top surface is given by the radial heat flux caused by the pulsed laser beam, which has the gaussian distribution. The heat flux of the pump beam is written as:

$$I(r) = \frac{2A_0}{\pi\omega_0^2} \exp\left(\frac{-2r^2}{\omega_0^2}\right) \quad (2.20)$$

, where  $A_0$  is the absorbed power on the metallic layer and  $\omega_0$  is the  $1/e^2$  pump and probe beam diameter, which can be measured by the beam offset.

The temperature response to an impulse of heat can be written as:

$$\begin{aligned} \Theta(\mathbf{r}, t) &= q(t) * h(\mathbf{r}, t) \\ &= \int_{-\infty}^{\infty} q(t') h(\mathbf{r}, t-t') \end{aligned} \quad (2.21)$$

where  $\mathbf{r}$  is the spatial coordinate along the  $\mathbf{r}$ -direction,  $t$  is time,  $Q$  is the heat energy.  $h(\mathbf{r}, t)$  is the unit impulse response.

The heat input is only periodic component because the lock-in amplifier removes the DC component at  $\omega_0$  and can be written as:

$$q(t) = e^{i\omega_0 t} \sum_{n=-\infty}^{\infty} Q \delta(t - nT - t_0) \quad (2.22)$$

where  $t_0$  is the first pulse arrives.

Inserting the intensity of the pulse laser to eqn. 2.22, the heat can be expressed as:

$$q(r, t) = \frac{2A_0}{\pi w_0^2} \exp\left(\frac{-2r^2}{w_0^2}\right) e^{i\omega_0 t} \sum_{n=-\infty}^{\infty} \delta(t - nT_s - t_0) \quad (2.23)$$

where  $T_s$  is a period  $1/f_{\text{rep}}$  (the frequency of the laser repetition).

When we transform the eqn. 23 using the Hankel and Fourier transform,

$$q(k, \omega) = A_0 \exp\left(\frac{-\pi^2 k^2 w_0^2}{2}\right) \omega_s \sum_{n=-\infty}^{\infty} \delta(\omega - n\omega_s - \omega_0) e^{-in\omega_0 t} \quad (2.24)$$

We can combine the surface temperature response with the heat input,

$$\Theta(k, \omega) = q(k, \omega) \hat{G}(k, \omega) \quad (2.25)$$

After this, we can achieve the space domain temperature response using the inverse Hankel transform:

$$\Theta(r, \omega) = \int_{-\infty}^{\infty} q(k, \omega) \hat{G}(k, \omega) J_0(2\pi kr) 2\pi k dk \quad (2.26)$$

We can also consider the periodic probe heating delayed by time  $t_d$  with respect to the pump beam:

$$q(r, t)_{\text{probe}} = \frac{2A_0}{\pi w_0^2} \exp\left(\frac{-2r^2}{w_0^2}\right) \sum_{n=-\infty}^{\infty} \delta(t - nT_s - t_0 - t_d) \quad (2.27)$$

Applying the Fourier transform:

$$q(r, \omega)_{\text{probe}} = \frac{2A_0}{\pi w_0^2} \exp\left(\frac{-2r^2}{w_0^2}\right) \sum_{n=-\infty}^{\infty} \delta(\omega - n\omega_s) e^{-in\omega_0(t_0 + t_d)} \quad (2.28)$$

We can get the average of the temperature distribution using a convolution between the temperature profile and the probe beam profile using eqn. 2.28:

$$\Delta\Theta(\omega) = A_0 \int_0^\infty \delta(\omega - \omega_0) \hat{G}(k, \omega_0 + n\omega_s) \exp(in\omega_s t_d) \exp(-\pi^2 k^2 w_0^2) 2\pi k dk \quad (2.29)$$

Applying the Inverse Fourier transform,

$$\Delta T(t) = e^{i\omega_0 t} \sum_{n=-\infty}^{\infty} A_0 \int_0^\infty \hat{G}(k, \omega_0 + n\omega_s) \exp(-\pi^2 k^2 w_0^2) 2\pi k dk \exp(in\omega_s t_d) \quad (2.30)$$

The temperature response due to the harmonic heating at frequency  $\omega$  is replaced as:

$$\Delta T(\omega) = A_0 \int_0^\infty \hat{G}(k, \omega) \exp(-\pi^2 k^2 w_0^2) 2\pi k dk \quad (2.31)$$

Finally, we can get the temperature response function:

$$\Delta T(t) = e^{i\omega_0 t} \sum_{n=-\infty}^{\infty} \Delta T(\omega_0 + n\omega_s) \exp(in\omega_s t_d) \quad (2.32)$$

When we think about the lock-in amplifier, we can consider the in-phase and out-of-phase components. We can multiply the input signals with two lock-in reference signals with a  $\pi/2$  phase difference at the frequency  $\omega_0$ , and we remove the AC components using low-pass filters. We can get the in-phase and out-of-phase components of the signal at the modulation frequency  $\omega_0$  at a delay time  $t_d$  using the lock-in amplifier. Thus, eqn. 32 can be written as:

$$V_{\text{in-phase}} = \frac{1}{2} \sum_{n=-\infty}^{\infty} [\Delta T(\omega_0 + n\omega_s) + \Delta T(-\omega_0 + n\omega_s)] \exp(in\omega_s t_d) \quad (2.33)$$

$$V_{\text{out-of-phase}} = \frac{1}{2} \sum_{n=-\infty}^{\infty} [\Delta T(\omega_0 + n\omega_s) - \Delta T(-\omega_0 + n\omega_s)] \exp(in\omega_s t_d) \quad (2.34)$$

The in-phase signal  $V_{\text{in-phase}}$  demonstrate the surface temperature difference caused by the pulse heating at the modulation frequency  $\omega_0$  at a delay time  $t_d$ . The out-of-phase signal  $V_{\text{in-phase}}$  comes from accumulation effects due to the pulsed laser heating at the modulation frequency  $\omega_0$ .

Finally, we can get the ratio model to fit the experimental data:

$$Ratio = -\frac{V_{in-phase}}{V_{out-of-phase}} \quad (2.35)$$

The decay rate of  $V_{in-phase}$  is divided by the  $V_{out-of-phase}$ , which represents the heat dissipation on the sample surface considering the heat accumulations effects, can offer us the pure thermal diffusion properties by fitting this with the experimental data. The thermal penetration depth caused by the modulated continuous heating is  $d_p = \sqrt{\Lambda / (\pi f_{mod} C)}$ , where  $\Lambda$  is the thermal conductivity ( $\text{W m}^{-1} \text{K}^{-1}$ ),  $f_{mod}$  is the modulation frequency (Hz), and  $C$  is the volumetric heat capacity ( $\text{J m}^{-3} \text{K}^{-1}$ ) of the sample.

The accuracy of TDTR is typically limited due to uncertainties in several experimental parameters including the metal film thickness and heat capacity of the sample if the film is thick. TDTR also need the very smooth surface of the samples. However, there are many experimental advantages. TDTR does not need for electrical insulation and can separate the metal/film interface thermal conductance from the thermal conductivity. TDTR also has high spatial resolution due to the objective lens and only needs optical access even under these conditions including high pressures, high magnetic fields, and high temperatures.

#### **4. Time-resolved magneto-optical Kerr effect (TR-MOKE) method**

We can utilize a time-resolved magneto-optic Kerr effect (TR-MOKE) method<sup>131</sup> by inserting some optical components into TDTR. TR-MOKE catches the signals of the temperature-dependent transient polar Kerr rotation ( $d\theta/dT$ ), which is the temperature-dependent reflectance changes affected by the magnetic field on the sample surface. By using this, we can detect the temperature response of a magnetic transducer under pump laser heating. TR-MOKE

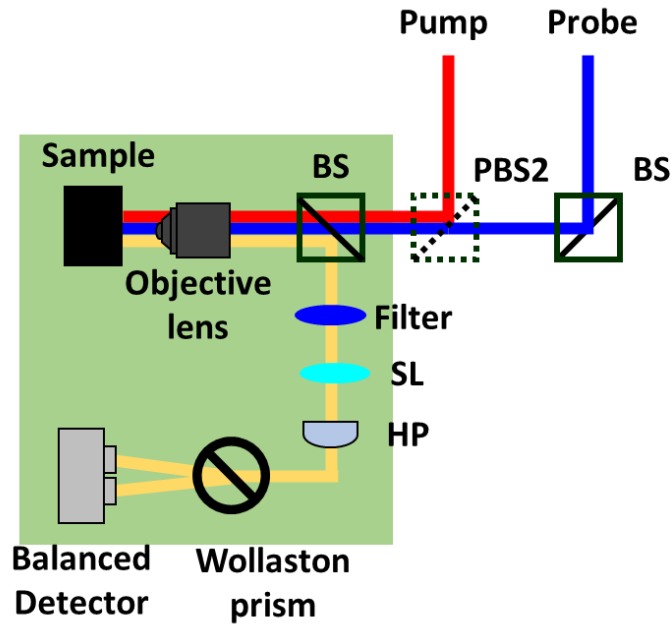


**Figure 2.5.** The schematic of the time-resolved magneto-optical Kerr effect (TR-MOKE) method for thin film materials. The pump and probe beam irradiate the surface of the sample at the same location. The light green part including all optical components can be inserted in TDTR setup to convert the TR-MOKE set-up.

can help us to characterize thin magnetic transducer films, which can be a sample in the TDTR.

Figure 2.5 shows the schematic of the TR-MOKE set-up in our lab. The pump and probe passed from the beam splitter near the objective lens beam irradiate the surface of the sample, and the Faraday effect happens in the sample, and the beam properties changes depending on the magnetic field. Both beams then go back to the beam splitter and are reflected at the beam splitter to the filter. the filter blocks the pump beam but allows the probe beam mass. The beam focused by the single lens is split into two orthogonally polarized components after passing through a half-wave plate and the Wollaston prism. We can control the ratio of two beams by rotating the half-wave plate. The balanced photodetector can acquire two polarized beams.

TR-MOKE signals would change the direction of signals for the magnetization states, which aligned in the opposite direction of the magnetic transducers. We can extract the TR-MOKE in-phase and out-of-phase signals by subtracting the polarized and the other polarized.

$$V_{\text{in-phase}} = V_{\text{in-phase}}^{M^+} - V_{\text{in-phase}}^{M^-} \quad (2.36)$$

$$V_{\text{out-of-phase}} = V_{\text{out-of-phase}}^{M^+} - V_{\text{out-of-phase}}^{M^-} \quad (2.37)$$

We used the TR-MOKE to study spin dynamics and ultrafast magnetization processes. The change of magnetization  $d\mathbf{M}$  is related to the change of the Kerr rotation angle ( $d\theta_K$ ) through the MOKE effect in the polarization state of the reflected probe beam. The voltage signals ( $V$ ) monitored by the TR-MOKE measurement can be expressed as

$$V \propto \frac{R\theta_K}{M_S} \frac{dM}{dT} \quad (2.38)$$

, where  $R$  is the total reflectivity,  $\theta_K$  is the Kerr rotation angle for the magnetic transducer at the saturated magnetization state,  $T$  is the temperature of the sample, and  $M$  and  $M_S$  are the magnetization and saturation magnetization of the magnetic transducer, respectively.

## 5. Summary

In this chapter, I introduced the several computational techniques such as equilibrium molecular dynamics (EMD) method and non-equilibrium molecular dynamics (NEMD) method. I also introduced the experimental techniques, TDTR method, to study the thermal transport in the polymer fibers because of the high accuracy and fine resolutions. Finally, I also briefly introduced the time resolved magneto-optical Kerr effect (TR-MOKE) method for the spin investigations, where we monitor the reflected light varying with the magnetic status of the materials.

## CHAPTER 3

In this chapter, I studied what kinds of disorders affect the anisotropic thermal conductivity in van der Waals heterostructures using MD simulations. Furthermore, I demonstrated how disorders affect the anisotropic thermal conductivity in van der Waals heterostructures.

### 1. Introduction

The two-dimensional (2D) materials and van der Waals heterostructures is the atomic layers with strong interlayer covalent bonding are stacked together by weak van der Waals interactions.<sup>52,132-137</sup> Those layered low-dimensional materials will potentially revolutionize the modern semiconductor industry due to their superior optical, mechanical, thermal, and electronic properties.<sup>135,138-140</sup> While those materials could be integrated into nanoelectronics with high packing density because of their superior properties, they could also naturally become a solution to the thermal management issue by functioning as a directional heat spreader.<sup>41,98,141,142</sup> A directional heat spreader dissipates heat more efficiently in the preferred directions because of a large contrast in thermal conductivities along different orientations.

Due to the highly anisotropic structure of 2D materials and van der Waals heterostructures,<sup>52</sup> their basal-plane or in-plane thermal conductivity,  $\Lambda_{ab}$ , is one or two orders-of-magnitude higher than the through-plane thermal conductivity,  $\Lambda_c$ . We define the thermal anisotropy ratio  $\eta$  as the ratio of basal-plane thermal conductivity to through-plane thermal conductivity.<sup>82</sup> Enhancing the thermal anisotropy ratio of 2D materials and van der Waals heterostructures could further improve the thermal management in nanoelectronics.<sup>41,98,139-142</sup>

Disorders and defects that naturally exist in real materials usually reduce their thermal conductivity.<sup>140</sup> Very counter-intuitively, disorders in low-dimensional materials can sometimes enhance the thermal anisotropy ratio, as recently demonstrated in simulations and experimental work.<sup>57,63,98,132,143-145</sup> Xin *et al.* simulated the lithiated graphite and showed a tunable thermal anisotropy ratio due to the phase transition caused by the lithium ion intercalation.<sup>63</sup> Zhu *et al.* experimentally demonstrated that both basal-plane and through-plane thermal conductivity of molybdenum disulfide can be modified by electrochemical intercalation that leads to the lithiation-induced disorders.<sup>145</sup> These studies on the intercalation inspire us that disorders of certain types can enhance the thermal anisotropy ratio. While intercalation is an active way to tune the thermal anisotropy with a drastic change in cell structure<sup>57,63,143-145</sup>, we seek a passive way to control this ratio. For example, to achieve better performance in electronic properties, a 2D material could have rotational stacking disorder;<sup>146</sup> van der Waals heterostructures would naturally have diverse types of atoms either in the basal-plane direction or the through-plane direction.<sup>135</sup>

We are interested to understand what kind of disorders and how these disorders would change the thermal anisotropy ratio. Examples of disorders include: (1) stacking disorders with the rotational alignment that have been observed in graphite (moiré pattern) and graphene/hexagonal boron nitride (hBN) heterostructures (Hofstadter's butterfly);<sup>54,147-150</sup> (2) in-plane superlattice heterostructures, including the graphene/hBN and 2D transition-metal dichalcogenides (TMDs) (e.g., MoS<sub>2</sub>/MoSe<sub>2</sub>, WSe<sub>2</sub>/MoS<sub>2</sub>, WS<sub>2</sub>/MoS<sub>2</sub>, and MoS<sub>2</sub>/WSe<sub>2</sub>);<sup>151-154</sup> (3) van der Waals heterostructures that can be obtained by mechanical assembly or direct epitaxial growth with a few reported real hetero-bilayers using InSe, MoS<sub>2</sub>, graphene, hBN, WSe<sub>2</sub>, MoSe<sub>2</sub>, and fluorographene.<sup>39,52,95,135,155-157</sup>

In this chapter, we theoretically investigated a series of model 2D materials and van der Waals heterostructures using molecular dynamics (MD) simulations. We systematically built the graphite-like structures and varied only the mass to create heterostructures with mass disorder both in the in-plane and through-plane directions or rotated the graphene layer to create structural disorder. This simple model with well-defined atomic structures and interatomic interactions can capture the features of the real heterostructures, enable fair comparisons among different heterostructures, and provide insights on the design of anisotropic materials. We find that the through-plane thermal conductivity of graphite-like structures can be effectively reduced compared to the pristine graphite by the through-plane, in-plane, and hybrid disorders, thus the thermal anisotropy ratio can be enhanced significantly, especially by the through-plane and hybrid disorders.

## 2. Materials models and computational details

Figure 3.1 shows the representative examples of 2D materials and van der Waals heterostructure models in this work. The unit-cell structures of all the models were constructed by the Virtual Nano Lab (VNL) software.<sup>158</sup> Figure 3.1a shows a rectangular pristine graphite structure (224 carbon atoms) with the conventional cell numbers  $N_x = 7$ ,  $N_y = 4$ ,  $N_z = 1$  in the  $x$ ,  $y$ ,  $z$  directions, respectively. The lattice constant for the  $a$ -axis (along the zig-zag direction) is  $L_a = 2.461 \text{ \AA}$ , and that for the  $c$ -axis is  $L_c = 6.709 \text{ \AA}$ .<sup>159</sup> We chose the cell numbers along the  $a$ -axis and  $b$ -axis so that the side lengths along those two directions are within 1% difference. The graphene layers in graphite have an ABAB stacking pattern, i.e., half of the carbon atoms are exactly below the center of the hexagon in the upper layer while the other half are below a

carbon atom. Figure 3.1b shows the turbostratic graphite with a rotational angle of  $27.13^\circ$  for stacking disorder with rotational alignment.

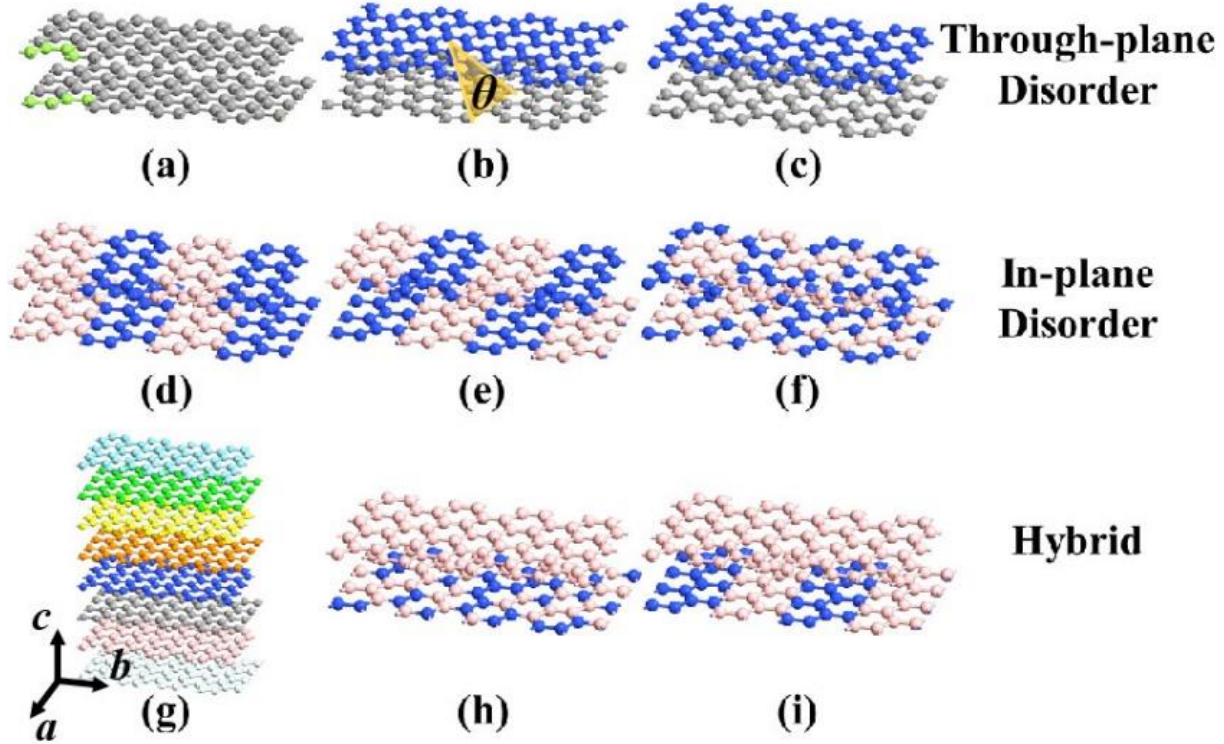


**Figure 3.1.** The graphite-like structure models of 2D materials and van der Waals heterostructures. A different color represents a different mass of the hetero atom (MH). (a) Pristine graphite (the atoms in the conventional unit cell are colored green); (b) Turbostratic graphite known as stacking disorder (SD,  $\theta = 27.13^\circ$ ); (c) Through-plane mass disorders with one graphene layer and the other layer with heavier mass (TPMD); (d) In-plane superlattice with in-phase pattern (IPSL IP); (e) In-plane superlattice with out-of-phase pattern (IPSL OP); (f) In-plane super lattice with random pattern known as in-plane random alloy (IPRD); (g) Hybrid through-plane random mass disorder (TPRMD); (h) Hybrid graphite with in-plane random alloy (TP+ IPRD); (i) Hybrid graphite with in-plane superlattice (TP+ IPSL). The mass disorders are categorized as the following three types: through-plane disorder (b and c), in-plane disorder (d-f), and hybrid disorder (g-i).

This special rotational angle was determined by the minimum energy on the Moiré patterns on graphite.<sup>160</sup> Besides the stacking disorder, we replaced part of the carbon atoms in the unit cell with heavier atoms to create a mass-disordered heterostructure. For simplicity, in this work we assume the mass disorder only changes the mass of atoms, not the interactions among them. This treatment is to ensure the isolation of effects due to the mass disorder only. We use  $m$  to represent the mass of the carbon atom C and use  $M_H$  to calculate the mass of the ‘hetero-atom’ H. Figure 3.1c shows the through-plane mass disorder with alternative carbon and hetero-atom in each entire layer. The different mass ratios  $M_H/m$  (2, 3, 4, or 13) were selected based on the real heterostructures. For example, the mass ratio of graphene/MoS<sub>2</sub> is about 13, that of InSe/MoS<sub>2</sub> is roughly 3, and that of WS<sub>2</sub>/MoS<sub>2</sub> is roughly 2. We used graphite as the base material instead of those real structures to make fair comparisons among structures with various mass ratios. Figure 3.1d-f show the three arrangements in the in-plane mass disorder in this work: (1) in-plane C-H-C-H superlattice (also known as planar superlattice) structure with C-C stacked along the c-axis direction (Figure 3.1d); The periodic length for C atoms or H atoms is  $L_{\text{Periodic}} = 8.525 \text{ \AA}$ , which is twice longer than the standard lattice parameter along a-axis  $L_a$ . The periodic planar superlattice direction is along the y-direction; (2) in-plane C-H-C-H superlattice structure with C-H stacked along the c-axis direction (Figure 3.1e); (3) in-plane random C and H atoms arrangement with half of the atoms as carbon atoms and the other half as the hetero-atoms (Figure 3.1f). We also combined different disorder structures and termed them as hybrid structures. The hybrid structures have the following three types: (1) multiple graphene-like layers with randomly distributed different masses  $M_H$  of the entire layer in the through-plane direction, which is the through-plane mass random disorder (TPRMD) as shown in Figure 3.1g; (2) graphene stacked with layers with in-plane random C and H atoms arrangements (in-plane alloy),

which contains both through-plane mass disorder and in-plane alloy-like random disordered (TPMD + IPRD) in Figure 3.1h; (3) graphene stacked with layers with in-plane superlattice structures in Figure 3.1i.

Table 3.1 summaries the information of each structure model we defined, which includes the model ID, the model definition, the model name abbreviation, the hetero-atom mass, and the calculated thermal anisotropy ratio value. All the materials model structures in our calculations were built from a unit cell and repeated along all the periodic directions. Strictly speaking, those disorders are spatially correlated disorders with the repeated patterns defined in their unit cells rather than a truly uncorrelated type of random disorders.

**Table 3.1.** Summary of the simulation models with structural or mass disorders, hetero-atom mass, and the calculated thermal anisotropy ratio in our study.

<b>ID</b>	<b>Name</b>	<b>Hetero-atom mass, <math>M_H^a</math></b>	<b>Anisotropy ratio, <math>\eta</math></b>
<b>I</b>	Pristine	N/A	187
<b>II</b>	In-plane superlattice out-of-phase (IP -OP 2m)	2m	115
<b>III</b>	In-plane superlattice out-of-phase (IP -OP 4m)	4m	128
<b>IV</b>	In-plane superlattice in-phase (IP -IP 4m)	4m	88
<b>V</b>	In-plane random alloy (IPRD 4m)	4m	2
<b>VI</b>	Stacking disorder (SD)	N/A	269
<b>VII</b>	Through-plane mass disorder (TPMD 2m)	2m	533
<b>VIII</b>	Through-plane mass disorder (TPMD 4m)	4m	560
<b>IX</b>	Through-plane mass disorder (TPMD 13m)	13m	1868
<b>X</b>	Through-plane random mass disorder (TPRMD)	1m ~ 8m	8768
<b>XI</b>	Graphene /random alloy (TP + IPRD)	4m	727
<b>XII</b>	Graphene / in-plane superlattice (TP + IPSL)	4m	562

<sup>a</sup>  $M_H$  is the hetero-atom mass, and m is the atomic mass of the carbon.

All MD simulations were performed using the LAMMPS package.<sup>161</sup> We set the time step as 1 fs and used a hybrid Tersoff and Lennard-Jones (LJ) potential to describe the interactions between atoms. Tersoff potential<sup>162</sup> was used to model the C-C bond for the in-plane atomic interaction, and the standard Lennard-Jones (LJ) 6-12 potential was used to model the through-plane atomic interactions between each layer. The LJ potential is defined by:

$$V(r_{ij}) = 4\epsilon \left[ \left( \frac{\sigma}{r_{ij}} \right)^{12} - \left( \frac{\sigma}{r_{ij}} \right)^6 \right] \quad (3.1)$$

, where  $r_{ij}$  is the distance between atoms  $i$  and  $j$ , and the value of  $\sigma$  and  $\epsilon$  is  $\sigma = 0.335$  nm and  $\epsilon = 4.6616$  meV, respectively.<sup>163</sup>

We built and relaxed the model structures in Figure 3.1 with a two-stage relaxation process: (1) relaxing the  $7 \times 4 \times 1$  graphite cell structures in an isothermal-isobaric (NPT) ensemble first for 2.5 ns, and then a canonical (NVT) ensemble for 1 ns, and finally a microcanonical (NVE) ensemble for 1 ns to reach a stable structure at 300 K and 1 atm; (2) replicating to larger cells (e.g.,  $14 \times 8 \times 2$ ,  $14 \times 8 \times 4$ ,  $14 \times 8 \times 8$ , ...,  $14 \times 8 \times n$  unit cells) and then relaxing them in the NPT, NVT, and NVE ensemble at 300 K for 1 ns, respectively. Such relaxation process was to ensure the proper relaxation due to the lattice expansion. We found this two-stage relaxation process is computationally much faster than directly relaxing the system in those ensembles. We set the change of the system parameters including the volume, the pressure, and the total energy of the simulation cell as the relaxation criteria. This method can relax the structure with a change in pressure within 0.5% and a change of temperature within 0.5%. Furthermore, the relaxed structures were visualized using the Visual Molecular Dynamics (VMD).<sup>164</sup>

The equilibrium molecular dynamics (EMD) method was then conducted to compute the thermal conductivity both in the basal-plane and through-plane directions. The Green-Kubo relation is used to compute the thermal conductivity  $\Lambda$ :

$$\Lambda(\tau) = \frac{V}{k_B T^2} \int_0^\tau \frac{\langle J(\tau)J(0) \rangle}{\langle J(0)J(0) \rangle} d\tau \quad (3.2)$$

, where  $\Lambda$  is the thermal conductivity,  $V$  is the material volume of the system,  $k_B$  is the Boltzmann's constant,  $T$  is the temperature,  $J$  is the heat flux, and  $\tau$  is the integration time.  $\langle J(\tau)J(0) \rangle / \langle J(0)J(0) \rangle$  is the normalized heat current auto-correlation functions (HCACF). Figure 3.2a shows a typical Green-Kubo integrated thermal conductivity from the EMD simulation. For each sample, the NVE simulation time was 10 ns and at least ten samples with different random initial velocities were applied to ensure a meaningful statistical averaging. We checked the appropriate use of integration time so that the integrated thermal conductivity is a converged value and also we do not integrate the noise floor.<sup>165,166</sup> For the basal-plane thermal conductivity, the integrated thermal conductivity usually converges at 50 ps. For the through-plane thermal conductivity, the thermal conductivity converges at short integration times (e.g., 30 ps) but averaging over 50 ps can help eliminate the background noise. The uncertainty of the EMD thermal conductivity results<sup>167</sup>  $\sigma_\Lambda$  is calculated by:

$$\sigma_\Lambda = 2\Lambda_{\text{ave}} \left( N \frac{\tau_{\text{total}}}{\tau} \right)^{-0.5} \quad (3.3)$$

, where  $\Lambda_{\text{ave}}$  is the mean value of the computed thermal conductivities,  $N$  is the number of the simulations,  $\tau_{\text{total}}$  is the total time of the simulations, and  $\tau$  is the integration time of the simulation.

### 3. Result and discussions

#### A. Thermal conductivity

The computed thermal conductivity of pristine graphite along the c-axis is  $\Lambda_c = 7.9 \pm 0.9$  W m<sup>-1</sup> K<sup>-1</sup>, which is within the widespread experimental results (5 - 11 W m<sup>-1</sup> K<sup>-1</sup>),<sup>130,168</sup> while the thermal conductivity in the basal plane is  $\Lambda_{ab} = 1435 \pm 153$  W m<sup>-1</sup> K<sup>-1</sup>, which is slightly lower than the experimental data (~2000 W m<sup>-1</sup> K<sup>-1</sup>) and on the same order with the theoretical results.<sup>130,169</sup>

This difference is not caused by the size effect because we confirmed that the simulation with 14×8×8 conventional unit cells is large enough to extract the converged value. The probable reasons are the inability of the Tersoff potential to accurately describe all the phonon-related properties, and the LJ potential parameters we chose. Even though those discrepancies exist, our results agree reasonably well with other computational results.<sup>63,163,169</sup> For example, using the same potential with Ref. [<sup>170,171</sup>], we were able to repeat the similar in-plane thermal conductivity with the same sample size. We have also checked that the difference is not due to the different time steps.

Figure 3.2a shows the thermal conductivity in the basal plane and along the c-axis converges as a function of integration time at 1485 W m<sup>-1</sup> K<sup>-1</sup> and 7.9 W m<sup>-1</sup> K<sup>-1</sup>, respectively. Both computed values are slightly larger than the values from Ref. [<sup>63</sup>] ( $\Lambda_{xy} = 1232 \pm 161$  W m<sup>-1</sup> K<sup>-1</sup>,  $\Lambda_z = 6.4 \pm 0.5$  W m<sup>-1</sup> K<sup>-1</sup>), and they are within the shaded error bars in Figure 3.2a. The possible reason is that the detailed relaxation procedures influence the lattice constant and total volumes. For example, our relaxed lattice constant for the a-axis and c-axis is  $L_{a, \text{relaxed}} = 2.496$  Å, and  $L_{c, \text{relaxed}} = 6.805$  Å, respectively. Those values are slightly larger than the values from Ref. [<sup>63</sup>] ( $L_{a, \text{ref}} = 2.461$  Å,  $L_{c, \text{ref}} = 6.708$  Å).

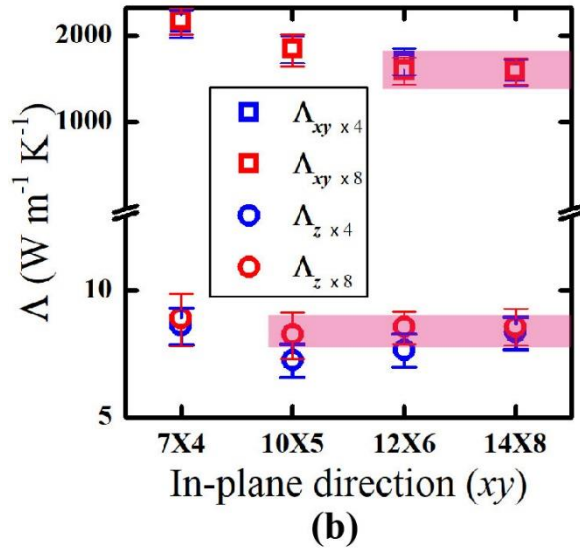
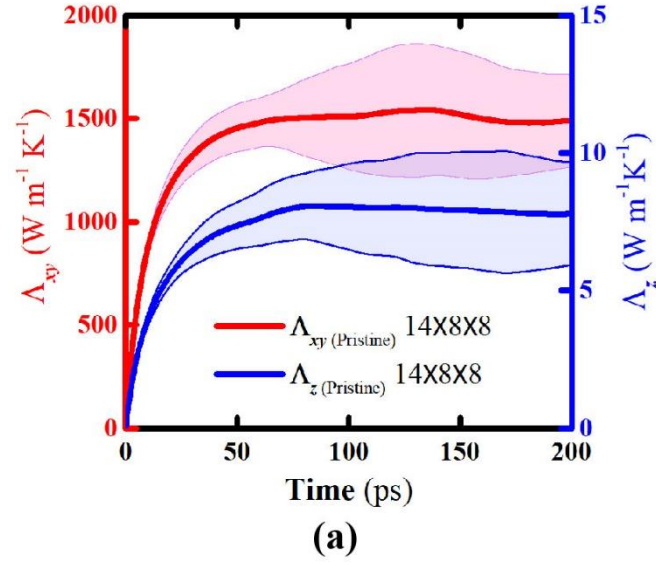


**Figure 3.2.** The converged thermal conductivity of the pristine graphite. (a) Green-Kubo integration function of thermal conductivity as a function of integral time in the basal plane ( $\Lambda_{xy}$ ) and in the  $c$ -axis ( $\Lambda_z$ ). The shaded red and blue areas are the estimated error bar of the integration value in the basal plane and in the  $c$ -axis, respectively. (b) Thermal conductivity of the pristine graphite in all directions as a function of in-plane ( $xy$ ) and  $c$ -axis ( $z$ ) cell sizes. The square is the computed thermal conductivity in the basal plane (the  $ab$ -plane), and the circle is that along the  $c$ -axis. The shaded red area highlights the converged values. The blue and red symbols are the four and eight unit cells along the  $z$ -direction, respectively.

Compared to the experimental results<sup>159</sup> ( $L_{a, \text{exp}} = 2.464 \text{ \AA}$ ,  $L_{c, \text{exp}} = 6.771 \text{ \AA}$ ), the lattice constant for the a-axis is further from the experimental result than the reference, but that for the c-axis is closer to the experimental result. Since our purpose is to study how disorders affect the thermal conductivity of the graphite-like structures and compare with the pristine graphite, our focus is not the accurate prediction of thermal conductivity but the trend and mechanism we can learn from the simple model structures with a self-consistent dataset.

We also calculated different sizes of the cell and confirmed that our reported thermal conductivity values are converged under our simulation parameters. Figure 3.2b shows the convergence test of the thermal conductivity of the pristine graphite in the basal plane and along the c-axis. As the length of simulation cell increases, the thermal conductivity in the basal plane decreases and thermal conductivity along the c-axis increases until reaching the converged values. For example, as the number of unit cells expands in the basal plane, the thermal conductivity in the basal plane decreases from  $>2000 \text{ W m}^{-1} \text{ K}^{-1}$  to  $\sim 1400 \text{ W m}^{-1} \text{ K}^{-1}$ . This observation is the same as shown in the EMD calculations of graphene.<sup>166</sup> Similarly, the thermal conductivity in the basal plane converges at  $\sim 8.0 \text{ W m}^{-1} \text{ K}^{-1}$  with an increasing number of cells. The different trends of the observed size effect might due to the role of long-wavelength phonons. Increasing the simulation domain size will introduce phonons with longer wavelengths to participate in the phonon scattering process. Larger domain size will increase the phonon scattering time for the phonon-boundary scattering whereas decrease the phonon lifetime because of more phonon-phonon scattering. The competition of phonon-boundary scattering and phonon-phonon scattering leads to the different trends on the size effect.

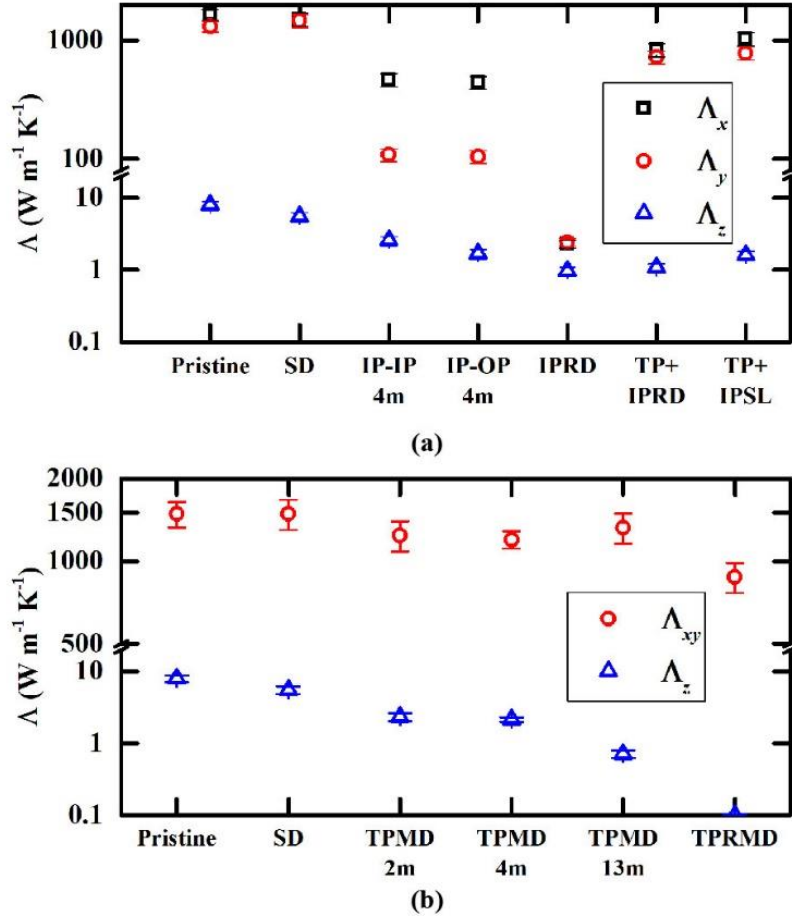


**Figure 3.3.** Thermal conductivity of graphite-like structures both in the basal-plane and along the  $c$ -axis direction. (a) Thermal conductivity of in-plane mass disorder including IP-IP, IP -OP, IPRD, TP+IPRD, and TP+IPSL. The black squares are the thermal conductivity along the  $x$ -axis, the red circles are that along the  $y$ -axis, and the blue triangles are that along the  $z$ -axis. (b) Thermal conductivity of through-plane mass disorder including SD, TPMD, and TPRMD. The number with M means the mass contrast compared with the pristine. The red circles are the computed thermal conductivity in the basal plane (the  $ab$ -plane), and the blue triangles are that along the  $c$ -axis.

Figure 3.3 shows the computed thermal conductivity of all graphite-like models with disorders shown in Figure 3.1 and Table I, both in the basal-plane and along the  $c$ -axis direction. Figure 3.3a shows the thermal conductivity tensor of pristine graphite and structures with in-plane disorders and hybrid disorders (samples I-V, XI, and XII). For the in-plane superlattice

structure (IPSL), both the in-phase (IP) and out-of-phase (OP) stacking structures have a reduced thermal conductivity (>6 times reduction) in the x and y directions compared with pristine graphite. The thermal conductivity in the y-direction (i.e., perpendicular to the planar superlattice interfaces) is lower than that in the x-direction (i.e., parallel to the planar interfaces), which is well understood from the classical size effect in thermal conductivity and change of phonon dispersion due to the planar superlattice structure.<sup>172</sup> The thermal conductivity in the z-direction, along the c-axis, is reduced much less, ~4 times. Comparing the IP-IP and IP-OP structures with the same hetero-atom mass  $MH = 4m$ , we find that the out-of-phase stacking pattern has a similar in-plane thermal conductivity but a 34% lower through-plane thermal conductivity. We also compare the effect of the hetero-atom mass (2m v.s. 4m) and find that a higher mass contrast in the in-plane mass disorder structure reduces thermal conductivity in all directions. For the in-plane random mass disorder (IPRD) structure, which is similar as the in-plane alloy, the in-plane thermal conductivity drops dramatically to the same order of through-plane thermal conductivity, which makes this structure alone not attracting for high thermal anisotropy ratio. Such a randomly distributed mass disorder can effectively scatter the long-wavelength phonons and thus reduce the thermal conductivity.

All the in-plane disorder structures have lower thermal conductivities both in the basal plane and along the c-axis than the pristine graphite. In-plane disorders only, thus, do not promote thermal anisotropy ratio since the in-plane disorders reduce the thermal conductivity more in the in-plane direction than the through-plane direction. Hybrid disorders that combine the in-plane superlattice structures with a perfect graphene layer (e.g., TP + IPRD and TP + IPSL), however, shows the similar thermal conductivity in the basal plane whereas a much lower thermal conductivity along the c-axis. Therefore, TP + IPRD and TP+IPSL structures can

promote their thermal anisotropy ratio because they can preserve the high magnitude of the thermal conductivity in the basal plane due to the existence of the pristine graphene layers between the in-plane mass disordered layers.

Figure 3.3b demonstrates the anisotropic thermal conductivity of the structures with through-plane disorders. The stacking disorder (SD) structure does not change the in-plane thermal conductivity but also brings only a slight decrease (about twice) in the thermal conductivity along the c-axis. This result shows a different conclusion with the prediction using the atomic Green's function method by Mao et al, who indicate a factor of  $>20$  reduction in the through-plane thermal conductivity in randomly stacked turbostratic graphitic structures.<sup>64</sup> Our stacking disorder structure with only one stacking angle is more ordered than a completely random stacked structure so we expect the reduction should be less than theirs. In addition, the discrepancy might be due to very different interatomic force descriptions and calculation methods. For example, the atomic Green's function method does not contain the anharmonic phonon scattering whereas MD includes all types of phonon scattering.<sup>173</sup>

For the through-plane mass disorder (TPMD) structures, the thermal conductivity in the basal plane decreases only slightly but the through-plane thermal conductivity decreases remarkably compared with the pristine graphite. Moreover, when the ratio of the mass contrast increases from 2 to 13, the through-plane thermal conductivity decreases monotonously from  $2.3 \text{ W m}^{-1}\text{K}^{-1}$  to  $0.7 \text{ W m}^{-1}\text{K}^{-1}$  with an almost unchanged thermal conductivity in the basal-plane direction. Similarly, as in the in-plane disorder structure case, a hybrid through-plane mass disorder, i.e., through-plane random mass disorder (TPRMD), can further decrease the through-plane thermal conductivity about a factor of  $\sim 10$  without significantly changing the in-plane thermal conductivity.

When we computed the thermal conductivity of the TPRMD using the EMD simulations, we found that obtaining the accurate averaged thermal conductivity value from the EMD integration of heat current autocorrelation is very challenging for the ultra-low thermal conductivity ( $<0.3 \text{ W m}^{-1}\text{K}^{-1}$ ) since the noise floor and oscillation of the heat current autocorrelation is large. Here, we preprocessed the raw data using the locally weighted scatterplot smoothing (LOWESS) method to make the raw data smooth and extracted the mean value of the thermal conductivity. When we compute the extremely low thermal conductivity ( $<0.3 \text{ W m}^{-1}\text{K}^{-1}$ ), we can only identify an upper limit. For example, we report thermal conductivity of the TPRMD is  $<0.1 \text{ W m}^{-1}\text{K}^{-1}$ .

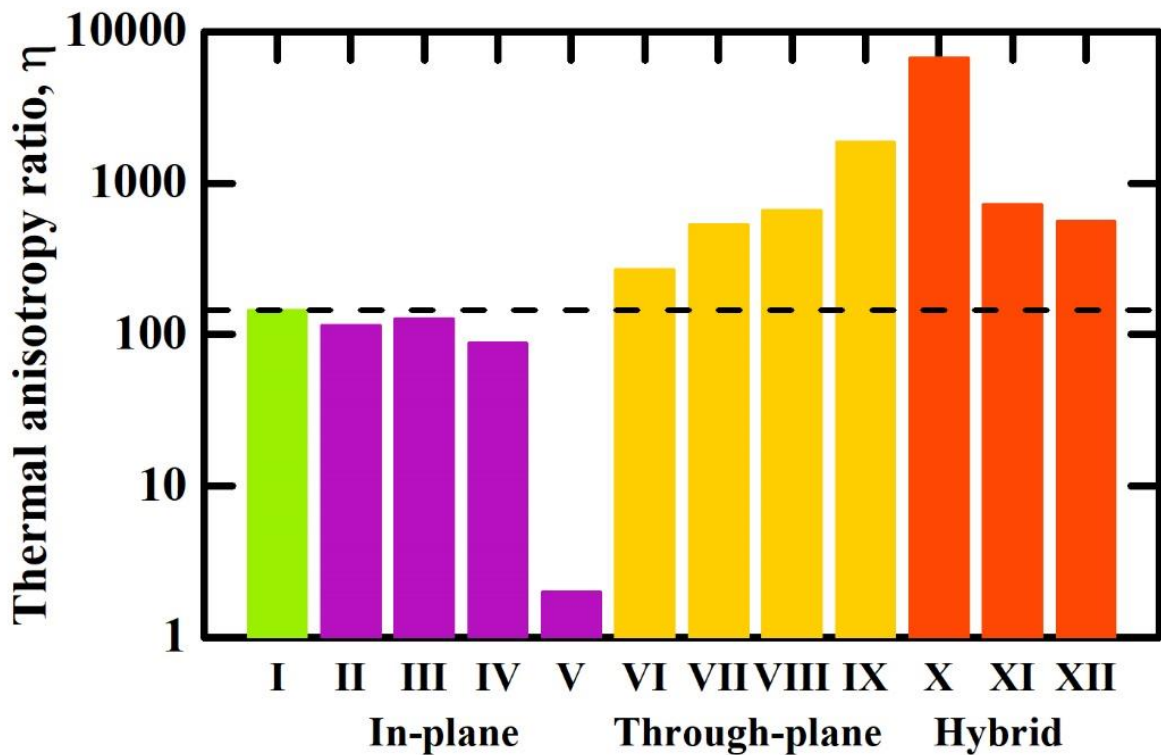


**Figure 3.4.** Thermal anisotropy ratio of graphite-like structures. The model ID is defined in Table 1. The in-plane disorders are II- V, the through-plane disorders are VI- IX, and the hybrid disorders are X - XII. To guide the eye, the dash line is the thermal anisotropy ratio for the pristine graphite.

## **B. Thermal anisotropy ratio**

Figure 3.4 summarizes the thermal anisotropy ratio  $\eta$  for all the model structures. The structures with in-plane mass disorders (II- IV) have the similar thermal anisotropy ratio compared with the pristine graphite because they have the reduced thermal conductivity both in the basal plane and along the c-axis. The structure with IPRD (V) has the lowest thermal anisotropy ratio and we can regard it as isotropic materials since the hetero-atoms in the alloy layered structure effectively scatter the phonons. The structures with through-plane disorders (VI- IX) have higher thermal anisotropy ratios compared with graphite since the through-plane mass disorders significantly reduce the through-plane thermal conductivity and preserve the in-plane thermal conductivity. The hybrid disorders (X- XII) have even higher thermal anisotropy ratio than that of through-plane disorders. The TPRMD is the best way to promote the thermal anisotropy ratio, which happens to be the most similar model to the real heterostructure materials. The van der Waals heterostructures applied in the real devices are made by mechanical assembly or direct epitaxial growth of layers with different types (they will have different masses).<sup>51,53</sup> If high thermal anisotropy ratio of the heterostructures is a desired property, our simulations provide a guideline for patterning; if the low through-plane thermal conductivity becomes a thermal management issue, our simulations also emphasize the importance of evaluating the thermal transport properties.

## **C. Phonon transport analysis**

To understand the anisotropic change of the thermal conductivity in structures with disorders, especially through-plane disorders, we investigate the dominant factors in the thermal conductivity of materials in the classical limit, which can be expressed by the Boltzmann transport equation with the relaxation time approximation,

$$\Lambda = \sum_k \sum_v c_{ph} v_g^2 \tau_{life} = \sum_k \sum_v \frac{k_B}{V} v_g^2 \tau_{life} \quad (3.4)$$

, where  $c_{ph}$  is the phonon specific heat,  $v_g$  is the group velocity, and  $\tau_{life}$  is the phonon lifetime. The specific heat is expressed as  $c_{ph} = k_B / V$  since the phonon Bose-Einstein distribution does not exist in the classic MD system, where  $k_B$  is the Boltzmann constant and  $V$  is the system volume. We calculated phonon dispersions of those graphite-like structures using the GULP package with the same interatomic potential as in MD.<sup>174</sup> Here, we compare the phonon dispersion of the pristine graphite to that of the graphite-like structures with the through-plane mass disorder ( $M_H=4m, 13m$ ) as an example to examine the effect of mass disorder. Figure 3.5 shows the change of the phonon dispersion due to the through-plane mass disorder by computing lattice dynamics on their unit cells. Figure 3.5a shows the phonon dispersions along the  $\Gamma$ -K direction (corresponds to the ab-plane in the real space) for the pristine graphite and through-plane mass disorders  $M_H=4m, 13m$ . Because the only difference between the layers is the mass, the dispersion curve of the TPMD structure is simply the combination of pristine graphite and ‘heavier’ graphite dispersions. The ‘heavier’ graphite has a dispersion with every branch shifted downward. Figure 3.5b shows the phonon dispersion along the  $\Gamma$ -A direction (corresponds to the c-axis in the real space). Comparing with the pristine graphite, the through-plane mass disorder opens the phononic bands, create band gaps between the transverse (longitudinal) optical branch and transverse (longitudinal) acoustic branch at the zone boundary, and shift the curves downwards (i.e., suppress the phonon group velocity).

We can compute the group velocity of all branches using the equation,  $v_g = \partial\omega / \partial k$ . Most of the high group velocity in the ab-plane branches remain the same as in pristine graphite, and the additional branches with lower group velocities originate from the layer with heavier mass. Figure 3.6a shows the group velocity for the four branches with the lowest frequencies, i.e.,

transverse acoustic (TA), transverse optical (TO), longitudinal acoustic (LA), and longitudinal optical (LO) branches. Longitudinal branches have higher group velocities in general. The group velocity of all branches along the  $c$ -axis is significantly suppressed with heavier mass, especially at the zone boundary. We also found that when the through-plane mass contrast increases, the group velocity reduction of acoustic branches is more considerably.

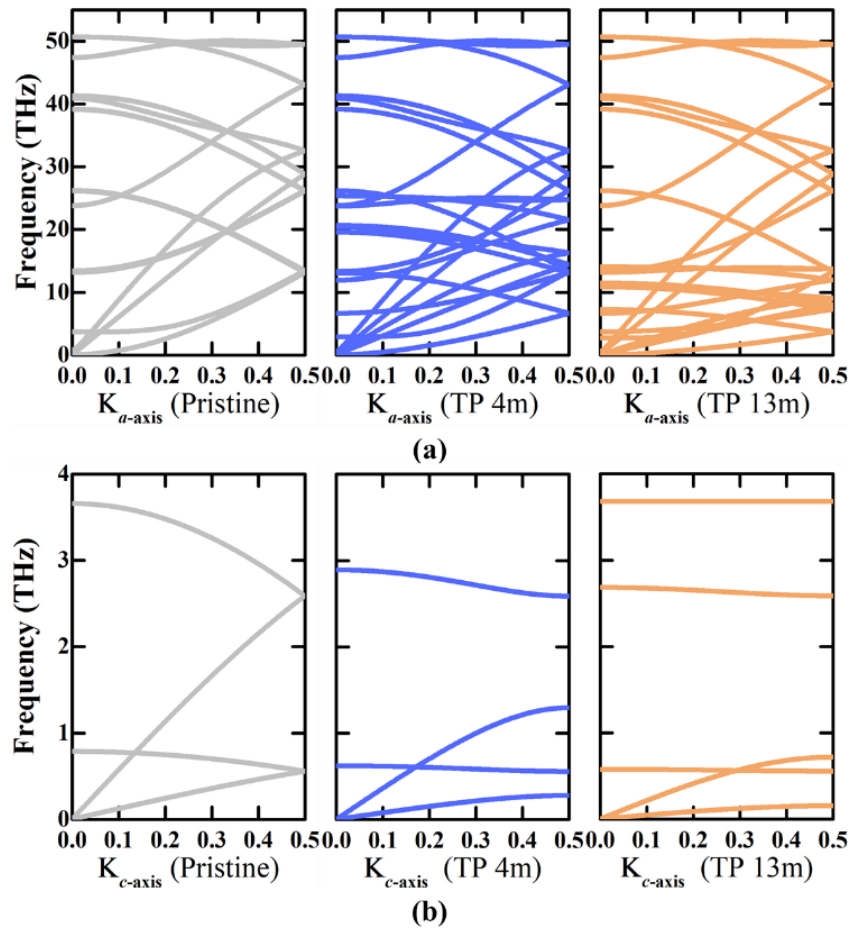


**Figure 3.5.** Phonon dispersion of (a) the pristine graphite and the through-plane mass disorder in the  $\Gamma$ -K direction (along the  $ab$ -plane) (b) in the  $\Gamma$ -A direction (along the  $c$ -axis). TP 4m and 13m are the through-plane mass disorder structure with hetero atom mass as 4m and 13m, respectively.

As a comparison, we also calculated the phonon dispersion of the structure with SD (the data is not shown). We found the acoustic branches in the  $\Gamma$ -K direction are almost similar with that of the pristine graphite, while only the TA and TO modes in the  $\Gamma$ -A direction (c-axis) slightly suppressed compared to the pristine graphite, which could explain why the reduction of through-plane thermal conductivity in SD is much smaller than the TPMD and TPRMD.

We calculated the phonon lifetime to further understand the reason for the thermal anisotropy ratio enhancement in graphite-like structures by the normal-mode analysis (NMA).<sup>175,176</sup> We project the trajectory of the atomic position and atomic velocity on the eigenvectors of normal mode coordinate. The vibrational position trajectory of mode  $(\kappa_v)$  under the normal mode coordinates,  $q(\kappa_v; t)$ , is<sup>176</sup>

$$q(\kappa_v; t) = \sum_{b,t} \left( \frac{m_b}{N} \right)^{1/2} \exp[i\kappa \cdot r_{(0)}^l] e_b^*(\kappa_v) \cdot u_b^l(t) \quad (3.5)$$

, where the superscript \* denotes complex conjugate operation,  $\kappa$  and  $v$  are the wavevector and polarization of the phonon mode (branch), respectively.  $u_b^l(t)$  is the real-space atomic displacement of the  $b$ -th atom in the  $l$ -th unit cell at time  $t$ ,  $r_{(0)}^l$  is the equilibrium position in the  $l$ -th unit cell,  $e_b$  is the eigenvector of the normal mode at atom  $b$  with mass  $m_b$ , and  $N$  is the total number of atoms in the simulation cell. Its time derivative,  $\dot{q}(\kappa_v; t)$  is the vibrational velocity trajectory. By using the velocity trajectory, we can obtain the kinetic energy of the normal modes  $(\kappa_v)$ .<sup>177</sup>

$$T(\kappa_v; t) = \frac{1}{2} \dot{q}^*(\kappa_v; t) \dot{q}(\kappa_v; t) \quad (3.6)$$

From the lattice dynamic theory, the phonon lifetime using the autocorrelation function of kinetic energy is<sup>177</sup>

$$\frac{\langle T(\kappa; t)T(\kappa; 0) \rangle}{\langle T(\kappa; 0)T(\kappa; 0) \rangle} = \cos^2 [\omega_\alpha(\kappa) t] \exp[-t / \tau(\kappa)] \quad (3.7)$$

, where  $\omega_\alpha(\kappa)$  is the anharmonic frequency and  $\tau(\kappa)$  is the phonon life time of normal modes.

Here, the anharmonic frequency can be replace with the harmonic frequency since we confirmed that the harmonic frequency is insignificantly different from the anharmonic frequency in our case,  $\omega_\alpha(\kappa) \cong \omega(\kappa)$ .<sup>63</sup>

The NMA for the pristine graphite and the TPMD in the ab-plane is conducted on a rectangular pristine graphite structure (3584 carbon atoms) with the conventional cell numbers  $N_x = 14$ ,  $N_y = 8$ ,  $N_z = 4$  in the  $x$ ,  $y$ ,  $z$  directions, respectively. Thus, four reduced wavevectors exist along the  $\Gamma$ -K direction, which is from 0.125 to 0.5. The NMA for those along the c-axis is conducted on a rectangular pristine graphite structure (7168 carbon atoms) with the conventional cell numbers  $N_x = 14$ ,  $N_y = 8$ ,  $N_z = 8$  in the  $x$ ,  $y$ ,  $z$  directions, respectively. We increased the cell number in the z-direction to ensure four reduced wavevectors exist along the  $\Gamma$ -A direction, which is from 0.125 to 0.5. We confirmed that the simulation domain with those unit cell numbers render the converged thermal conductivity values.

We found that phonon lifetimes of both the pristine graphite and the TPMD with  $M_H=13m$  in the ab plane decreases with the frequency and then reaches a plateau at optical frequencies. In addition, the TPMD with  $M_H=13m$  has larger phonon lifetime in the ab plane than that of the pristine graphite. Similar trends of phonon lifetime are observed along the c-axis. Figure 3.6b shows the phonon lifetime comparison between the pristine graphite and the TPMD with  $M_H=13m$  along the c-axis for the TA, TO, LA, LO modes at these four wavevectors. The transverse branches have higher phonon lifetime than the longitudinal branches. Even though the group velocity of the pristine graphite is much larger than that of the TPMD at all K points, the

phonon lifetime of the TPMD with  $M_H=13$ , however, is larger than that of the pristine graphite in all the modes. Two possible reasons contribute to this increase of phonon lifetime: (1) the phonon scattering rate is proportional to the scattering matrix component, which scales inversely with the atomic mass. Therefore, the phonon lifetime is higher because of the reduction of phonon scattering rate due to the increased atomic mass in the unit cell;<sup>178</sup> (2) the increase in lifetimes could be due to the acoustic (a) - optical (o) scattering selection rules. As shown in the dispersion curves in Figure 3.5, the gap between acoustic branches and optical branches increases with increasing mass of the hetero atoms. Since the higher frequency optical phonons provide possible scattering channels for the acoustic modes through aao scattering, the reduced possibility or absence of aao scattering due to the increases gap increases the lifetime of acoustic phonons.<sup>170,171</sup>

Thus, because of the opposite trend of phonon group velocity and phonon lifetime change with the through-plane mass disorder, the calculated thermal conductivity result indicates that the group velocity plays a more important role in determining the thermal conductivity of through-plane disorders than the phonon lifetime. In order to validate this, Figure 3.6c shows the selected mode-wise data of phonon lifetime multiplied by the squared group velocity  $v_g^2 \tau$  life along the c-axis in the pristine graphite and the TPMD from the equation (4) with the relaxation time approximation. Apparently for  $\sum \sum v_g^2 \tau$  life of those modes, the pristine graphite is much larger than that of the TPMD and the dominant reason for the difference is the suppression of phonon group velocity, not the phonon lifetime.

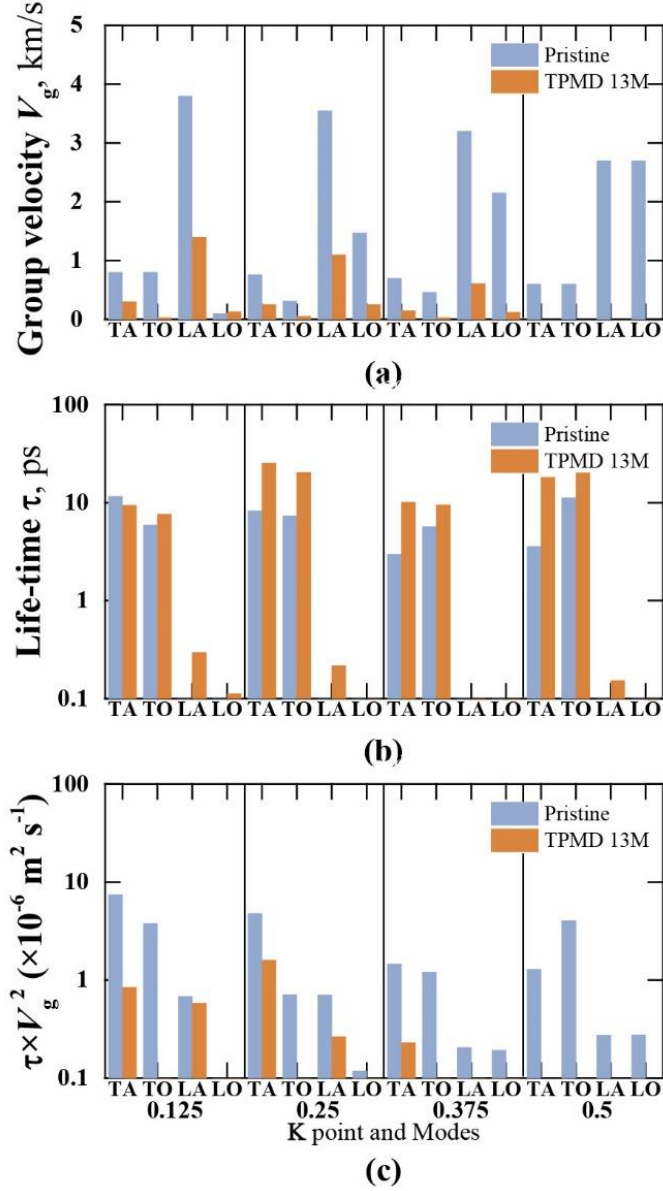


**Figure 3.6.** Phonon transport analysis for the comparison between pristine graphite and the TPMD graphite with  $M_H=13\text{m}$  along the  $c$ -axis. (a) Phonon group velocity  $v_g$ , (b) phonon lifetime  $\tau_{life}$ , and (c)  $v_g^2 \tau_{life}$ . The reduced wavevector  $K$  point is from 0.125 to 0.5. Four phonon modes are shown here: transverse acoustic (TA), transverse optical (TO), longitudinal acoustic (LA), and longitudinal optical (LO) modes that are significantly contributed to the thermal conductivity along the  $c$ -axis. The pristine graphite is colored by light blue, and the TPMD 13M is light orange. Certain values are too small to show in the plots.

Therefore, for the structures with through-plane mass disorders and hybrid random mass disorder, the thermal conductivity in the basal plane slightly decreases due to the moderate decrease of averaged phonon group velocity (the combination of different phonon group velocities due to the different atomic mass); the thermal conductivity in the c-axis reduces dramatically because of the remarkable change of phonon dispersion relations due to the mass contrast.

We note here that our simulations do not change the interactions among the atoms when some of the carbon atoms are replaced with hetero atoms with heavier mass. This approach is similar with the studies on thermal transport across superlattice structure<sup>179</sup> and interfacial thermal conductance across bridge layer to isolate the effect of mass difference.<sup>180</sup> In fact, we are aware that incorporating hetero-atoms into a structure will definitely change such interactions, which will in turn change both the phonon group velocity and phonon lifetime. It could be an interesting future work to accurately describe the interatomic interactions in those structures with high thermal anisotropy ratio so that the complicated effect of disorder on anisotropy thermal conductivity can be thoroughly understood.

#### **4. Summary**

In summary, we used equilibrium molecular dynamics simulations to study how disorders affect the anisotropy thermal conductivity and thermal anisotropy ratio of 2D materials and van der Waals heterostructures. Among the three categories of disorder, i.e., in-plane disorder, through-plane disorder, and hybrid disorder, the latter two categories could provide an enhanced thermal anisotropy ratio. The structures with through-plane mass disorders and hybrid random mass disorder naturally appear as van der Waals heterostructures, which could function

as a directional heat spreader in the device. Our analysis would provide a new insight into the thermal management of the nanoelectronics incorporating 2D materials and van der Waals heterostructures.

## CHAPTER 4

In the previous chapter, I found that the most effective mass disorder is the through-plane random mass disorder (TPRMD), which has a different mass each layer. However, a comprehensive understanding requires more systemic studies on the effect of the magnitude of mass, the influence of the mass pattern each layer, and the relationship between mass pattern and thermal transport in each layer. In this chapter, I investigated the effects of various mass disorder pattern on thermal transport in van der Waals heterostructures using MD simulations.

### 1. Introductions

Recently, electronic devices have developed drastically, but they generate a tremendous amount of heat. The thermal management of nano-electronic devices is problematic. 2D materials are crystalline materials consisting of a single layer of atoms, and heterostructure is the multi-layers stacked with various 2D materials. They are highly anisotropic because they have strong bonds in the basal plane and are stacked each by weak van der interaction. Therefore, it can function as a directional heat spreader due to their structures with their high thermal anisotropy ratio.

The disorder generally decreases thermal properties. However, researchers found that the disorder can increase the thermal anisotropy ratio. One of excellent examples is the lithiated graphite and molybdenum disulfide. Thermal conductivity of lithium graphite intercalation compounds ( $\text{Li}_x\text{C}_6$ ) is calculated by using molecular dynamics simulations.<sup>63</sup> Here, the thermal anisotropy ratio of the lithiated graphite compound successfully increases. This clearly shows that it is necessary to change the thermal conductivity along the z-direction but to conserve the thermal capability on the XY plane. Several examples reported the thermal conductivity of the heterostructures along the z-direction decreases.  $\text{MoS}_2 / \text{MoSe}_2$  heterostructures can decrease the

thermal conductivity along the  $z$ -direction.<sup>100</sup> Ding *et al.*<sup>153</sup> also reported the Graphite / MoS<sub>2</sub> heterostructures also have a similar trend.

The mass disorders or mismatch is usually an effective way to change the thermal anisotropy ratio. By using this idea, we made and categorized several structures with disorders. My previous work showed which kinds of disorders effectively increase the thermal anisotropy ratio. Then we discuss how these disorders change the thermal anisotropy ratio. Among the three categories of disorder (in-plane disorder, through-plane disorder, and hybrid disorder), the latter two categories could provide an enhanced thermal anisotropy ratio. According to Allen and Feldman (A-F),<sup>181</sup> thermal vibrational modes in the disordered materials consist of three parts: propagon, diffuson, and locon. (1) Propagon, which is the propagating vibrational modes, is similar to a crystalline solid and transports heat efficiently. (2) Diffuson, similarly amorphous, is random energy transportation. It is less efficient than propagon. (3) Locon is a true insulating state. The energy in locon mode remains localized unless scattered. The thermal conductivity of through-plane disorder along the  $z$ -direction decreases because propagon modes decrease, and there is thermal localization along the  $z$ -direction.

The most effective mass disorder is the through-plane random mass disorder (TPRMD), which has a different mass each layer. However, it requires more systemic studies on the effect of the magnitude of mass, the influence of the mass pattern each layer, and the relationship between mass pattern and thermal transport in each layer. In this chapter, we theoretically investigated multilayer van der Waals heterostructures with different mass patterns using molecular dynamics (MD) simulations. We systematically built the graphite-like TPRMD structures both in the in-plane and through-plane directions with the mass pattern to study thermal transport in the patterned layers.

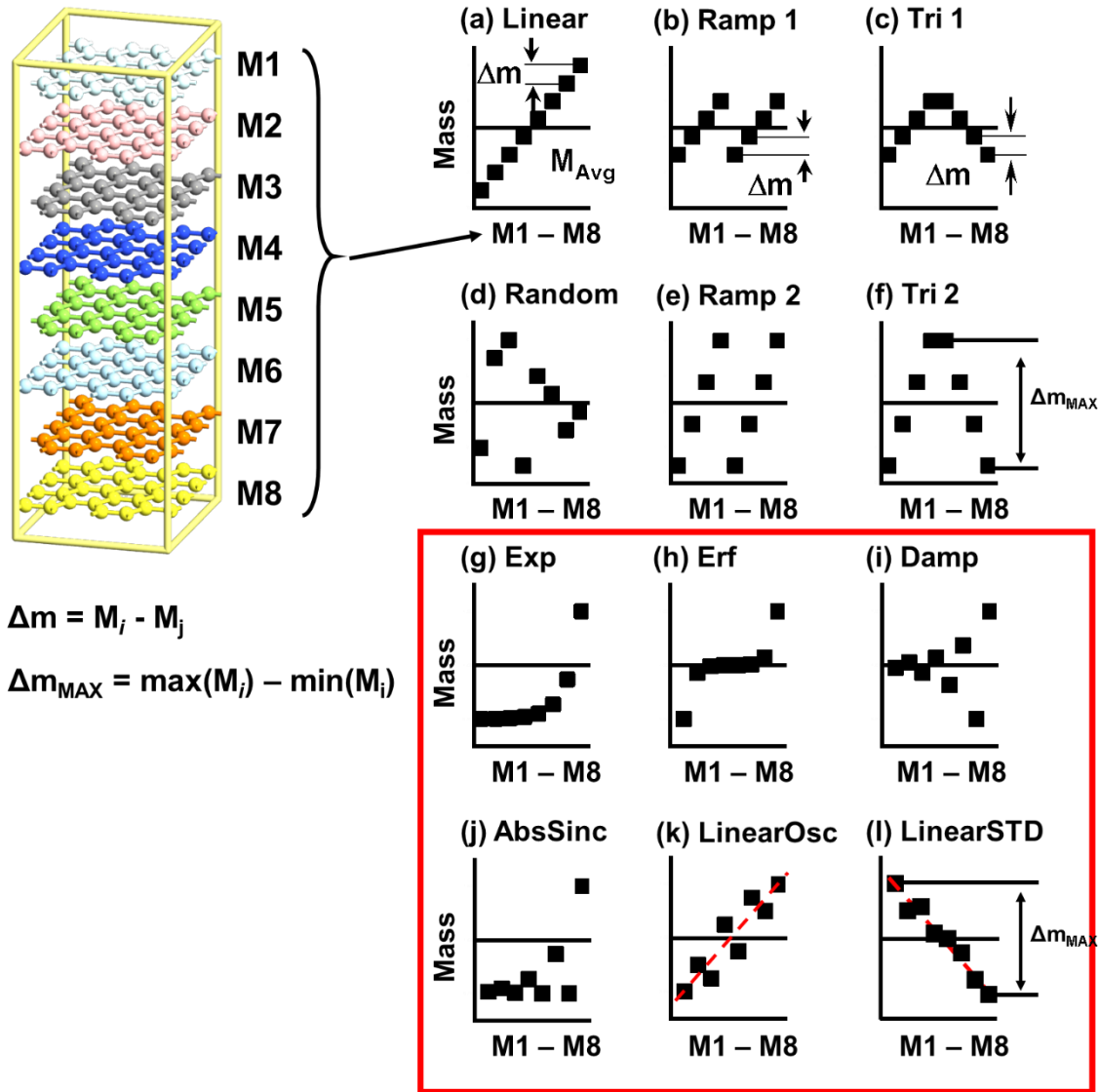


**Figure 4.1.** Various mass disorder patterns in the through-plane mass disorder of graphite-like structures. The different mass distribution is following as (a) linear pattern, (b) ramp pattern with the same mass gap each layer, (c) triangle pattern with the same mass gap, (d) random pattern, (e) ramp pattern with the same maximum mass difference, (f) triangle pattern with the same maximum mass difference, (g) exponential difference pattern, (h) error function pattern, (i) damping function pattern, (j) absolute sinc function pattern, (k) linear oscillation pattern, and (l) linear trend function, respectively. The mass gap each layer is 1% difference but 0.5% in a red box except for (e) and (f).

This simple model with well-defined atomic structures and interatomic interactions can capture the features of the mass pattern effect. It provides insights on the design of anisotropic materials, especially for small mass disorders.

## 2. Materials models and computational details

We systemically built mass patterns in the TPRMD using VNL software in figure 4.1. Figure 4.1 shows various mass disorder patterns in the through-plane mass disorder of graphite-like structures. The different mass distribution is as following (a) linear pattern, (b) ramp pattern with the same mass gap each layer, (c) triangle pattern with the same mass gap, (d) random pattern, (e) ramp pattern with the same maximum mass difference (twice mass gap), (f) triangle pattern with the same maximum mass difference (twice mass gap), (g) exponential difference pattern, (h) error function pattern, (i) damping function pattern, (j) absolute Sinc function pattern, (k) linear oscillation pattern, and (l) linear trend function, respectively. The mass gap each layer is 1% difference but 0.5% in a red box except for (e) and (f). We computed the thermal conductivity of the graphite-like structures with various mass distributions by using the EMD simulations. The EMD simulations offer thermal conductivities along with three directions and do not apply the external turbulent. We conduct all MD simulations using LAMMPS programs and calculate the thermal conductivities by Green-Kubo (G-K) equation. In the previous work, we only changed the mass each layer. This treatment ensures the isolation of effects due to mass disorder only. We used 'm' to represent the mass of the carbon atom C, and the difference of the mass is the certain percentage of carbon atom's mass. We set the time step as 1 fs and used a hybrid Tersoff and Lennard-Jones (LJ) potential<sup>125,162</sup> to describe the interactions between atoms. Tersoff potential was used to model the C-C bond for the in-plane atomic interaction, and the

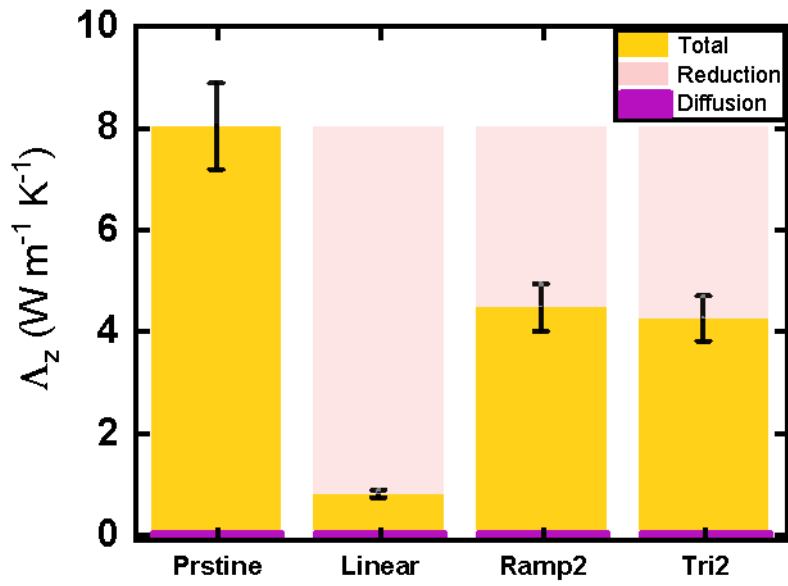
standard Lennard-Jones (L-J) 6-12 potential was used to model the through-plane atomic interactions between each layer. In L-J potential, the value of  $\sigma$  and  $\varepsilon$  is  $\sigma = 0.335$  nm and  $\varepsilon = 4.6616$  m eV, respectively. All structure is the  $14 \times 8 \times 8$  cell compared to the pristine graphite. The NPT, NVT, and NVE ensemble at 300 K had been applied for relaxation. More detailed information can be found from chapter 3. We also calculate the non-propagation thermal conductivity using the GULP software using the Allen and Feldman thermal conductivity.<sup>182</sup> Thermal conductivity in the disordered materials can be described as:

$$\Lambda_{\text{Total}} = \Lambda_{\text{Propagon}} + \Lambda_{\text{A-F}} \quad (4.1)$$

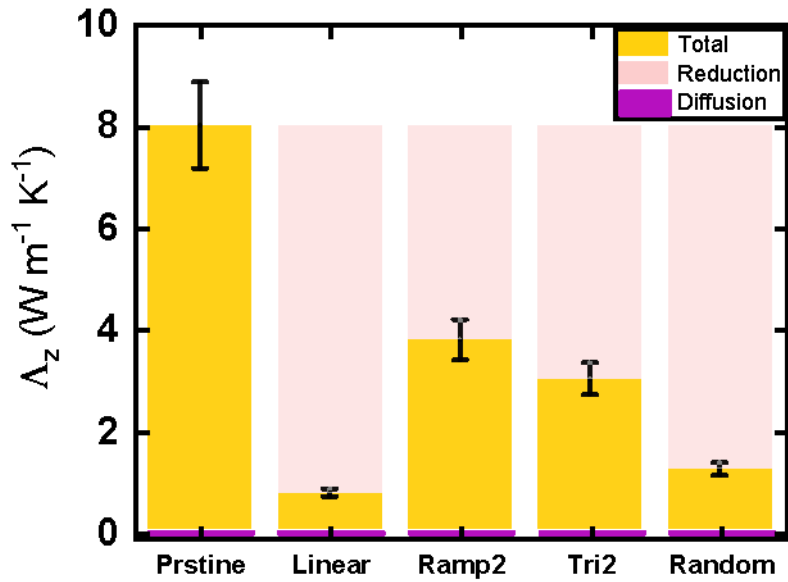
,where the  $\Lambda_{\text{Total}}$  is the total thermal conductivity, which can be achieved by the G-K calculation,  $\Lambda_{\text{Propagon}}$  is the thermal conductivity contributed by propagating vibrational mode, and  $\Lambda_{\text{A-F}}$  is the Allen and Feldman thermal conductivity, which demonstrates that the thermal conductivity without the propagon. We can judge the thermal conductivity of the propagon by using two thermal conductivity because thermal vibrational modes consist of propagon, diffuson, and locon.

### 3. Results and discussion

Figure 4.2 shows the calculated thermal conductivity along the z-direction of various mass distribution in TPMD structures. A light orange bar is total thermal conductivity calculated by the EMD simulations with G-K function, and a violet bar is the A-F thermal conductivity (Diffuson) using GULP.<sup>182</sup> A transparent pink bar is the reduction of thermal conductivity due to thermal localization caused by the mass disorder, which can be achieved by subtraction of the total thermal conductivity to the A-F thermal conductivity by the following equation (1).



(a)



(b)

**Figure 4.2.** Thermal conductivity along the  $z$  directions of various mass pattern from (a) to (f). (a) the same mass difference each layer (b) the same maximum mass difference. Light orange, transparent pink, violet is total thermal conductivity, reduction of thermal conductivity, diffusion-related thermal conductivity, respectively.

Figure 4.2a demonstrates the computed thermal conductivity along the z-direction of various mass patterns with the same mass difference each layer, which is a 1% difference compared to the carbon mass. The in-plane thermal conductivity of the through-plane mass disorder is conserved ( $\sim 1600 \text{ W m}^{-1} \text{ K}^{-1}$ ), which we did not show because it is already reported in the previous study.<sup>183</sup> The thermal conductivities along the z-direction of whole mass patterns decrease, and the ramp pattern and triangle pattern decrease roughly 50%. The linear mass pattern shows a decrease to  $0.7 \text{ W m}^{-1} \text{ K}^{-1}$ , which is roughly one eleventh.

Figure 4.2b demonstrates the computed thermal conductivity along the z-direction of various mass patterns with the same maximum mass difference, which is the subtraction of the minimum mass from the maximum mass among the structure. Light orange, transparent pink, violet is total thermal conductivity, reduction of thermal conductivity, the diffusion related thermal conductivity, respectively. The conductivities along the z-direction of whole mass patterns with the same maximum mass difference decrease a lot. The ramp 2 and the triangle 2 patterns show more decrease of thermal conductivity than the ramp 1 and triangle 1 patterns. It clearly shows that the maximum mass difference is proportional to the reduction of thermal conductivity. The most effective mass disorder patterns are the linear pattern and the random pattern. Interestingly, the linear pattern has a more reduction effect than the random pattern. We also show the A-F thermal conductivities (violet bar) of whole patterns along the z-direction, which is contributed by diffusion and locon, are extreme minor values. Therefore, we can assume that the propagon (the propagating vibrational modes) decrease due to the mass disorder.

We calculated phonon dispersions of those graphite-like structures using the GULP package with the same interatomic potential as in MD. Figure 4.3 show dispersion curves along the z-direction of the linear mass pattern with the different mass gap between each layer.

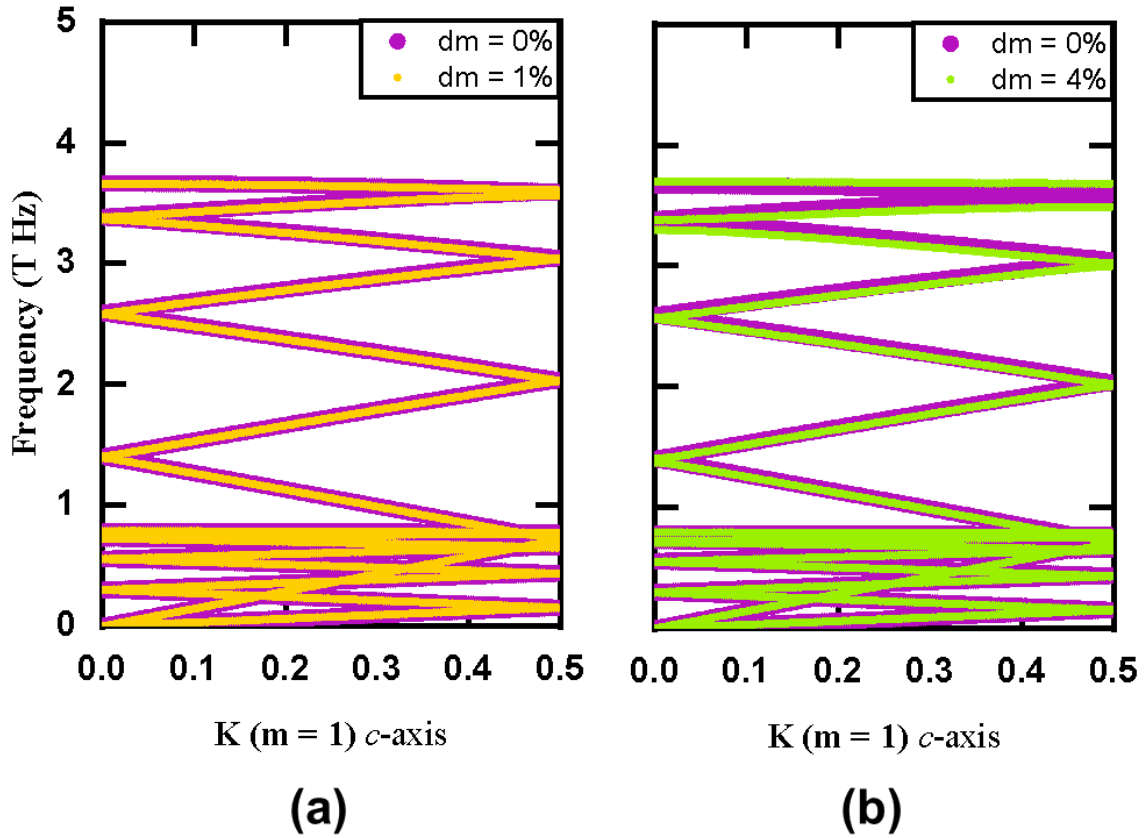


**Figure 4.3.** Dispersion curves along the  $z$  directions of linear mass pattern depending on the  $K$  points: (a) pristine and linear pattern with 1% mass gap, (b) pristine and linear pattern with 4% mass gap. The violet line is the dispersion curve of the pristine graphite with eight layers, orange is that of the linear pattern with 1% mass gap, and the light green is that of the linear pattern with 4% mass gap.

Figure 4.3a shows the dispersion curves of pristine graphite and the through-plane mass disorder with the linear pattern with a 1% mass gap, and figure 4.3b shows the dispersion curves of the pristine and the linear pattern with a 4% mass gap. We focused on the acoustic branches, and the  $x$ -axis is the  $K$  points along the  $c$ -axis. The violet line is the dispersion curve of the pristine graphite (0% mass gap) with eight layers, orange is that of the linear pattern with 1%

mass gap, and the light green is that of the linear pattern with 4% mass gap. There is no difference between the pristine and 1% TPMD with the linear pattern, but the thermal conductivity decreases one eleventh. It means that the thermal conductivity reduction with the small mass disorder is not dominantly contributed by the group velocity. The dispersion curve with the linear pattern 4% shows a small change of the dispersion curve between 3 and 4 T Hz. There is a disconnection of the 4% ‘linear’ dispersion curves between two upper branches. This disconnection clearly shows that the group velocities can be suppressed by this effect, so we would like to check the group velocity. Lower group velocities can suppress the thermal conductivity by reducing the energy transfer rate of acoustic phonon. Figure 4.2 supports figure 4.3: The softening of the atomic vibrations could result in a lower frequency of the Ioffe–Regel transition, so more vibration modes become diffuson.

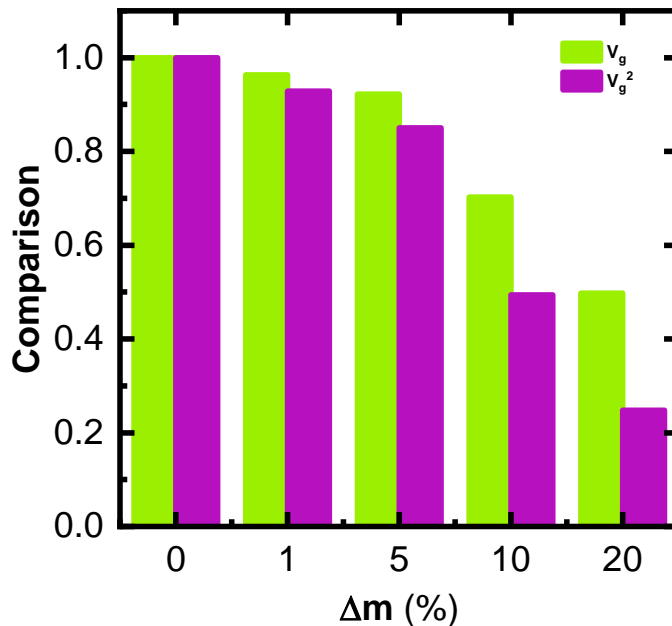


**Figure 4.4.** Normalized group velocity along the  $z$ -direction of linear graded mass pattern model depending on the mass difference ( $\Delta m$ ). The light green and the violet bar is the group velocity and the group velocity squared, respectively.

The propagon can be suppressed, not communicate with the surrounding, and finally isolated from others. Therefore, the thermal conductivity of a small mass disorder decreases a lot even compared with the regular through-plane large mass disorder.

Figure 4.4 shows the normalized average group velocity and the squared velocity along the z directions of linear graded mass pattern model depending on the mass difference ( $\Delta m$ ). A light green and violet colored bar are the group velocity and the group velocity squared, respectively. Although the group velocity decreases exponentially depending on the mass difference with the linear patterns, the reduction of the group velocity and the squared value with the 1% mass difference is less than 5% and 10 % compared to the group velocity of the pristine graphite, respectively. It means that the most contribution to the thermal conductivity reduction is not from the group velocity but the other factors. We assumed that the unbalanced mass distribution has the effect to prevent atomic motions from propagation movement and make them isolated from the surroundings. To understand the mass disorder effects, we would like to introduce the asymmetric value using the mass distribution and the locations because our mass disorder patterns consist of the locations and mass. The asymmetry  $C_z$  is defined as:

$$C_z = \frac{\sum_i m_i r(z)_i}{\sum_i m_i} \quad (4.2)$$

, where  $m_i$  is the mass of the  $i^{\text{th}}$  layer and  $r(z)_i$  is the location of the  $i^{\text{th}}$  layer based on the central position. Moreover, we computed the additional mass pattern within red box in figure 4.1. We have already observed the linear and random pattern effect, so we set the mass difference is 0.5% to see the additional mass pattern (g - l) effects depending on the asymmetry. We also made more random patterns and the linear trend pattern to compare those fairly.

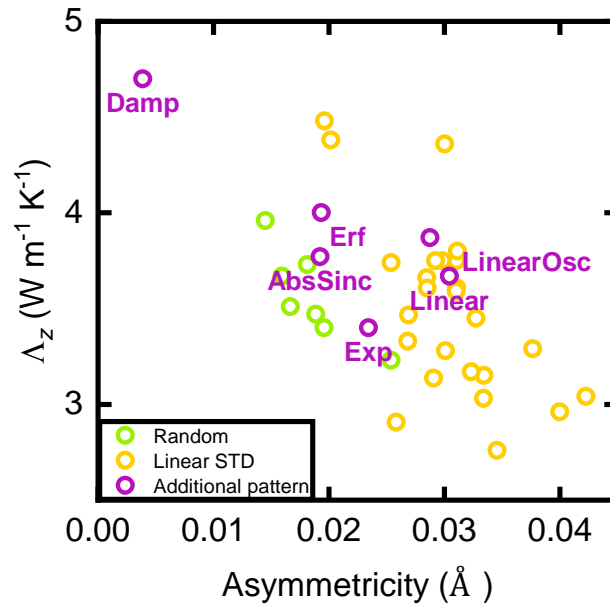


**Figure 4.5.** Various statistical parameters of mass distribution ( $g - l$ ) depending on the thermal conductivity along the z-directions. The light green, light orange, violet line is the various random mass patterns, the linear trend patterns, and additional mass patterns, respectively.

Figure 4.5 shows various statistical parameters of mass distribution ( $g - l$ ) depending on the thermal conductivity along the z-directions. The light green, light orange, violet line are the various random mass patterns, the linear trend patterns, and additional mass patterns, respectively. Exp is an exponential difference pattern, Erf is an error function pattern, Damp is a damping function pattern, AbsDamp is an absolute damping function pattern, and Linear Osc is a linear oscillation pattern in the violet-colored circles. We can see a clear trend that the thermal conductivity decreases depending on the asymmetry with the same maximum mass difference. It clearly shows that the small mass disorder with a strong asymmetry breaks propagon. This contribution to the thermal conductivity reduction is much more dominant than the group velocity. The asymmetry, which is the mass centroid, can affect the thermal

transport because in asymmetric materials all the phonons are converted to short mean free path and diffusons. The vibration modes cannot participate in their motions together but separately contribute to each carrier.

We note that our simulations use the same potential among the atoms and only change the mass distribution with the small differences depending on each layer. This approach is similar to our previous study<sup>183</sup> and the studies on the thermal transport of isotope materials.<sup>184</sup> Here, we assume that a change of such interactions in the small mass pattern structures can be neglected due to a very small difference. We found that the asymmetry can affect thermal transport in the structures with the small mass disorder. It would be an interesting future work to study how the asymmetry can change thermal transport so that the complicated effect of disorder on anisotropy thermal conductivity can be thoroughly understood.

#### **4. Summary**

In summary, we used equilibrium molecular dynamics simulations to study the effect of the magnitude of mass, the influence of the mass pattern each layer, and the relationship between mass pattern and thermal transport in each layer. Among various mass patterns, the random mass pattern and linear mass pattern show a strong reduction to thermal transport in the through-plane mass pattern structures. We found that the asymmetry can disturb thermal transport in the structures with a small mass disorder. Our analysis would provide a new insight into the thermal management of the nanoelectronics incorporating 2D materials and van der Waals heterostructures.

## CHAPTER 5

In the previous chapter, I studied the theoretical thermal transport in the anisotropic materials, but we did not demonstrate the experimental study on any real materials. In this chapter, I studied the anisotropic thermal conductivity of the high-density polyethylene fibers using time-domain thermo-reflectance (TDTR) method and discuss how the distribution of defects affect the measured results.

### 1. Introductions

Due to the low thermal conductivity of polymer, it has been commonly used for an insulator, but the micro-sized polymer can have potentially high thermal conductivity than its bulk. When each polymer chain aligns perfectly with each other along with the chain backbone structures, the thermal conductivity can be high.<sup>166</sup> For instance, He's simulation work<sup>82</sup> shows the thermal conductivity of the semi-crystalline polyethylene increasing when we stretch it. The reason is that the alignment becomes more organized, and the backbone contributes to more thermal transport due to the focusing effect.<sup>81</sup> Experimental measurement also supports that the thermal conductivity of polymers can be high. For example, Choy *et al.*<sup>65</sup> reported the thermal conductivity of low-density polyethylene fiber-reinforced plastic (FRP) is  $30 \text{ W m}^{-1} \text{ K}^{-1}$ . Recently, Shen *et al.*<sup>79</sup> reported that polyethylene (PE) nanofibers are  $100 \text{ W m}^{-1} \text{ K}^{-1}$  by using a biomaterials microcantilever. However, the measured thermal conductivity may be overestimated or underestimated due to experimental limitations of measurement techniques.

The thermal conductivity of polymer fibers in the axial and radial directions has been studied for recent years. Wang *et al.*<sup>80</sup> reported that the axial thermal conductivity of commercial high-density polyethylene (HDPE) fibers are  $10 - 25 \text{ W m}^{-1} \text{ K}^{-1}$ . Lu and Liu *et al.*<sup>81</sup> have

measured thermal conductivity in the radial direction of deformed polymer fibers. They found that the thermal conductivity of the fibers decreases when stretching, but the thermal conductivity of the polymer fiber without any deformation is still unknown. In this work, we are interested in measuring the thermal conductivity of polymer fibers in radial directions without any deformation. We also wanted to study the influence of the thermal conductivity with defects and alignment in microfibers by using the TDTR method. The penetration depth changes depending on the modulation frequency of the pulsed laser. Thus, we will measure the thermal conductivity along both the radial and axial direction depending on the modulation frequency. Both the axial and radial thermal conductivities of the polymer fiber have some fitting issues, so we discuss the thermal conductivity models and the possible fitting methods.

## **2. Materials and methods**

### **A. Sample preparation**

Our sample is the commercial high-density polyethylene (HDPE) fiber, spectra 900. To measure this flexible, tiny surface (with micro size diameter) sample, we should pre-process the sample for the TDTR. The TDTR technique is an optical method, so we need to get a very smooth surface to reflect the beam perfectly. There are four steps for sample preparation in figure 5.1: First, we embed the polymer fibers in a super glue. Secondly, we cut the sample surface by using microtomy with a diamond blade.

Next, we measure the surface roughness of the samples, confirming the surface quality (Figure 5.1c). If not, we go back to the second step. Finally, we deposit the aluminum metal film transducer on the sample (Figure 5.1d) using the sputtering method in the vacuum chamber ( $10^{-7}$  Torr). We used the aluminum film as the transducer layer for our TDTR because our laser wavelength ( $\sim 780$  nm) matches to the aluminum layer for the strong thermoreflectance.

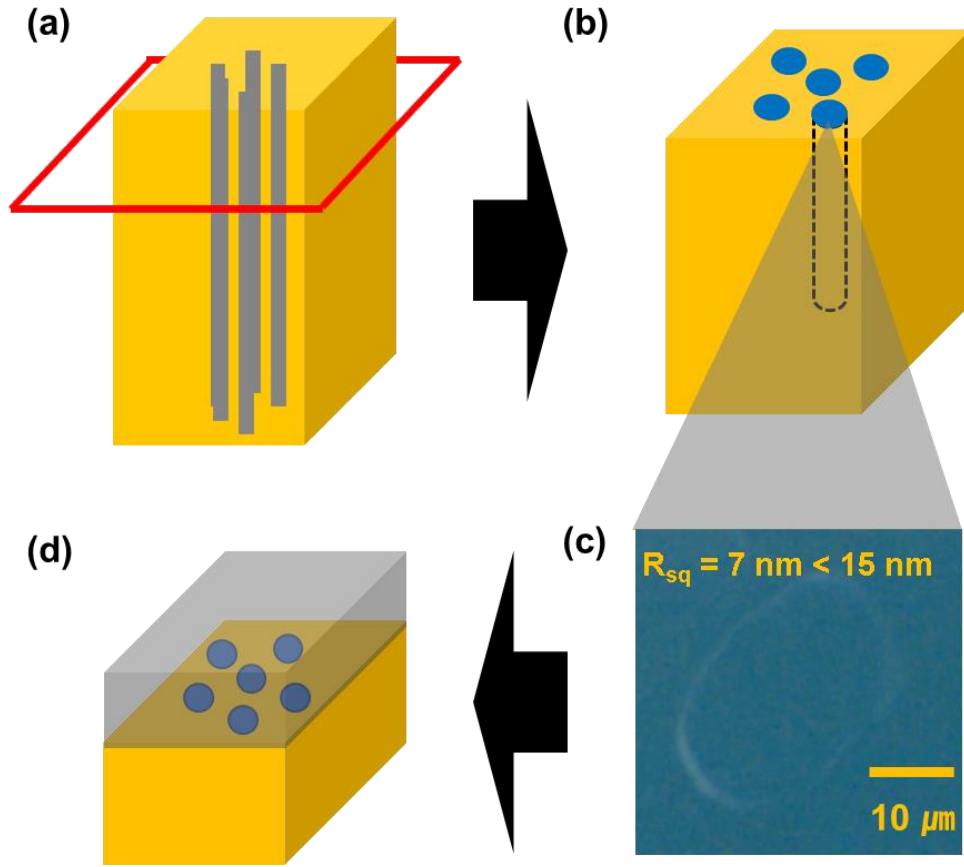


**Figure 5.1.** The schematics for the sampler preparation of the polymer fibers. (a) the embedded sample in the epoxy or super-glue, (b) the microtomed surface of the sample embedded in the super-glue (c) the optical image of the sample surface on the CCD camera in TDTR, (d) the aluminum thin film deposited on the sample surface.

The embedding material is the commercial super glue with low thermal conductivity (Permatex<sup>®</sup> Super Glue, Permatex, Inc.). We characterized the roughness of the surface by using a commercial confocal laser scanning microscopy (VKx 1100, Keyence, Osaka, Japan). The roughness  $R_q$  represents the standard deviation of heights. The roughness  $R_q$ , is defined as:

$$R_q = \sqrt{\frac{1}{l} \int_0^l h^2(x) dx} \quad (5.1)$$

, where  $l$  is the sampling length,  $h(x)$  is the measured height versus on the line. We can see relatively smooth fiber cross-sections with only some tiny stripes perpendicular to the direction of the cut caused by a moving motion of the diamond knife in the microtomy in figure 5.1c. When the roughness of the polymer fiber is less than 10 nm, we confirm that the microtomed fibers have enough smooth surface for TDTR measurement.

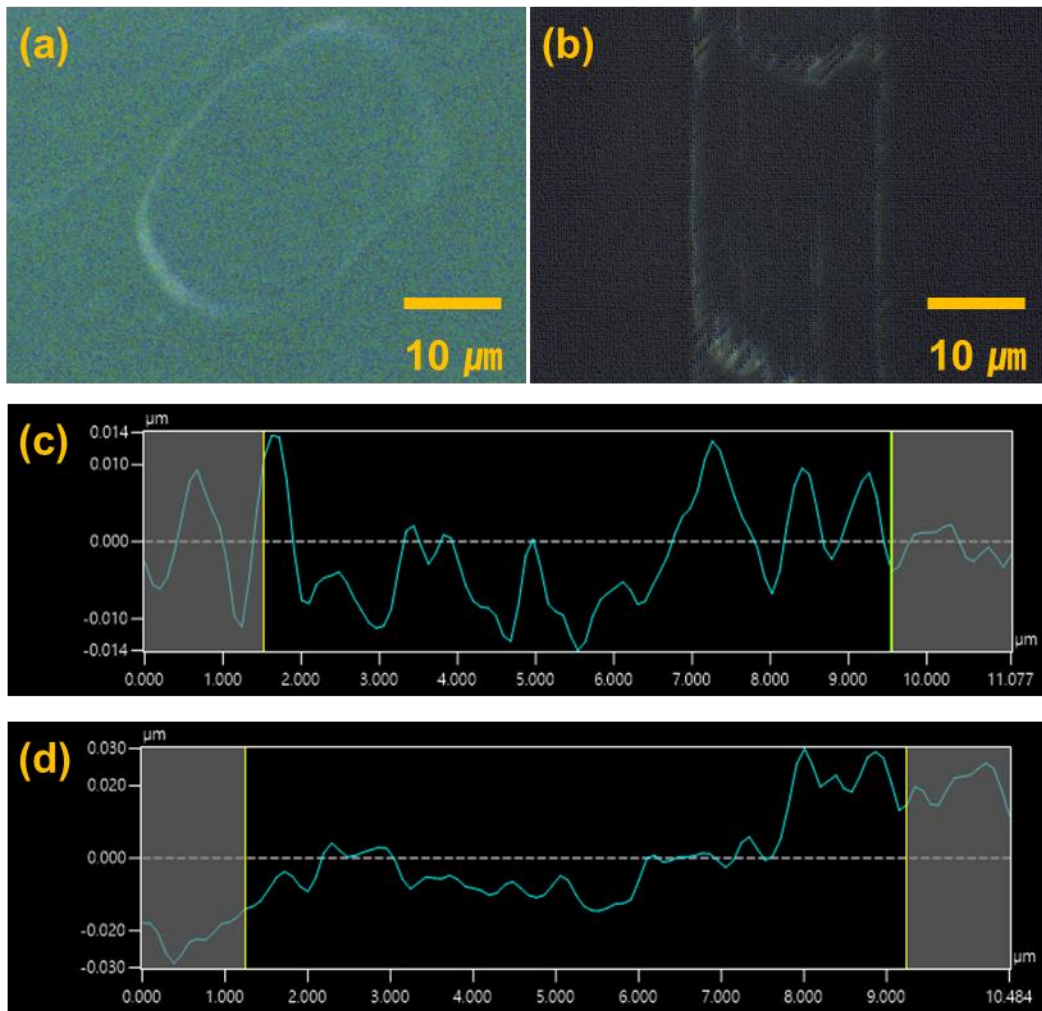


**Figure 5.2.** The optical image about the microtomed Spectra 900 surface along (a) the axial and (b) the radial on the CCD camera in TDTR. The surface profile of (c) the axial and (d) the radial surface of the sample measured by the confocal laser scanning microscopy.

Figure 5.2 shows the optical image of the microtomed Spectra 900 surface and the surface profile for the roughness characterization. Figure 5.2a and b show the sample surface along the axial and the radial directions on the CCD camera, respectively. Figure 5.2c and d show the surface profile of the axial and the radial surface of the sample measured by the confocal microscope.

### **B. Time-domain thermorefectance (TDTR) method**

We measured the thermal conductivity and the interfacial thermal conductance between aluminum and high-density polymer fiber at 300 K using the TDTR method with various modulation frequencies. The TDTR is two laser beam (the pump and probe) measurement techniques. A Ti: Sapphire Mode-Locked Lasers emit the pulsed laser at a repetition rate of the frequency with 80 M Hz. We modulated the pulsed pump beam using an electrical optical modulator (EOM) with the modulated frequency, whose controlling signals come from the function generator. The laser beam is the Gaussian beam, so it diverges depending on the distance. We should set a certain divergence to make the shape constant and the size of the pump and probe beam nearby the samples, by using two both vertical and horizontal rectangular lenses before the polarized beam splitter and one single circular lens after the polarized beam splitter. We found the proper locations of two rectangular lenses and a single lens.

The probe beam after the polarized beam splitter passes through the mechanical chopper to eliminate the  $1/f$  noise dominant until 100 Hz. The mechanical optical chopper rotates with constant speed and the plate containing several uniform holes, where the frequency of the chopper is 200 Hz. We aligned two split beams after the second polarized beam splitter before beams reach the objective lens. In free space, two beams are reflected by the sample surface, which should be sufficiently smooth to reflect perfectly. We install the objective lens to focus the

pump and probe beams with the radius of several microns. The beam spot sizes with the objective lens with the magnification of 10x and 20 are 6.0 and 3.0  $\mu\text{m}$ , respectively.

A pump beam heats up the metallic layer up, which can generate the heat and change its thermo-reflectance property depending on the temperature rise, and the other beam, a probe, monitors the metallic surface. The reflected probe beam can be captured by the detector, and we can achieve the voltage signals, which are proportional to the temperature due to thermo-reflectance. We used the aluminum metallic layer because the thermo-reflectance of the aluminum is a peak value at the wavelength of nearby 800 nm, which is roughly matched to our laser wavelength ( $\sim 785$  nm). The time among the pulsed pump laser with 80 MHz is 12.5 ns, so we can monitor the time-domain thermo-reflectance signals by changing the distance of the pump path through the mechanical delay stages. The propagating acoustic strain waves in the materials are shifted a  $\pi$ -phase depending on the acoustic impedance of the first and second layers. When the impedance of the first layer is lower than that of the second layer, the waves are  $\pi$ -shifted and show the downward signals in the time-domain. When there is the opposite configuration, the wave shows no phase shift of the strain wave.

### **3. Data analysis and thermal transport modeling**

We enlarged the received signals through several processes. First, the signals go through the electrical inductor to remove the higher harmonic. We amplified the filtered signals using the pre-amplifier (5x) and an RF-lock in the amplifier because the signals without the amplifier are very weak ( $\sim 10^{-4}$ ). The thermal signals received from the detector and amplified from the RF-lock in amplifier consist of two components: an in-phase signals  $V_{\text{in}}$  and an out-of-phase signals

$V_{out}$ . Negative in-phase signals divided by out-of-phase signals would be the normalized ratio data,  $\text{Ratio} = V_{in} / V_{out}$ .

We fit the models using the ratio of the in-phase to out-of-phase because fitting with ratio is much more robust.<sup>185</sup>

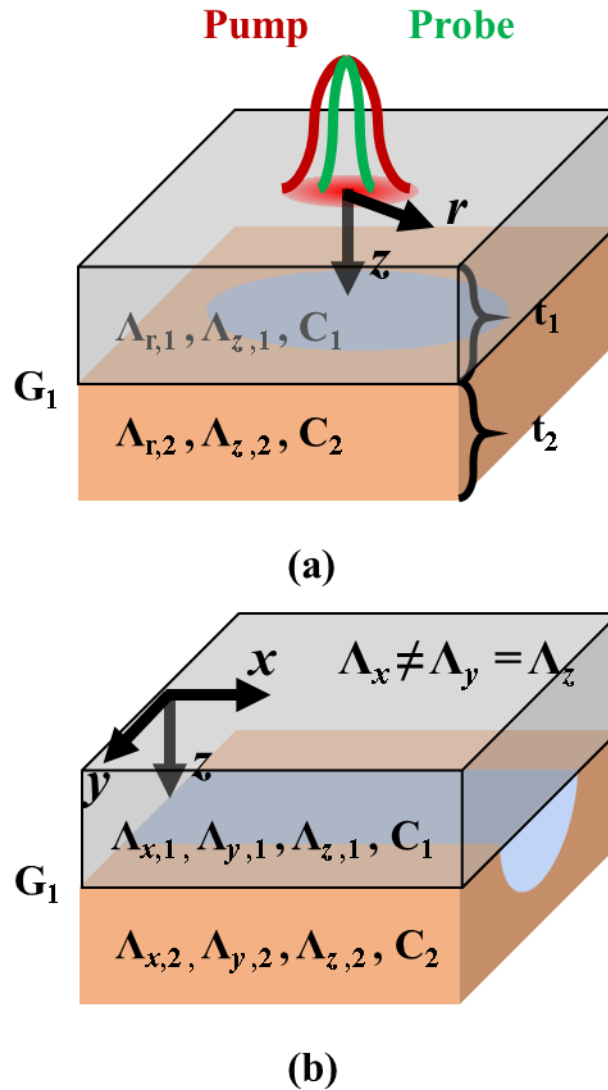


**Figure 5.3.** The schematics for the polymer sample for thermal modeling of TDTR experiments. (a) the cylindrical models for the polymer fiber along the axial direction and (b) the three-dimensional model of the polymer fiber along the radial direction.

In our opinion, when we convert the raw signals ( $V_{in}$  and  $V_{out}$ ) to a certain temperature to fit the models, it might be contaminated due to several electrical noises such as the wire connections, the environmental vibrations, and the laser pulsed laser noises. The ratio cancels this out by making the normalized value.

The thermal models for the multilayer consist of the beam spot size, the power of the beam, the frequency of the laser modulation, the thermal conductivity, the volumetric capacity, anisotropy, the interfacial thermal conductance, and the layer thickness. The materials parameters among the model variables are the thermal conductivity  $\Lambda_i$ , the volumetric capacity  $C_i$ , anisotropy  $\eta = \Lambda_r/\Lambda_z$ , the interfacial thermal conductance  $G_i$  and the layer thickness  $t_i$ .

Figure 5.3a shows the schematics of the thermal models for the multilayers based on the cylindrical coordinates. Figure 5.3a shows the thermal model for the polymer fiber along the axial direction containing the important variables ( $\Lambda_i$ ,  $C_i$ ,  $t_i$ ,  $\eta$ ).

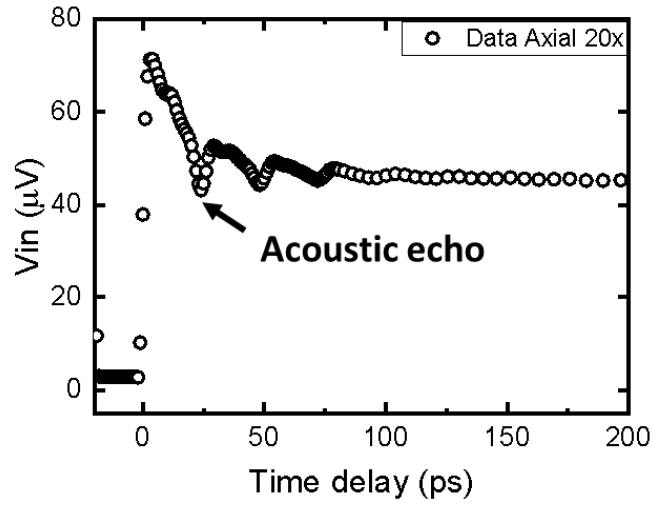
To measure the radial thermal conductivity of the polymer fiber, we should consider their high anisotropic ratio because the normal isotropic heat conduction model does not match the experimental results. Figure 5.3b shows the schematics of the thermal models for the multilayers based on the cartesian coordinates. If the thermal models of the materials are strongly anisotropic and even different along all directions, we should consider cylindrical models. Thus, we can have the thermal conductivity tensor of the multilayer models, so the modes for the radial thermal conductivity is different from the fundamental models.<sup>186</sup> The thermal conductivity along the radial direction is the same as the thermal conductivity along the  $y$  and  $z$  directions  $\Lambda_{radial}$ , and the axial that along the  $x$ -directions is different from others and is measured by the axial thermal conductivity  $\Lambda_{axial}$ . We can calculate the full thermal conductivity tensor<sup>187</sup> and the

directional thermal conductivities. The thermal conductivity tensor of the polymer fiber is written as:

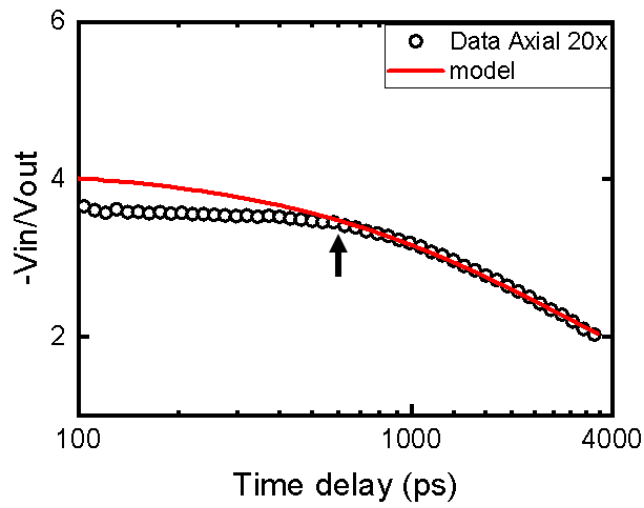
$$\Lambda_2 = \begin{bmatrix} \Lambda_x & 0 & 0 \\ 0 & \Lambda_y & 0 \\ 0 & 0 & \Lambda_z \end{bmatrix} = \begin{bmatrix} \Lambda_{\text{axial}} & 0 & 0 \\ 0 & \Lambda_{\text{radial}} & 0 \\ 0 & 0 & \Lambda_{\text{radial}} \end{bmatrix} \quad (5.2)$$

, where the subscripts axial and radial based on the fiber models and the subscripts of  $x$ ,  $y$ , and  $z$  correspond to defined in figure 5.3b. The crystalline polymer chains are following as the axial directions due to the geometry condition of the polymer fiber, and the radial polymer might have weak van der Waals interactions. By using this, we can extract the thermal conductivity of the radial thermal conductivity of the polymer fibers. We measured the frequency-dependent thermal conductivity of the Spectra 900.

Figure 5.4a demonstrates TDTR measurement of Spectra 900 fibers in the initial time to check the acoustic echo. We can characterize the thickness is  $\sim 80$  nm using the acoustic echo, and the thickness is the product of the sound of speed in materials and the time of acoustic echo. Wang *et al.*<sup>80</sup> hypothesized that these suppressed signals come from a thermoelastic effect related to the difference in the aluminum reflectivity with strain. Two layers are consisting of the metal transducer and the polymer fiber with different elastic constants. When the pump beam generates heat on the metallic layer, the metallic layer can have the lateral stress caused by the different elastic constants at the interface. This stress could be relaxed by the releasing acoustic wave related to zero-order lamb mode.<sup>80,188</sup> We can calculate the damping time of 600 ps for a beam spot size and a propagation velocity by following the ref [<sup>80</sup>]. We fit the model to the data except for the range of thermoelastic effect (by 600 ps).

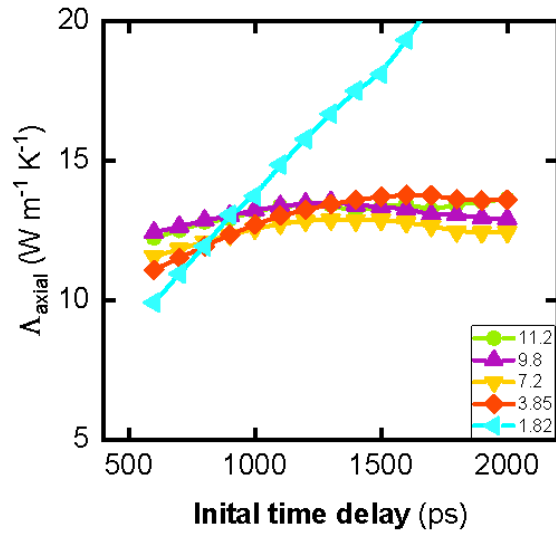


(a)

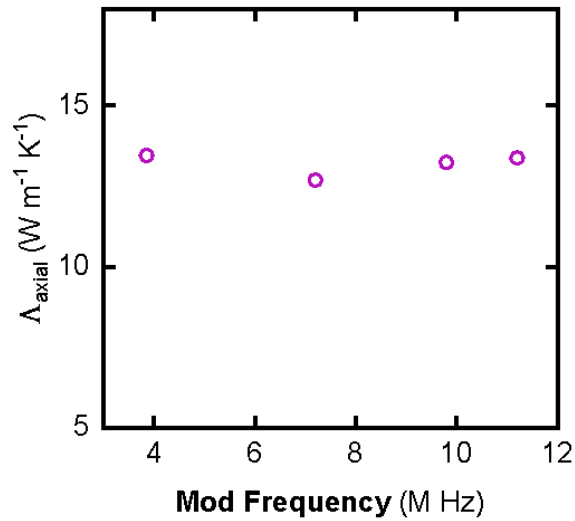


(b)

**Figure 5.4.** The experimental data using TDTR method: (a) Initial time data of the  $V_{in}$ -phase measured with 20x objective lens. The arrow indicates the acoustic echo to characterize the aluminum film thickness. (b) Whole-time period of the ratio of  $V_{in}$  and  $V_{out}$ ,  $-V_{in} / V_{out}$ . A black circle and red line is the experimental data for the Spectra 900 along the axial direction and the theoretical model, respectively. The arrow indicates the zero-order Lamb mode of the aluminum transducer at 600 ps for a 20x objective lens.



(a)



(b)

**Figure 5.5.** TDTR measurement results: (a) the initial time delay-dependent thermal conductivity of the Spectra 900 along the axial direction using the TDTR method with 20x objective lens. The  $x$  axis is the initial time for the fitting, the  $y$  axis is the extracted thermal conductivity. A green light, violet, yellow, orange, cyan line are the fitted thermal conductivity depending on the modulation frequency of 11.2, 9.8, 7.2, 3.85, 1.82 M Hz, respectively. (b) The frequency-dependent axial thermal conductivity reaching to the constant fitting values.

#### 4. Results and discussion

We have observed the frequency-dependent signal suppression in the spectra 900 along the axial direction. It clearly shows the fitted thermal conductivity because the normal fitting values should be constant depending on the fitting range. Figure 5.5a shows the initial time delay-dependent thermal conductivity of the Spectra 900 along the axial direction using the TDTR method with 20x objective lens.

When we change the fitting range, in which the initial time changes but the end time no changes, the thermal conductivity changes and reaches certain constant values in figure 5.5a. The  $x$ -axis is the initial fitting time, the  $y$ -axis is the fitted thermal conductivity using the range. The fitted thermal conductivity with the modulation frequency of 11.2, 9.8, 7.2, 3.85, 1.82 M Hz is the green light, violet, yellow, orange, cyan line, respectively. The fitted thermal conductivity with the modulation frequency of 11.2, 9.8, 7.2, 3.85 M Hz, reaches the constant fitted values at 900, 1000, 1100, 1300 picoseconds, respectively. We can also see the thermal conductivity with the modulation frequency of 1.82 M Hz cannot reach the constant values with various fitting range. It means that there is a limitation using the modulation frequency for the polymer fiber embedded in the super glue. We consider the acoustic wave related to the high-order lamb mode, but it should be generating on the high frequency of 453.3 M Hz compared with the normal operation frequency (0.2 – 20 M Hz) of our TDTR. It means that this is not related to the lamb mode signals but other effects. We checked that the beam alignment in the TDTR system, which can affect the signals, is in good status. We were not sure what kind of effects induced this suppression but guessed that the phenomena are related to the change of the thermal penetration depth, temperature gradient depending on the length, and thermal expansion because the modulation frequency changes the heat flux of the pulsed pump laser. Figure 5.5b shows the

measured thermal conductivity of the Spectra 900 along the axial direction is constant depending on the modulation frequency. This result has the similar trends to the former result.<sup>80</sup> The thermal conductivity is  $\sim 13.2 \text{ W m}^{-1} \text{ K}^{-1}$  and 6% variance compared to Wang's result, and the interfacial thermal conductance is  $\sim 100 \text{ M W m}^{-2} \text{ K}^{-1}$ , which is larger than the former reported results. Since our samples might have a much smoother surface compared with others, we can achieve higher interfacial thermal conductance along the axial direction. The frequency-dependent thermal conductivity is constant because two competing factors make the balance: phonons with the long mean free path (increase) and the phonons scattered at the amorphous region (decrease).

We measured the radial direction thermal conductivity of the Spectra 900 using three-dimensional models. Figure 5.6 demonstrates that the modulation frequency-dependent thermal conductivity of the Spectra 900 along the radial direction with a 10x and 20x objective lens.

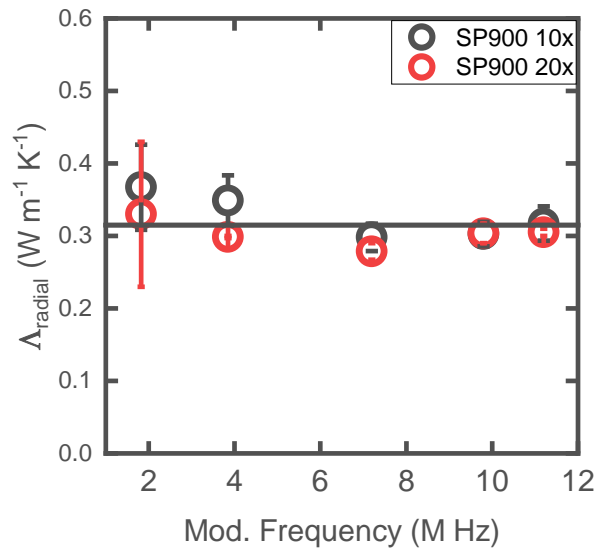


**Figure 5.6.** The modulation frequency-dependent thermal conductivity of the Spectra 900 along the radial direction using the TDTR method with 10x and 20x objective lens. The black and red line is the result with 10x and 20x objective lens, respectively.

The radial thermal conductivity is  $\sim 0.31 \text{ W m}^{-1} \text{ K}^{-1}$ , and it is a reasonable result compared to the theoretical results about the semi-crystalline PE, whose thermal conductivity is  $0.26 \text{ W m}^{-1} \text{ K}^{-1}$ . The radial thermal conductivity of the fiber is a little bit higher than the semi-crystalline PE because there are some amorphous structures among the crystalline lamellas, and its thermal conductivity is higher than that of pure crystalline along the radial direction. Compared to Lu and Liu's result, the radial thermal conductivity of the stretched Spectra 900 is less than  $0.31 \text{ W m}^{-1} \text{ K}^{-1}$  because their sample preparation causes some defects and deformation of the samples. The frequency-dependent thermal conductivity except for the low frequency is constant because two competing factors make the balance similarly as the axial results. The slight increase at the low frequency is due to a small contribution from some phonons with long mean free paths. The axial thermal conductivity is  $\sim 13.2 \text{ W m}^{-1} \text{ K}^{-1}$ , and the anisotropy ratio is more than 40, which demonstrates the Spectra 900 is high anisotropic materials (high axial thermal conductivity but low radial thermal conductivity).

## 5. Summary

In summary, we measured the thermal conductivity of the commercial high-density polyethylene fiber (Spectra 900) using the TDTR measurement. We found that the thermal conductivity along both the radial and axial direction appear constant depending on the modulation frequency, but further measurements and analysis are needed to draw any solid conclusions. We also found that the thermal anisotropy ratio of polymer fiber is  $\sim 40$ , so the Spectra 900 polymer fibers are high anisotropic materials.

## CHAPTER 6

In previous chapters, I focused on how we can improve the thermal conductivity anisotropy ratio by using the theoretical and experimental methods. All of these studies focus on how to dissipate the heat to the heat sink efficiently. We also have another strategy to decrease the power density of the nano-electronic devices. In this chapter, we will try another strategy, which is how the power density could decrease using a creative way. The idea is to use spintronics, which focus on the spin of electrons. Here, I demonstrated the mechanism of thermally driven STT using the multilayer configurations. I also showed the spin signals of electron affected by the CISS effect as a function of the temperature rise governed by the laser power, the geometrical condition of the chiral perovskite film, and the laser modulation frequency.

### 1. Introductions

Transistor based nano-electronic devices have shown rapid development over the past few decades. Their performance, however, is limited mostly by the excessive heat generation due to continuous current charge-discharge cycles. For instance, a transistor works under two states, which are '1' at current flowing and '0' and '0' corresponding to current on and off state respectively. Naturally, a higher transistor density correlates to enhanced nano-electronic device performance. Therefore, there have been attempts to incorporate more transistors into limited space to enhance computation processing and data transferring speed.<sup>30</sup>

But this approach has reached its peak in the development of the nano-electronic device because of two reasons:<sup>84</sup> (1) The extreme increase of the power density on the circuit, where the electrical charge flowing through the transistor generates heat that cannot be solved by using the

existing thermal management and (2) Decreasing the size of the transistor has reached the limitation due to quantum tunneling.

Researchers have been thinking about a new paradigm to overcome the limitations of the existing nano-electronics. One such novelty lies in utilizing the spin of electrons that is also known as the intrinsic angular momentum of electrons. The spin of electrons can be up (1) and down (0) depending on the direction of the angular momentum that acts as a switch. This spin switch can replace the existing transistor based electronics with similar performance but significantly lower heat generation.<sup>84</sup> The field of electronics where we manipulate spin to yield the desired outcome is spintronics.

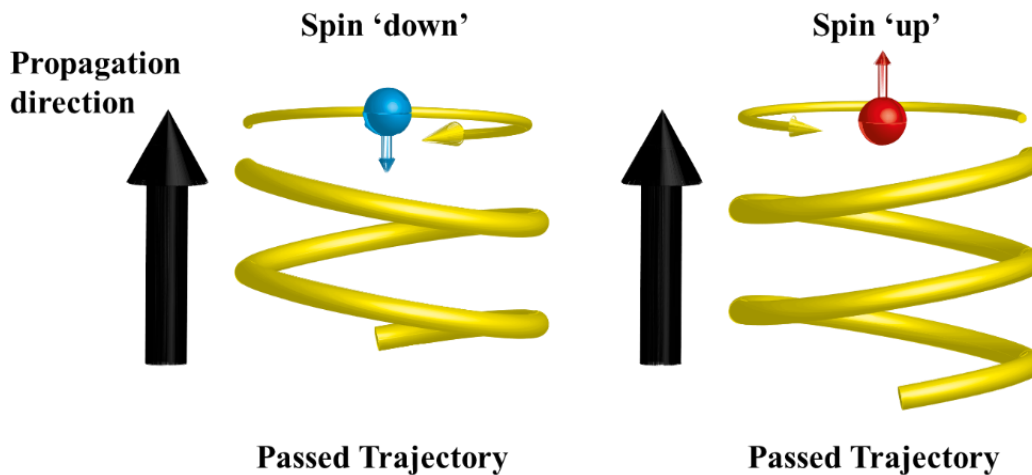
The manipulation and the generation of electron spin are the most important research topics in the spintronics.<sup>85</sup> The multi-ferromagnetic materials are used to generate the electron spin, but the miniaturization of the multi-layered materials is difficult. This is because ferromagnetic materials lose their magnetization as they get smaller in size.<sup>88,90</sup> Moreover, it is difficult to make a permanent magnetic film as well. Thus, inorganic materials for the spin devices have serious restrictions, so it is required another considerable method using organic materials.

The chiral induced spin selectivity (CISS) effect, which can create polarized spin (up or down) depending on the handedness of the spin trajectory, like spin filtering, can solve this problem because the CISS effect also occurs on nanoscale materials.<sup>189</sup> It can be more efficient compared to the ferromagnetic materials due to the small size (nanometer size). The topology of the materials with chirality has this CISS effect. The low dimensional perovskite incorporating chiral molecules is a promising organic material to generate the spin because the two-

dimensional layered structure can tend to be with more cations, which can help the more spin generation.<sup>190</sup>

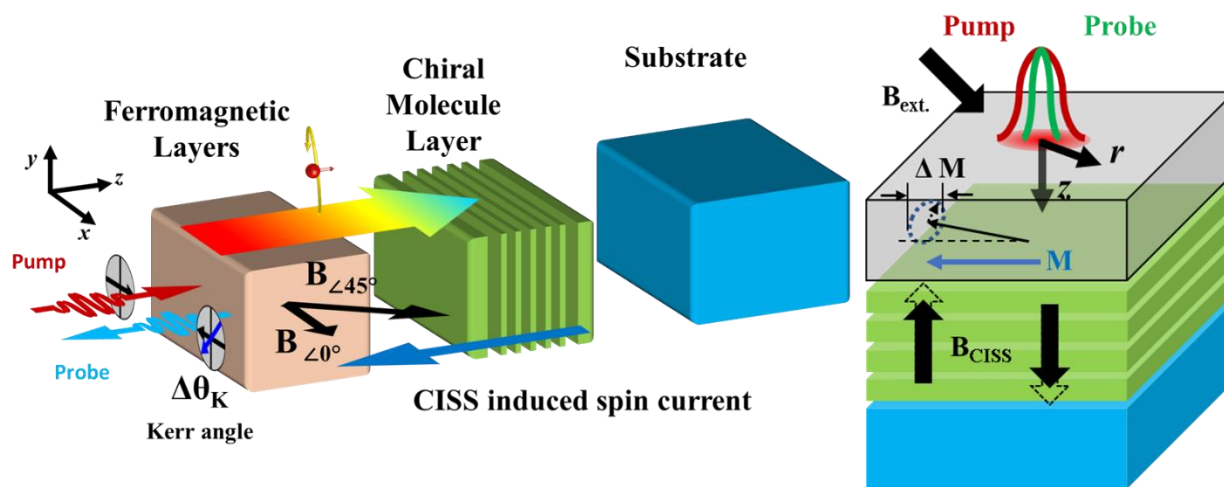
The CISS effect comes from the spin-orbit coupling (SOC), which is the transient moment of the electron spin.<sup>189</sup> The SOC generates an effective magnetic field depending on the helix shape potentials combining the propagating direction and the spin direction.

Figure 6.1 shows how the spin generates the helix shape potential with the spin states and the propagation directions. The classical view helps us to understand the concept of spin. In chemical engineering, the spin-up rotates in counterclockwise direction along the axis of an electron. When it propagates along the axis, the passed trajectories of the spins draw the helix trace, which act as the electrostatic potentials. This helix trajectory is right-handedness directions. Similarly, the helix trajectory of the spin-down is left-handedness direction, and the helix shape potentials create the effective magnetic field following the right-hand rule for curve orientation.



**Figure 6.1.** The schematic of the electron spin. The rotation direction of the spin-down is clockwise along the axis of an electron. The spin's trajectory makes the helix trace depending on the spin states and the propagating directions. The direction of the created effective magnetic field follows the right-hand rule for curve orientation.

Many researchers have tried to figure out the CISS effect. There are only steady-state experimental results of the CISS effect and theoretical model for the transient CISS effect.<sup>191</sup> However, we cannot connect the time-dependent theoretical models with the time-independent (steady-state) experimental data because there are missing parts. To demonstrate this, we will test the CISS effect of the organic-inorganic hybrid perovskite incorporating chiral organic molecules on the ultrafast time scale by using the TR-MOKE method. Moreover, we want to investigate the relation between the CISS effect and the structural topology of the perovskite incorporating chiral organic molecules such as handedness and the chiral layer's geometrical conditions contributing to the CISS effect.



**Figure 6.2.** The schematic of the magnetic precession in the TR-MOKE: The pump heats and creates a temperature gradient along the metallic surface and the chiral samples. The temperature gradient excites the electron flow, and the thermally induced CISS effect creates the spin current. If the spins inject into the metallic film, it can affect the magnetic precession. We can monitor the Kerr rotation angle ( $d\theta/dT$ ) using the TR-MOKE method. It can capture a phase changes slightly rotated plane of polarization affected by a magnetic field.

## 2. Materials and method

We use the TR-MOKE to measure the spin signals, which could be generated by the CISS effect in the organic-inorganic hybrid perovskite incorporating chiral organic molecules. The time-resolved magneto-optic Kerr effect (MOKE) is the tools visualize the change of magnetic states by using reflected light from magnetized materials (figure 6.2). We use a pump and probe techniques, and the time resolution is 0.5 ps. We used the mode locking Ti:Sapphire pulsed laser with the repetition rate of 80 MHz. We modulate the pulsed pump beam using an electrical optical modulator (EOM) at several modulation frequencies including at 1.82, 3, 3.85, 5, 7.2, 9,8 M Hz. We also modulate the probe beam using the mechanical chopper with the frequency of 200 Hz to eliminate the  $1/f$  noise dominant until several hundred Hertz. The pump power varies from 5 to 20 mW, and the probe power is 9 mW before the 10x objective lens.

The pump heats the metallic film and creates a temperature gradient on the metallic surface and the chiral samples. The temperature gradient generated by the pump beam excites the electron flow near the chiral layers. The CISS effect makes the electrons spin-polarized, which means it creates the spin current, in the chiral samples. The TR-MOKE method<sup>192</sup> visualizes the time-domain Kerr signals of the reflected probe beam, which contains a dynamic spin accumulation<sup>193</sup> thermally generated by the CISS effect using the TR-MOKE method.

The organic-inorganic hybrid perovskite incorporating chiral organic molecules are  $\text{PEA}_2\text{PbI}_4$  with R- and S-phenylethyl ammonium lead iodine (R - $\text{PEA}_2\text{PbI}_4$  and S- $\text{PEA}_2\text{PbI}_4$ ) provided by Yuo's group in figure 6.3a. Figure 6.3a (i) shows when the de-phased group of spins pass through the S-chiral, only the up-spin is filtered out. . Similarly, the spin-down is filtered out and the up-spin passes through for the R-chiral samples. Figure 6.3a (ii) shows that the

PEA<sub>2</sub>PbI<sub>4</sub> with R- and S-phenylethyl ammonium lead iodine (R -PEA<sub>2</sub>PbI<sub>4</sub> and S-PEA<sub>2</sub>PbI<sub>4</sub>) has magnetic anisotropy along the through-plane direction.

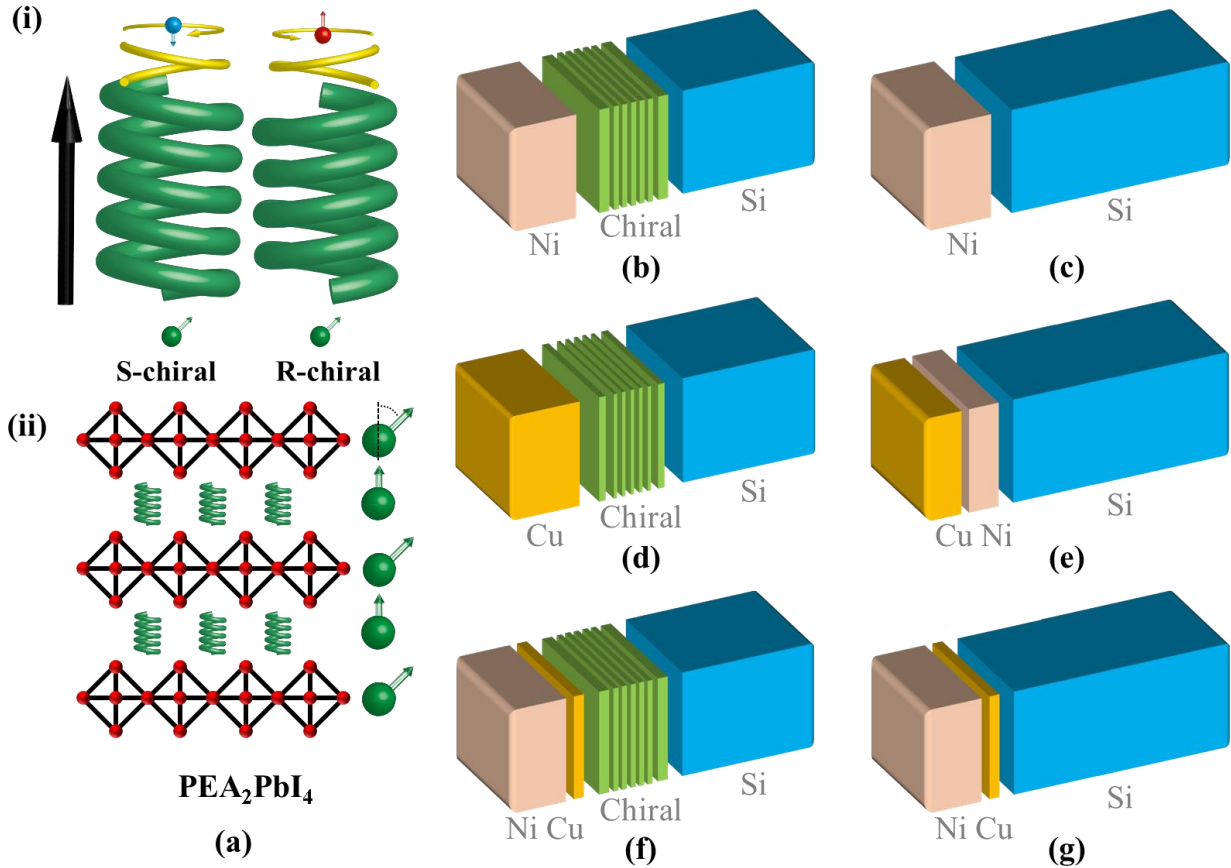


**Figure 6.3.** The schematic of the chiral molecules and control samples. (a) The chirality of the S-chiral (left-handedness) and R- chiral (right-handedness)- (i) From the de-phased group of spins, the S-chiral selects the down-spin but filters the up-spin, whereas the R-chiral selects the up-spin but filters down-spin. (ii) The PEA<sub>2</sub>PbI<sub>4</sub> with R- and S-phenylethyl ammonium lead iodine (R -PEA<sub>2</sub>PbI<sub>4</sub> and S-PEA<sub>2</sub>PbI<sub>4</sub>) has magnetic anisotropy along the through-plane. (b) Ni deposited chiral sample on the silicon substrate. (c) Ni deposited the silicon substrate. (d) Cu deposited chiral sample on the silicon substrate. (e) Cu (100 nm) and Ni (50 nm) deposited the silicon substrate. (f) Ni (80 nm) and Cu (10 nm) deposited chiral sample on the silicon substrate. (g) Ni (80 nm) and Cu (10 nm) deposited the silicon substrate.

The sample is a two-dimensional inorganic and organic hybrid sample incorporating chiral molecules, so the two-dimensional hybrid perovskite can have much more cation to generate the electron spins than the other dimensions. Moreover, it possesses a higher magnetic anisotropy. The chiral sample with the deposited nickel film can react to the air and degrade under the exposure of the light and atmosphere.

To prevent the oxidization and the degradation of the sample from the air and light, we put our samples in the vacuum chambers with the negative pressure of  $10^{-6}$  -  $10^{-7}$  bar. The incident laser beams (pump and probe) pass through the beam splitter and the quartz window in the chamber, so its power could decrease ~50 %. The optical filter removes the pump beams and only allowing probe beam to pass. The filtered probe beam from the optical filter is separated and orthogonally polarized through a half-wave plate and the Wollaston prism.

Figure 6.3 b-g shows the schematic of the chiral molecules and control sample. The chiral samples are in figure 6.3b, d, and f. The control samples are in the figure 6.3c, e, and g. Figure 6.3b and c show the Ni deposited samples, and figure 6.3d show the copper layer on the samples. Figure 6.3 shows the copper layer with a thickness of 100 nm and the nickel layer with a thickness of 50 nm on the silicon substrate. Figure 6.3g and h shows that the nickel with a thickness of 80 nm and the copper with a thickness of 10 nm deposited chiral sample on the silicon substrate.

To monitor the time-dependent experimental data, we measure the TR-MOKE signals by subtracting the polarized and the other polarized in the in-phase and out-of-phase by using the balanced detectors, showing the **time-domain picosecond magnetic precession** signals affected by the CISS effect. To figure out **the mechanism of the CISS effect** of the chiral samples, we build the several types of the metallic deposited chiral and control samples: (1) We conducted

control samples measurement to confirm whether the magnetic precession is solely due to CISS effect. The control sample is the ferromagnetic Ni film on a Si substrate without the chiral molecule layer. We predicted that the Ni film might be influencing the magnetic precession due to ferromagnetic demagnetization. Thus, the comparison between the control sample and Chiral samples will help decouple the ferromagnetic demagnetization from CISS effect. (2) We want to see and predict the thermally induced spin accumulation effect at the non-magnetic film metallic (Cu) film (Figure 6.3d and e). A copper layer with a thickness of 100 nm and the nickel with a thickness of 50 nm are deposited over both chiral samples on the silicon substrate (Figure 6.3d) and control samples (Figure 6.3e). We predict that there are no magnetic precession signals affected by CISS effect, but only the thermally induced spin accumulation signals. (3) We want to find out which is the dominant mechanism causing magnetic precession signals, the CISS effect or the interfacial effect between the ferromagnetic layer and chiral layers. We predicted that if the interfacial effect influences the precession signals, the nickel with a thickness of 80 nm and the copper with a thickness of 10 nm deposited chiral sample on the Si substrate cannot show any signals like the Ni deposited chiral sample on the Si substrate (Figure 6.3f and g).

### **3. Results and discussion**

#### **A. TDTR signals of the chiral molecules**

In TDTR measurement, we found that the ratio( $-V_{in}/V_{out}$ ) of the R- chiral sample is different from that of the S- chiral sample. We thought that the thermal properties including thermal conductivity and heat capacity of the chiral sample would be similar each other (R- and S-), so the difference in ratio comes from the thickness of the samples. We measured the TDTR signals of the chiral samples with the nickel film on the silicon substrate in figure 6.3b.

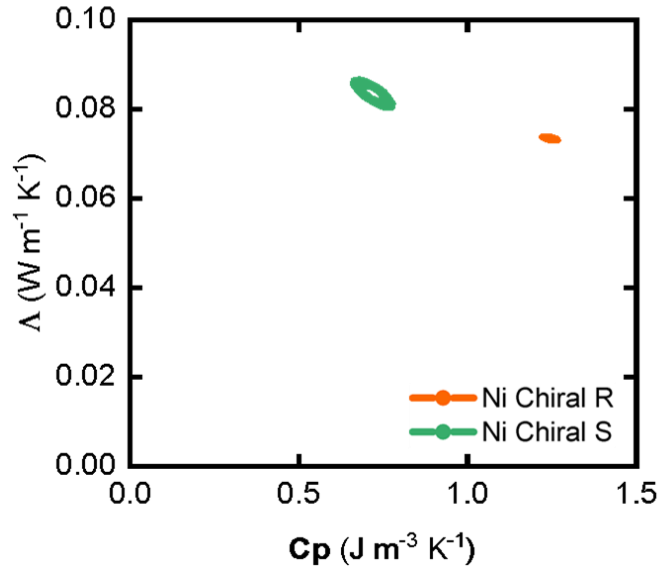


**Figure 6.4.** Contour map derived from the fitting quality of the TDTR data as a function of thermal conductivity and heat capacity. The orange and the green is the thermal conductivity of the R- and the S- chiral sample, respectively.

We characterized the thermal conductivity and heat capacity of the chiral molecule samples. We used the sum of the standard deviation ( $\sigma_{\text{fit}}$ ) between the model prediction and the measurement data for fitting.<sup>194</sup>

Figure 6.4 shows the contour of constant  $\sigma_{\text{fit}} = 2\sigma_{\text{fit, min}}$  with the confidence of 95% as function of the thermal conductivity and the volumetric heat capacity. The thermal conductivity of the R- and S- chiral sample is  $0.08 \pm 0.02 \text{ W m}^{-1} \text{ K}^{-1}$  and  $0.07 \pm 0.01 \text{ W m}^{-1} \text{ K}^{-1}$ , respectively. The heat capacity for the R- and the S- chiral sample is  $1.24 \pm 0.03 \text{ J m}^{-3} \text{ K}^{-1}$  and  $0.72 \pm 0.05 \text{ J m}^{-3} \text{ K}^{-1}$  respectively.

### **B. TR-MOKE signals with the in-plane magnetization**

In the TR-MOKE method, when the pulsed pump beam creates the temperature gradient into the ferromagnetic materials deposited over the chiral layers on the silicon substrate, the ferromagnetic layer is demagnetized in the plane, and the chiral molecule layer is thermally

activated. The spin loss by the demagnetization converts to the spin generation. The spin diffusion equation of the ferromagnetic layer on the chiral molecules can be expressed as

$$\frac{\partial \mu_s}{\partial t} = D \frac{\partial^2 \mu_s}{\partial z^2} - \frac{\mu_s}{\tau_s} + \left( \frac{g_s}{N_s} \right) \quad (6.1)$$

, where  $\mu_s$  is the spin chemical potential,  $D$  is the spin diffusion constant,  $\tau_s$  ( $=l_s^2/D$ , where  $l_s$  is the spin diffusion length) is the spin relaxation time,  $g_s$  is the spin generation rate,  $N_s$  is the spin density of states with the electronic density of state of the chiral molecule layer ( $N_s = 0.5 N_{FM}$ ).  $D = \sigma / (e^2 N_F)$ , where  $\sigma$  is the electrical conductivity and  $N_F$  is the density of states at the Fermi level,  $N_F = 3\gamma / (\pi^2 k_B^2)$ , where  $\gamma$  is the electronic heat capacity coefficient, and  $k_B$  is the Boltzmann constant. The thermally induced demagnetization spin generation rate  $g_s = -dM/dt$  at the chiral molecule layer.

The temperature gradient affects the chiral molecule films, and the thermally induced CISS effect creates the spin current and injects it into the ferromagnetic layer (figure 6.2). This leads to the thermally induced spin-transfer torque (STT), which is the transfer of the spin angular momentum to the magnetized ferromagnetic layer, manipulating the nanomagnets with the spin current. The ultrafast spin transfer torque can be described using the TR-MOKE method. A modified Landau-Lifshitz-Gilbert (LLG) equation with an additional term can be expressed as:

$$\frac{\partial \mathbf{M}}{\partial t} = -\gamma (\mathbf{M} \times \mathbf{B}_{eff}) + \alpha \mathbf{M} \times \frac{\partial \mathbf{M}}{\partial t} + \frac{J_{s,CISS}}{M_s h} \mathbf{M} \times (\mathbf{M} \times \mathbf{B}_{CISS}) \quad (6.2)$$

, where  $\gamma$  is gyromagnetic ratio,  $\mathbf{M}$  is the magnetization of the ferromagnetic layer,  $\mathbf{B}_{eff}$  is the effective magnetic field,  $\alpha$  is the Gilbert damping constant,  $J_{s,CISS}$  is the spin current caused by the thermally induced CISS effect and obtained by the equation (2),  $\mathbf{B}_{CISS}$  is the effective magnetic field of the chiral film depending on the thermally induced chiral film, and  $M_s$  and  $h$  are the saturation magnetization and the thickness of the ferromagnetic layer, respectively.

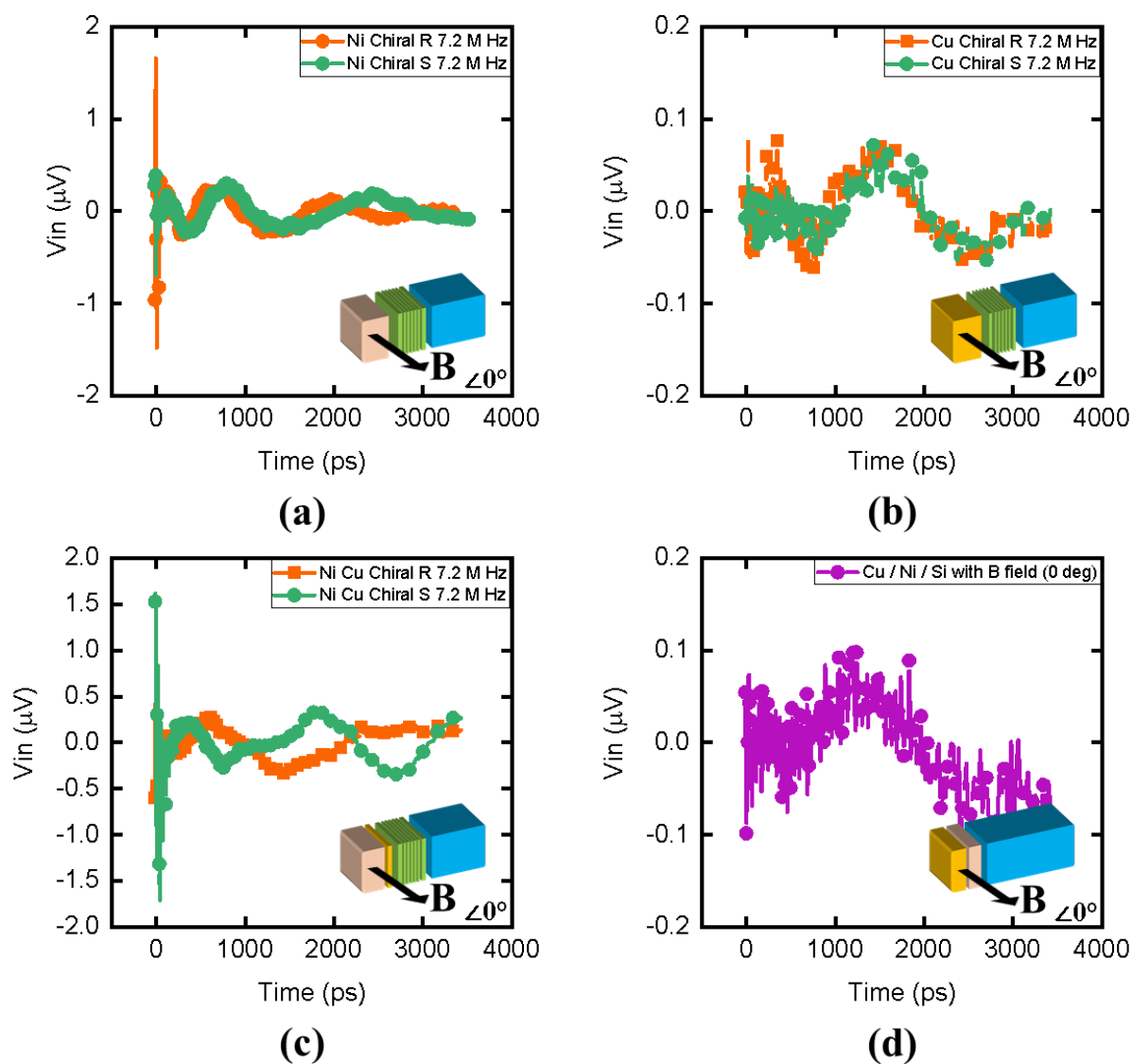


**Figure 6.5.** The magnetic precession signals after in-plane magnetization of (a) the nickel deposited chiral samples on the silicon substrate, (b) the copper (100 nm) deposited chiral samples on the substrate, (c) the nickel (80 nm) and copper (10 nm) deposited chiral samples on the silicon substrate, and (d) the copper (100 nm) and nickel (50 nm) film on the silicon substrate. The measured voltage ( $\mu V$ ) is the  $y$ -axis, and the delay time (ps) is the  $x$ -axis. The modulation frequency of the pump laser is 7.2 M Hz. The orange and the green dot line is the R- and S- sample, respectively.

We measure the TR-MOKE signals of the chiral samples and one control sample (Cu and Ni film) with the nickel film on the silicon substrate in figure 6.3b, d, e, and f. We applied the magnetic field along the in-plane direction and measure the TR-MOKE signals in Figure 6.5.

Figure 6.5 shows the magnetic precession signals after in-plane magnetization of the samples with the pump laser modulation frequency of 7.2 M Hz. The measured voltage ( $\mu V$ ) is the  $y$ -axis, and the delay time (ps) is the  $x$ -axis in all figures. The original raw data contains the thermal background noise, that the balanced detector does not remove. Thus, we removed the thermal background signals by subtracting the exponential decay equations. Figure 6.5a shows the TR-MOKE signals of the nickel deposited chiral samples on the silicon substrate. We can observe the sinusoid signals with the frequency  $\sim 1$  G Hz, and the R- and S- chiral molecules signals starts to shift, and the signals shows the  $\pi/2$  phase shift after 2000 ps. We found that there are two main frequency components using the fast Fourier transform (FFT) analysis.

Figure 6.5b shows the wave signals of the copper (100 nm) deposited chiral samples on the silicon substrate. Both R- and S- show the similar wave trends with no phase shift. We claim that these are spin accumulation contribution in the TR-MOKE signals because the copper is non-ferromagnetic material, so there cannot be magnetization in the film. The frequency of the signals is  $\sim 0.5$  G Hz. The magnitude of the signals is five times weaker than the magnetic precession signals generated by the CISS effect. This further supports our claim that these signals are due to spin accumulation.

We have observed the sinusoid signals at 1 GHz in figure 6.5a, and we predict that this is the polarized spin signals affected by the CISS effect. It is also possible that the ferromagnetic and non-ferromagnetic interface influence the signals, so we want to confirm whether the thermally induced CISS effect or the interface between the nickel and the copper films

generate the signals. To figure this out, we built the nickel (80 nm) and copper (10 nm) deposited chiral samples. We can see the TR-MOKE signals of the Ni (80 nm) and Cu (10 nm) deposited chiral samples on the silicon substrate in figure 6.5c. As the TR-MOKE signals with 1 GHz are clearly observed in the figure, we confirmed that the thermally induced CISS effect generates the signals.

Finally, we also measured the control sample, which is the copper (100 nm) and nickel (50 nm) film on the silicon substrate in figure 6.5d. The copper and nickel films on the Si substrate show lower frequency TR-MOKE signals, and its trend is similar to the copper deposited sample's signals. It means that the signals are not the polarized spin accumulation affected by the CISS effect, but the nickel precession signals, and they lost the CISS effect through the copper samples.

The Ni film without the chiral molecule film generates the electrons, and the other magnetized layer produces a few polarized spins following its magnetization directions, so we can detect the spin accumulations signals without the CISS effect. It is a counter evidence that the signals we observed in figure 6.5a and c is the precession signals affected by the CISS effect.

### **C. TR-MOKE signals with the in-plane magnetization depending on the modulation frequency and the heating laser power**

To characterize the detailed mechanism of the CISS effect of the chiral molecule samples based on the thickness, we change the thermal penetration depth using the different pump laser modulation frequency. We also change the temperature rise using the different heating laser power to characterize the temperature rise dependency of the samples. The thermal penetration depth is  $d_p \sim \sqrt{1/f_{\text{mod}}}$ , where  $f_{\text{mod}}$  is the modulation frequency (Hz). We used the nickel and copper samples in figure 6.3f to observe the modulation frequency-dependent TR-

MOKE signals. For the two-dimensional perovskite chiral samples, we predicted that the CISS effect would be more pronounced with increasing thermal penetration depth. This can be attributed to the increase in number of cations generating electron spin as we excite more 2D perovskite-chiral layers. We varied the modulation frequency of the pulsed pump laser between 1-10 MHz at a 20 mW pump power. For power dependent CISS effect measurement, the pump power ranges between 5-20 mW at 7.2 MHz modulation frequency. The lower thermal conductivity of the chiral samples leads to a larger temperature gradient.

We magnetized the Ni film along the in-plane applying the in-plane magnetic field. If the CISS effect influences the observed magnetic precession, the signals show a phase changes depending on the chirality. We predict that when we increase the temperature and the thermal penetration depth, the amplitude of the signals can increase due to the thermally activated chiral films.

Figure 6.6 shows the power dependent and frequency dependent CISS effect experimental results. We analyze the data using the FFT analysis and extract the main amplitude and the frequency. Figure 6.6a and b shows the amplitude of the Ni / chiral sample. The light orange and the light green line is the signals of the chiral R- chiral samples and the chiral S-samples on the silicon substrate, respectively. Figure 6.6a shows the both signals of the R- and S-samples increases depending on the pump laser power. The temperature rise caused by the heating laser increases with the pump power thereby increasing the thermally CISS induced spin current. The modulation frequency shows the different trend each other in figure 6.6b. As we predict, the precession affected by the CISS effect is power dependent. However, the precession seems to be the modulation frequency-dependent in R but not S.

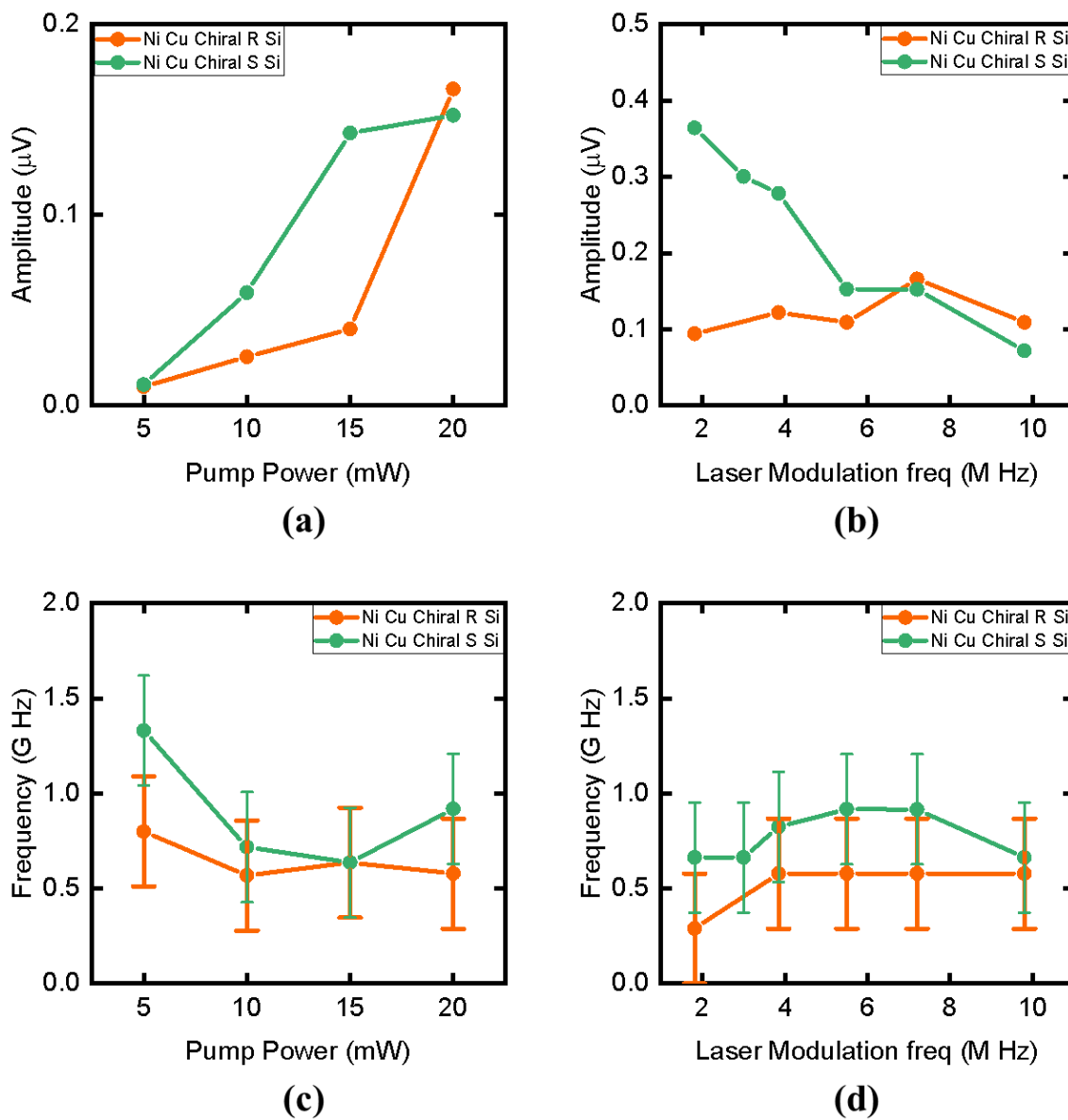


**Figure 6.6.** The analysis of the TR-MOKE signals with different power and different frequency of the pulsed pump laser: The power dependence of (a) the amplitude and (b) the frequency of the precession signals with the modulation frequency of 7.2 M Hz. The modulation frequency dependence of (c) the amplitude and (d) the frequency of the precession signals. The light orange colored line is Ni / Cu / Chiral **R- chiral** samples on the silicon substrate, and the light orange colored line is Ni / Cu / Chiral **S- chiral** samples on the silicon substrate.

The thermal gradient activates the CISS effect, so the film of the S-chiral sample is thinner than that of R, and the penetration depth at high modulation frequency is deeper than the thickness of the chiral film because the penetration depth decreases when increasing the modulation frequency. The amplitude of R-chiral increases marginally until 15mW but rises substantially at 20mW. The reason is that the smaller thickness of the R- chiral as compared to that of the S-chiral. The small thickness explains the frequency dependence CISS effect in the R-chiral and the S- chiral samples. For the R-chiral samples, as the thickness is low, all the layers contribute to CISS induce current, particularly at low modulation frequencies that result in nearly constant amplitude until 7.2 M Hz. The thicker S- chiral samples, on the other hand, show observable variation in amplitude with power and modulation frequency. Further, the frequency data implies that the main signal frequency of the S sample is larger than that of the R- sample because the magnitude of the CISS effect is larger in the S- sample.

#### **D. TR-MOKE signals with the 45-degree external magnetic field**

We applied the 45-degree external magnetic field to the control (Ni / Si) sample figure 6.3c, and figure 6.7 shows the magnetic precession signals of the control samples with various external magnetic fields. The negative applied magnetic field-dependent signals are from 10 to 90 mT in figure 6.7a, and the positive field is from 10 to 90 mT. The power of the pulsed pump beam is 20 mW, and that of the probe beam is 9 mW in the experiments. The plus and minus symbols indicate the direction of the applied magnetic field in all figures. Figure 6.7a and b shows the short damp signals with the frequency of 4-10 G H from 0 to 1000 ps and the long damp signals with the frequency 0.5 G Hz in whole time.

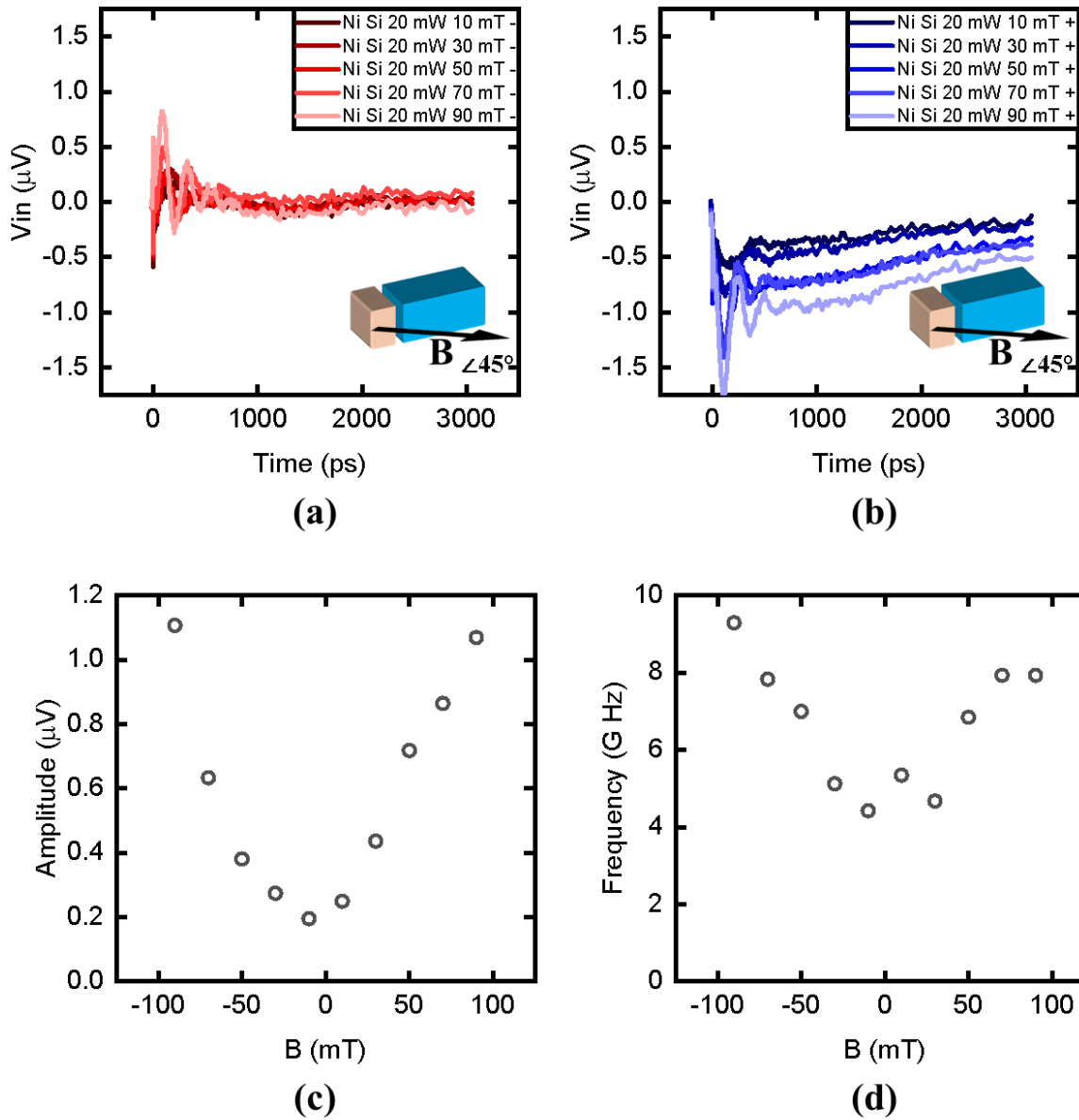


**Figure 6.7.** The magnetic precession signals of the nickel film on the silicon substrate with (a) the negative magnetic field-dependent signals from 10 to 90 mT and (b) the positive magnetic field-dependent signals from 10 to 90 mT. The pump power is 20 mW, and the probe power is 9 mW in the experiments. The plus and minus symbols indicate the direction of the applied magnetic field. (c) The amplitude of the first oscillation from the signals. (d) The frequency of the oscillation signals.

The short damp signals are the cross-plane magnetization signals, and the long damp signals are the in-plane magnetization signals. The magnetization negative and positive field is the up-ward (figure 6.7a) and down-ward (figure 6.7b) signals, respectively. We analyze the amplitude and the frequency of the signals using the FFT method.

The strong fields show the high amplitude of the signals, and the amplitude with the positive and negative fields is symmetric in figure 6.7c. The reason is that the magnetic precession is proportional to the field strength, and there is only the nickel magnetization signals. The frequency data is also symmetric in figure 6.7d. We can observe the amplitude and the frequency are proportional to the field strength with the positive and the negative directions.

We tested the nickel deposited and the nickel and copper deposited chiral sample (figure 6.8). To remove the signal noise, we averaged the data until the signal-to-noise ratio is larger than 50. The number of averaged data points is roughly over 15.

Figure 6.8 shows the time-domain magnetic precession signals of each samples applied both the negative and positive 45-degree external magnetic fields from 10 to 90 mT. We use the pump power of 20 mW and the probe power of 9 mW with the modulation frequency of 7.2 MHz. the plus (+) and the minus (-) symbols indicate the direction of the applied magnetic field. The CISS effect induced precession signals can be observed at a frequency of 1-2 GHz over the entire time period. Most of the signals are similar to the ones for in-plane magnetization as shown in figure 6.5a and c. The amplitude of the signals influenced by the CISS effect changes depending on the 45-degree external field strength. The short damp signal from 0 to 500 ps observed in the 70 and 90 mT fields is the in-plane nickel precession.

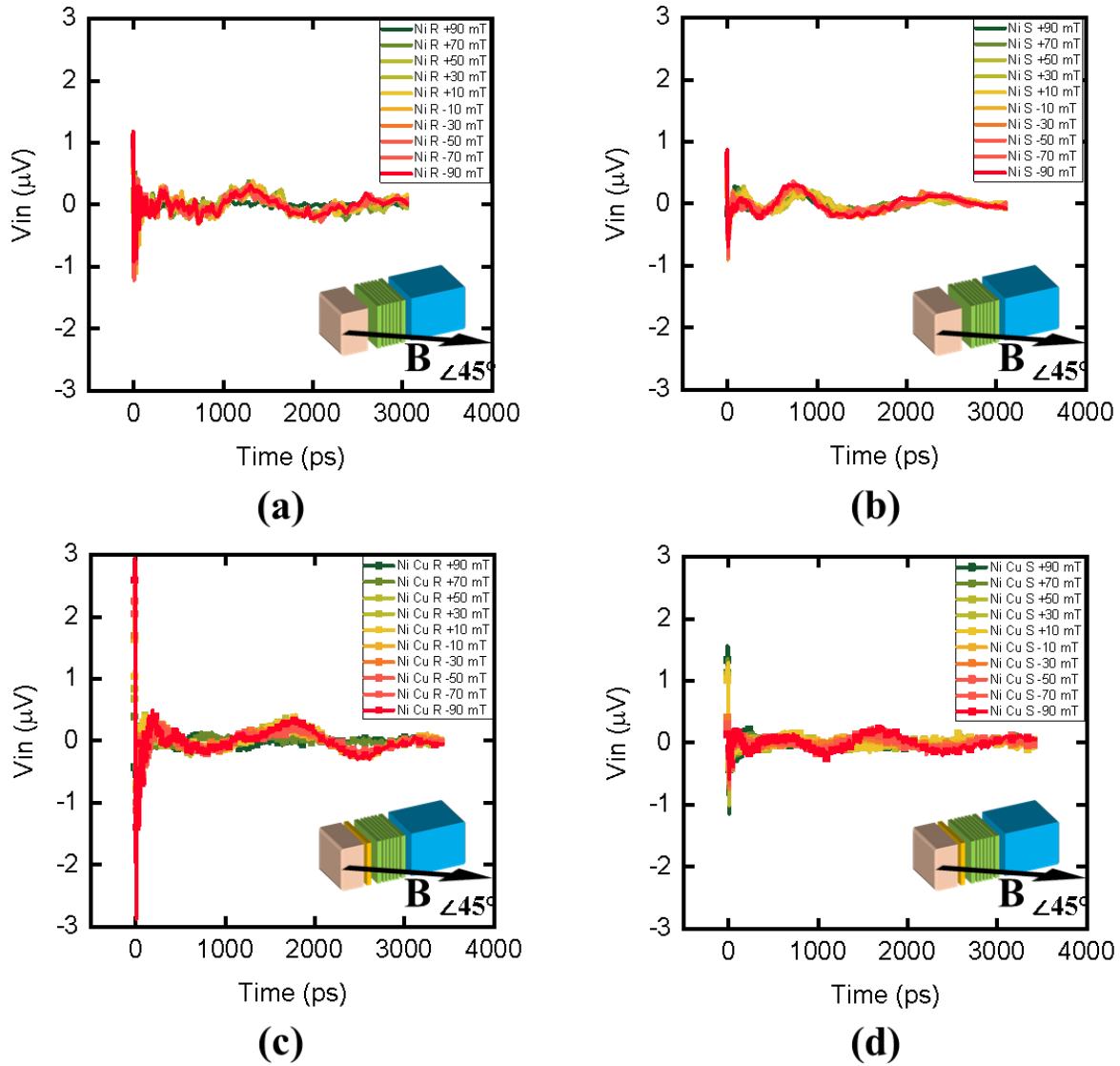


**Figure 6.8.** The time-domain magnetic precession signals of (a) the nickel deposited R-chiral sample on the silicon substrate, (b) the nickel deposited S-chiral sample on the silicon substrate, (c) the nickel and copper deposited R-chiral sample on the silicon substrate, and (d) the nickel and copper deposited S-chiral sample on the silicon substrate applied both the negative and positive 45-degree external magnetic fields from 10 to 90 mT. The pump power is 20 mW, and the probe power is 9 mW in the experiments. The plus (+) and the minus (-) symbols indicate the direction of the applied magnetic field.

The amplitude of the signals of the Ni / chiral and the Ni / Cu chiral sample has no difference. Interestingly, the signals of the Ni / Cu / chiral sample are much clearer than that of the Ni / chiral sample. We think that the thin copper layer serves as the signals filter to remove the interface noise. Moreover, the interface between the chiral molecules and the nickel film might be high resistive.

The Ni / R- chiral and S- chiral show the  $\pi$ -shifted signals for the whole time. The Ni / Cu / R- chiral and S- chiral show the  $\pi$ -shifted signals from 0 to 1000 ps. After 1000 ps, the signals of the Ni / Cu / R- chiral and S- chiral have similar phase. It seems to be the precession signals changes their phase via the non-ferromagnetic materials. We thought that the state of the electron spin is constant, but they can be transient in the non-ferromagnetic materials because the force of the CISS effect decreases far from the chiral film in non-ferromagnetic materials.

We analyze the amplitude and the frequency about the signals of Ni / chiral and Ni / Cu/ chiral sample using the FFT method in figure 6.9. The amplitude of the Ni / chiral sample in figure 6.9a and b is not symmetric. We cannot directly compare the R- and S- sample because they have different geometric conditions, which influence the thermally induced CISS effect. We can see how the peak values are distributed based on the field strength. In figure 6.9a, the peak values of the nickel deposited R- chiral samples are at -10 mT and +70 mT, but those of the nickel deposited S- chiral sample are at -50 mT and 30 mT. The amplitude of the control samples (Ni / Si) is symmetric, but that of the chiral samples shows asymmetry. The R- sample is biased towards right, and the S- sample biased leftwards.

In figure 6.9b, the entire trend of the nickel and copper deposited R- and S- shows is proportional to the negative external field but reversely proportional to the positive fields. The peak values of R- chiral are at -30 mT and +50 mT while those of S- chiral are at -90 mT and

over 10 mT. The bias of the nickel and copper deposited sample is similar to that of the nickel deposited sample: The R- sample biased towards right, and the S- sample biased towards left.

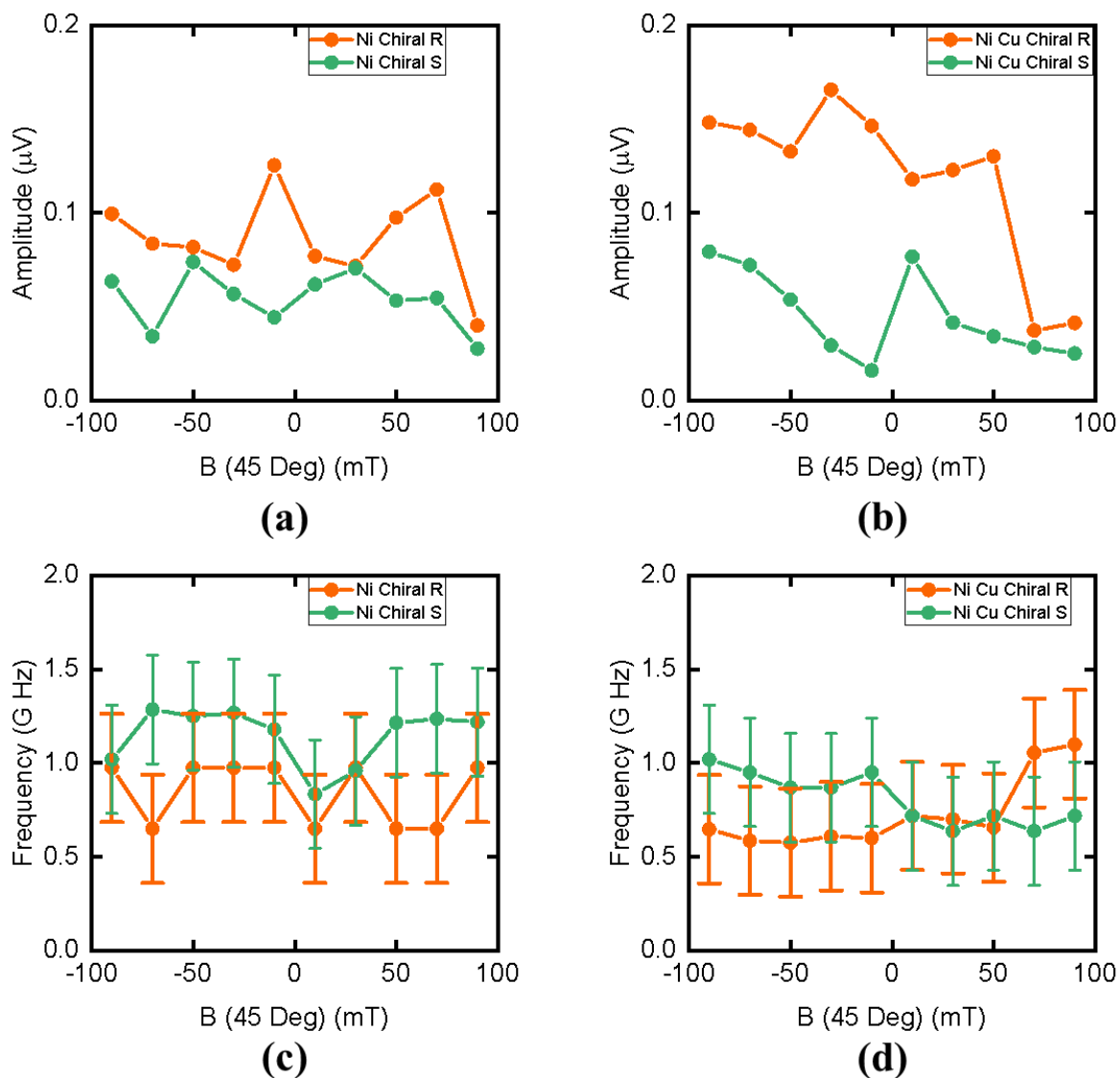


**Figure 6.9.** The FFT analysis result: The amplitude of (a) the nickel deposited chiral sample and (b) the nickel and copper deposited chiral sample on the silicon substrate. The frequency of (c) the nickel deposited chiral sample and (d) the nickel and copper deposited chiral sample on the silicon substrate.

Figure 6.9c shows the FFT frequency of the nickel deposited sample. most frequencies of the S- chiral sample is higher than that of the R- chiral sample. The field strength- dependence is not clear because the resolution of the FFT frequency is  $\sim 0.3$  G Hz.

Figure 6.9d shows the frequency of the nickel and copper deposited chiral sample. In the negative field strength, the frequency of the S- chiral sample is higher than that of the R- chiral sample. In the strong positive field strength, the frequency of the R- chiral sample is higher than that of the S- chiral sample, but the frequency of the R- and the S- chiral samples are similar in the weak positive field strength. The field strength-dependence is not clear because of the high uncertainty, but we can say that the frequency of the signals affected by the CISS effect is from 0.8 to 1.2 G Hz. We made the 2D contour plot of the amplitude and the frequency depending on both the laser power and the 45-degree field strength of the nickel deposited the chiral sample in figure 6.10. The  $x$ -axis is the 45-degree external magnetic field strength, where the plus (+) is the positive and the minus (-) is the negative field, and the  $y$ -axis is the pump laser power.

Figure 6.10a and b demonstrate the 2D contour amplitude of the nickel deposited R- chiral and S- chiral samples, respectively. The peak amplitudes (red contour area) in figure 6.10a are right-biased, and those in figure 6.10b left- biased. The third peak is observed in the condition with the pump power of 20 mW and positive field strength of 90 mT in figure 6.10a and b. This might be the high-order harmonic frequency components in the signals. The 2D contour signal frequency plot of the nickel deposited R- chiral and S- chiral sample is figure 6.10c and b, respectively. Interestingly, the frequency follows the opposite trend compared to the amplitude. The signals with the weak magnetic field and the weak heating power tends towards high frequency, similarly for nickel precession because the CISS effect cannot be thermally induced under this condition.

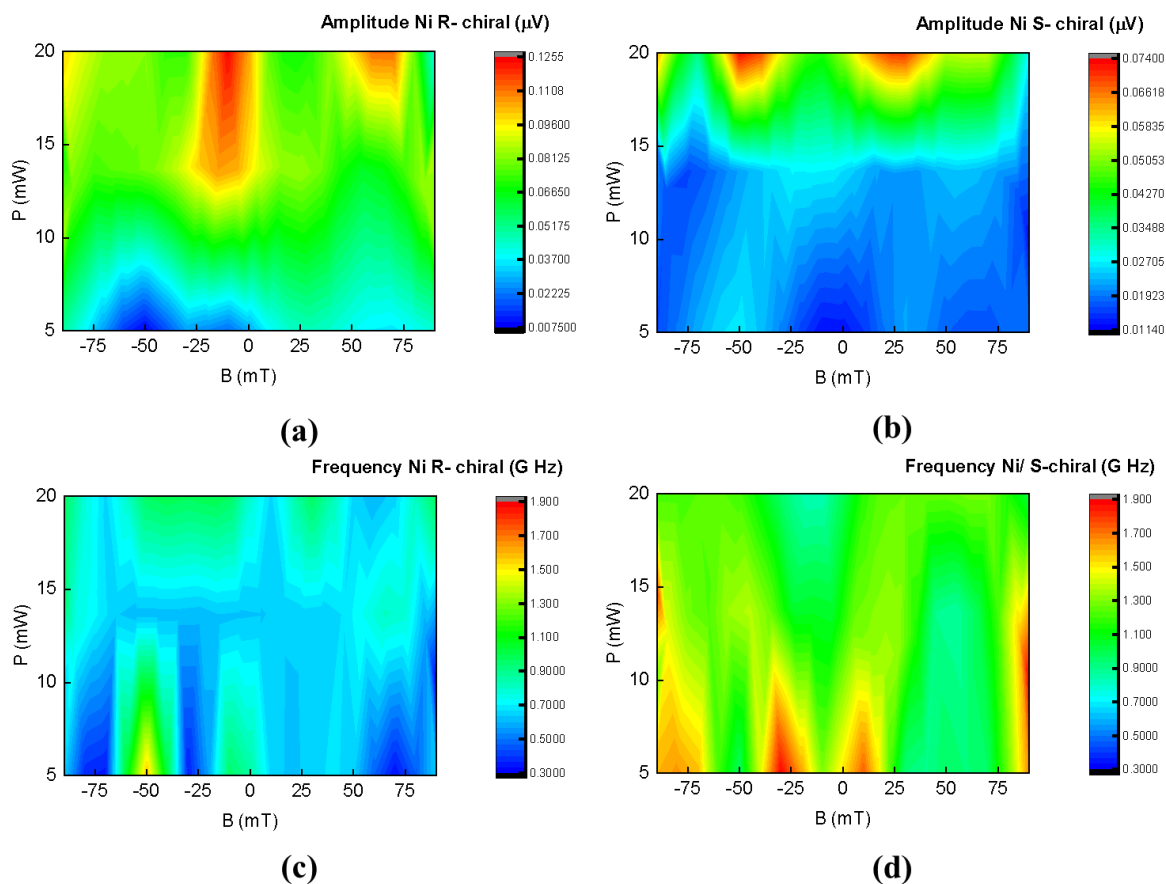


**Figure 6.10.** The 2D contour plot of the amplitude of (a) the nickel deposited R-chiral and (b) S-chiral sample. The 2D contour plot of the signal frequency of (c) the nickel deposited R-chiral and (d) S-chiral sample. The x-axis is the negative and positive 45-degree external magnetic field strength, and the y-axis is the pump laser power.

#### 4. Summary

In this chapter, I tested various deposited film on the chiral molecule samples to check the time-domain TR-MOKE signals of the precession signals influenced by the CISS effect and to figure the mechanism of the thermally induced CISS effect. We observed that signals of the R- and S-chiral samples show the  $\pi$ -phase shift. The amplitude of the signals is proportional to the power but follows a complicated relationship with laser modulation frequency dependence. The

laser modulation frequency is related to the thermal penetration depth, so the chiral film-thickness-dependent experiments is required in the future works. I measured the 45-degree external magnetic field strength-dependent signals to figure out the thermally induced CISS effect indirectly using the TR-MOKE techniques. I found the amplitude is biased depending on the positive and negative field strength: The R- sample biased towards left and the S- sample biased towards right. This work contributes to the novel physics of the thermally induced CISS effect of layered chiral hybrid perovskite materials.

## CHAPTER 7

This dissertation shows the theoretical and experimental studies on thermal and spin transport in various anisotropic materials. My theoretical study revealed that the most effective mass disorder is the structures with through-plane and hybrid random mass disorder. Furthermore, I studied the relationship between mass patterns and thermal transport in each layer. Many researchers have used the deep learning method to demonstrate that the most effective mass disorder pattern to reduce thermal conductivity is a random mass pattern. Thus, it is interesting to apply the deep learning method to find another pattern for the projects. Moreover, the mass disorder pattern with the small mass difference (0.5% compared to the original mass) is very similar to the isotope materials, so it is interesting to study theoretically and experimentally the carbon isotope materials based on the mass pattern study. The asymmetry of the mass distribution is an important factor to change thermal conductivity along the through-plane. Our analysis would provide new insight into the thermal management of the nanoelectronics incorporating 2D materials and van der Waals heterostructures.

I have shown experimentally to characterize the micro-sized polymer materials, which is commonly difficult to measure their thermal conductivity. I measured the thermal conductivity of the commercial high-density polyethylene fiber (Spectra 900) using the TDTR measurement and showed that the polymer fiber is a highly thermal anisotropic material. I microtomed the polymer fiber to make a smooth surface of the sample, whose roughness is less than 10 nm, and we can optically measure the flexible and tiny samples. In this microtomed method, we have faced the fitting issues for the fundamental thermal models of the TDTR. Another signal suppression caused by unknown effects except for the zero lamb mode signals bothers the model fitting. In this dissertation, I suggest a new fitting method to avoid this unknown suppression, but

it is necessary to find the physics of the suppression for the complete characterization. I predict that the suppression of the TDTR signals is related to the modulation frequency of the pulsed laser because the suppression signal time ranges expanded depending on the modulation frequency, which affects thermal diffusion. Another possibility is that simple models do not work in the microtomed materials and underestimate thermal diffusion.

Finally, I tested the fundamental mechanism of CISS effects using a few sample configurations probed by TR-MOKE. Although I figured out there are real CISS effects in the chiral molecule samples and the experimental parameters such as the laser power and the pulsed laser frequency contribution to the CISS effect, there are some future work can be done to further probe this mechanism in the two-dimensional inorganic and organic hybrid materials. Firstly, the thickness of the film is not controlled accurately by the spin coating, so there are difficulties to compare each sample. Using a crystal sample rather than a thin film sample might be a good choice. Secondly, I only showed the experimental results and trends but not demonstrated the detailed mechanism using the theoretical models. Thus, my future work is to demonstrate the physics of the thermally induced CISS effect of layered chiral hybrid perovskite materials and evaluate the efficiency based on the theoretical models. All insight on the fundamental spin transport mechanisms will be employed to advance the electron spintronics and to design the new spintronic devices to overcome the former electrical current based devices.

## REFERENCES

- 1 D. G. Cahill, P. V. Braun, G. Chen, D. R. Clarke, S. Fan, K. E. Goodson, P. Keblinski, W. P. King, G. D. Mahan, and A. Majumdar, "Nanoscale thermal transport. II. 2003–2012," *Appl. Phys. Rev.*, **1**, 011305 (2014).
- 2 D. G. Cahill, W. K. Ford, K. E. Goodson, G. D. Mahan, A. Majumdar, H. J. Maris, R. Merlin, and S. R. Phillpot, "Nanoscale thermal transport," *J. Appl. Phys.*, **93**, 793 (2003).
- 3 G. Chen, *Nanoscale energy transport and conversion: a parallel treatment of electrons, molecules, phonons, and photons* (Oxford University Press, 2005).
- 4 M. Flik, B. Choi, and K. Goodson, "Heat transfer regimes in microstructures," (1992).
- 5 H. Song, J. Liu, B. Liu, J. Wu, H.-M. Cheng, and F. Kang, "Two-dimensional materials for thermal management applications," *Joule*, **2**, 442 (2018).
- 6 A. Danowitz, K. Kelley, J. Mao, J. P. Stevenson, and M. Horowitz, "CPU DB: recording microprocessor history," *Queue*, **10**, 10 (2012).
- 7 R. R. Schaller, "Moore's law: past, present and future," *IEEE spectrum*, **34**, 52 (1997).
- 8 M. M. Waldrop, "The chips are down for Moore's law," *Nature News*, **530**, 144 (2016).
- 9 P. K. Schelling, L. Shi, and K. E. Goodson, "Managing heat for electronics," *Mater. Today*, **8**, 30 (2005).
- 10 J. Norley, A. Reynolds, G. Shives, and M. Smalc, "in *P-73: The Development of Natural Graphite-Based Heat Spreaders for Reducing Temperature and Increasing Temperature Uniformity in Flat Panel Displays*, 2005 (Wiley Online Library), p. 562.
- 11 G. Simmons, "Anisotropic thermal conductivity," *J. Geophys. Res. Solid Earth*, **66**, 2269 (1961).
- 12 G. A. Slack, "Anisotropic thermal conductivity of pyrolytic graphite," *Phys. Rev.*, **127**, 694 (1962).
- 13 J. Graebner, S. Jin, G. Kammlott, J. Herb, and C. Gardinier, "Large anisotropic thermal conductivity in synthetic diamond films," *Nature*, **359**, 401 (1992).
- 14 L. Wang, Z. Tamainot-Telto, S. Metcalf, R. Critoph, and R. Wang, "Anisotropic thermal conductivity and permeability of compacted expanded natural graphite," *Appl. Therm. Eng.*, **30**, 1805 (2010).

- 15 J. Luo, W. Lu, Z. Hang, H. Chen, B. Hou, Y. Lai, and C. T. Chan, "Arbitrary control of electromagnetic flux in inhomogeneous anisotropic media with near-zero index," *Phys. Rev. Lett.*, **112**, 073903 (2014).
- 16 G. Zhang and Y.-W. Zhang, "Thermal properties of two-dimensional materials," *Chinese Phys. B*, **26**, 034401 (2017).
- 17 A. Pakdel, C. Zhi, Y. Bando, and D. Golberg, "Low-dimensional boron nitride nanomaterials," *Mater. Today*, **15**, 256 (2012).
- 18 X. Xu, L. F. Pereira, Y. Wang, J. Wu, K. Zhang, X. Zhao, S. Bae, C. T. Bui, R. Xie, and J. T. Thong, "Length-dependent thermal conductivity in suspended single-layer graphene," *Nat. Commun.*, **5**, 1 (2014).
- 19 H. Im and J. Kim, "Thermal conductivity of a graphene oxide–carbon nanotube hybrid/epoxy composite," *Carbon*, **50**, 5429 (2012).
- 20 A. A. Balandin, S. Ghosh, W. Bao, I. Calizo, D. Teweldebrhan, F. Miao, and C. N. Lau, "Superior thermal conductivity of single-layer graphene," *Nano Lett.*, **8**, 902 (2008).
- 21 " (!!! INVALID CITATION !!!).
- 22 J. Cole, A. Brocklin, and C. Stryker," (Google Patents, 2002).
- 23 V. Tiwari, D. Singh, S. Rajgopal, G. Mehta, R. Patel, and F. Baez," in *Reducing power in high-performance microprocessors*, 1998, p. 732.
- 24 C.-L. Su, C.-Y. Tsui, and A. M. Despain," in *Low power architecture design and compilation techniques for high-performance processors*, 1994 (IEEE), p. 489.
- 25 K. Basu, A. Choudhary, J. Pisharath, and M. Kandemir," in *Power protocol: reducing power dissipation on off-chip data buses*, 2002 (IEEE), p. 345.
- 26 S. Olszewski, "Quantum Aspects of the Joule-Lenz Law," *J. Mod. Phys.*, **7**, 162 (2016).
- 27 A. Prokhorov," (Moscow: The Soviet State, 1972).
- 28 A. I. Rae and J. Napolitano," in *Quantum Mechanics* (CRC Press, 2015), p. 200.
- 29 D. J. Griffiths and D. F. Schroeter, *Introduction to quantum mechanics* (Cambridge University Press, 2018).
- 30 S. Wolf, D. Awschalom, R. Buhrman, J. Daughton, v. S. von Molnár, M. Roukes, A. Y. Chtchelkanova, and D. Treger, "Spintronics: a spin-based electronics vision for the future," *science*, **294**, 1488 (2001).

- 31 S. Zhang and Z. Yang, "Intrinsic spin and orbital angular momentum Hall effect," *Phys. Rev. Lett.*, **94**, 066602 (2005).
- 32 M. D. Stiles and A. Zangwill, "Anatomy of spin-transfer torque," *Phys. Rev. B*, **66**, 014407 (2002).
- 33 C.-F. Pai, L. Liu, Y. Li, H. Tseng, D. Ralph, and R. Buhrman, "Spin transfer torque devices utilizing the giant spin Hall effect of tungsten," *Appl. Phys. Lett.*, **101**, 122404 (2012).
- 34 A. Mellnik, J. Lee, A. Richardella, J. Grab, P. Mintun, M. H. Fischer, A. Vaezi, A. Manchon, E.-A. Kim, and N. Samarth, "Spin-transfer torque generated by a topological insulator," *Nature*, **511**, 449 (2014).
- 35 D. C. Ralph and M. D. Stiles, "Spin transfer torques," *J. Magn. Magn. Mater.*, **320**, 1190 (2008).
- 36 R. P. Feynman, "There's plenty of room at the bottom," *California Institute of Technology, Engineering and Science magazine* (1960).
- 37 H. G. Kilian and M. Pietralla, "Anisotropy of thermal diffusivity of uniaxial stretched polyethylenes," *Polymer*, **19**, 664 (1978).
- 38 A. France-Lanord, S. Merabia, T. Albaret, D. Lacroix, and K. Termentzidis, "Thermal properties of amorphous/crystalline silicon superlattices," *J. Phys. Condens. Matter*, **26**, 355801 (2014).
- 39 W. Zhang, Q. Wang, Y. Chen, Z. Wang, and A. T. Wee, "Van der Waals stacked 2D layered materials for optoelectronics," *2D Mater.*, **3**, 022001 (2016).
- 40 X. Liu, Q. Guo, and J. Qiu, "Emerging Low-Dimensional Materials for Nonlinear Optics and Ultrafast Photonics," *Adv. Mater.*, **29**, 1605886 (2017).
- 41 H. Alam and S. Ramakrishna, "A review on the enhancement of figure of merit from bulk to nano-thermoelectric materials," *Nano Energy*, **2**, 190 (2013).
- 42 Fitriani, R. Ovik, B. D. Long, M. C. Barma, M. Riaz, M. F. M. Sabri, S. M. Said, and R. Saidur, "A review on nanostructures of high-temperature thermoelectric materials for waste heat recovery," *Renew. Sust. Energ. Rev.*, **64**, 635 (2016).
- 43 M. S. Dresselhaus, G. Dresselhaus, X. Sun, Z. Zhang, S. B. Cronin, and T. Koga, "Low-dimensional thermoelectric materials," *Phys. Solid State*, **41**, 679 (1999).

- 44 J. Heo, K.-E. Byun, J. Lee, H.-J. Chung, S. Jeon, S. Park, and S. Hwang, "Graphene and Thin-Film Semiconductor Heterojunction Transistors Integrated on Wafer Scale for Low-Power Electronics," *Nano Lett.*, **13**, 5967 (2013).
- 45 M. T. Sharbati, Y. Du, J. Torres, N. D. Ardolino, M. Yun, and F. Xiong, "Low-Power, Electrochemically Tunable Graphene Synapses for Neuromorphic Computing," *Adv. Mater.*, **30**, 1802353 (2018).
- 46 T. Palacios, A. Hsu, and H. Wang, "Applications of graphene devices in RF communications," *IEEE Commun. Mag.*, **48**, 122 (2010).
- 47 P. K. Baheti and H. Garudadri, "in *An Ultra Low Power Pulse Oximeter Sensor Based on Compressed Sensing*, 2009, p. 144.
- 48 F. Wang, S. Liu, L. Shu, and X.-M. Tao, "Low-dimensional carbon based sensors and sensing network for wearable health and environmental monitoring," *Carbon*, **121**, 353 (2017).
- 49 E. W. Hill, A. Vijayaraghavan, and K. Novoselov, "Graphene Sensors," *IEEE Sens. J.*, **11**, 3161 (2011).
- 50 Y. Huang, J. Guo, Y. Kang, Y. Ai, and C. M. Li, "Two dimensional atomically thin MoS<sub>2</sub> nanosheets and their sensing applications," *Nanoscale*, **7**, 19358 (2015).
- 51 P. Ajayan, P. Kim, and K. Banerjee, "Two-dimensional van der Waals materials," *Phys. Today*, **69**, 38 (2016).
- 52 A. K. Geim and I. V. Grigorieva, "Van der Waals heterostructures," *Nature*, **499**, 419 (2013).
- 53 L. Chao, Z. Peng, and Z. David Wei, "Devices and applications of van der Waals heterostructures," *JoS*, **38**, 031005 (2017).
- 54 K. Kim, M. Yankowitz, B. Fallahzad, S. Kang, H. C. Movva, S. Huang, S. Larentis, C. M. Corbet, T. Taniguchi, and K. Watanabe, "Van der Waals heterostructures with high accuracy rotational alignment," *Nano Lett.*, **16**, 1989 (2016).
- 55 N. Yang, X. Xu, G. Zhang, and B. Li, "Thermal transport in nanostructures," *AIP Adv.*, **2**, 041410 (2012).
- 56 B. Liu, F. Meng, C. D. Reddy, J. A. Baimova, N. Srikanth, S. V. Dmitriev, and K. Zhou, "Thermal transport in a graphene–MoS<sub>2</sub> bilayer heterostructure: a molecular dynamics study," *RSC Adv.*, **5**, 29193 (2015).

- 57 J. Wan, S. D. Lacey, J. Dai, W. Bao, M. S. Fuhrer, and L. Hu, "Tuning two-dimensional nanomaterials by intercalation: materials, properties and applications," *Chem. Soc. Rev.*, **45**, 6742 (2016).
- 58 P. Chakraborty, Y. Liu, T. Ma, X. Guo, L. Cao, R. Hu, and Y. Wang, "Quenching Thermal Transport in Aperiodic Superlattices: A Molecular Dynamics and Machine Learning Study," *ACS Appl. Mater. Interfaces*, **12**, 8795 (2020).
- 59 I. O. Thomas and G. P. Srivastava, "Control of thermal conductivity with species mass in transition-metal dichalcogenides," *J. Appl. Phys.*, **123**, 135703 (2018).
- 60 C. Sevik, A. Kinaci, J. B. Haskins, and T. Çağın, "Influence of disorder on thermal transport properties of boron nitride nanostructures," *Phys. Rev. B*, **86**, 075403 (2012).
- 61 Y. Yang, C.-C. Chen, M. C. Scott, C. Ophus, R. Xu, A. Pryor, L. Wu, F. Sun, W. Theis, J. Zhou, M. Eisenbach, P. R. C. Kent, R. F. Sabirianov, H. Zeng, P. Ercius, and J. Miao, "Deciphering chemical order/disorder and material properties at the single-atom level," *Nature*, **542**, 75 (2017).
- 62 Z. Xu, "Heat transport in low-dimensional materials: A review and perspective," *Theor. App. Mech. Lett.*, **6**, 113 (2016).
- 63 X. Qian, X. Gu, M. S. Dresselhaus, and R. Yang, "Anisotropic Tuning of Graphite Thermal Conductivity by Lithium Intercalation," *J. Phys. Chem. Lett.*, **7**, 4744 (2016).
- 64 R. Mao, Y. Chen, and K. W. Kim, "Atomistic modeling of phonon transport in turbostratic graphitic structures," *J. Appl. Phys.*, **119**, 204305 (2016).
- 65 C. L. Choy and K. Young, "Thermal conductivity of semicrystalline polymers — a model," *Polymer*, **18**, 769 (1977).
- 66 V. Dhand, G. Mittal, K. Y. Rhee, S.-J. Park, and D. Hui, "A short review on basalt fiber reinforced polymer composites," *Compos. B. Eng.*, **73**, 166 (2015).
- 67 D. Mecerreyes, R. Marcilla, E. Ochoteco, H. Grande, J. A. Pomposo, R. Vergaz, and J. M. Sánchez Pena, "A simplified all-polymer flexible electrochromic device," *Electrochim. Acta*, **49**, 3555 (2004).
- 68 G. Shuxiang and K. Asaka, " in *Polymer-based new type of micropump for bio-medical application*, 2003, p. 1830.
- 69 F. Bischoff, "Organic Polymer Biocompatibility and Toxicology," *Clin. Chem.*, **18**, 869 (1972).

- 70 L. Y. Qiu and Y. H. Bae, "Polymer Architecture and Drug Delivery," *Pharm. Res.*, **23**, 1 (2006).
- 71 C. E. Mora-Huertas, H. Fessi, and A. Elaissari, "Polymer-based nanocapsules for drug delivery," *Int. J. Pharm.*, **385**, 113 (2010).
- 72 A. K. Patri, I. J. Majoros, and J. R. Baker, "Dendritic polymer macromolecular carriers for drug delivery," *Curr. Opin. Chem. Biol.*, **6**, 466 (2002).
- 73 J. Hu, H. Meng, G. Li, and S. I. Ibekwe, "A review of stimuli-responsive polymers for smart textile applications," *Smart Mater. Struct.*, **21**, 053001 (2012).
- 74 J. Hu and S. Chen, "A review of actively moving polymers in textile applications," *J. Mater. Chem.*, **20**, 3346 (2010).
- 75 T. Zhang, X. Wu, and T. Luo, "Polymer Nanofibers with Outstanding Thermal Conductivity and Thermal Stability: Fundamental Linkage between Molecular Characteristics and Macroscopic Thermal Properties," *J. Phys. Chem. C*, **118**, 21148 (2014).
- 76 J. Liu and R. Yang, "Length-dependent thermal conductivity of single extended polymer chains," *Phys. Rev. B*, **86**, 104307 (2012).
- 77 A. Henry and G. Chen, "High Thermal Conductivity of Single Polyethylene Chains Using Molecular Dynamics Simulations," *Phys. Rev. Lett.*, **101**, 235502 (2008).
- 78 J. J. Freeman, G. J. Morgan, and C. A. Cullen, "Thermal conductivity of a single polymer chain," *Phys. Rev. B*, **35**, 7627 (1987).
- 79 S. Shen, A. Henry, J. Tong, R. Zheng, and G. Chen, "Polyethylene nanofibres with very high thermal conductivities," *Nat. Nanotechnol.*, **5**, 251 (2010).
- 80 X. Wang, V. Ho, R. A. Segalman, and D. G. Cahill, "Thermal Conductivity of High-Modulus Polymer Fibers," *Macromolecules*, **46**, 4937 (2013).
- 81 Y. Lu, J. Liu, X. Xie, and D. G. Cahill, "Thermal Conductivity in the Radial Direction of Deformed Polymer Fibers," *ACS Macro Lett.*, **5**, 646 (2016).
- 82 J. He, K. Kim, Y. Wang, and J. Liu, "Strain effects on the anisotropic thermal transport in crystalline polyethylene," *Appl. Phys. Lett.*, **112**, 051907 (2018).
- 83 V. K. Joshi, "Spintronics: A contemporary review of emerging electronics devices," *Int. J. Eng. Sci. Technol.*, **19**, 1503 (2016).

- 84 S. A. Wolf, A. Y. Chtchelkanova, and D. M. Treger, "Spintronics—A retrospective and perspective," *IBM J Res Dev.*, **50**, 101 (2006).
- 85 J. F. Gregg, R. P. Borges, E. Jouguelet, C. L. Dennis, I. Petej, S. M. Thompson, and K. Ounadjela, "Spin injection efficiency in spin electronic devices," *J. Magn. Magn. Mater.*, **265**, 274 (2003).
- 86 S. Bhatti, R. Sbiaa, A. Hirohata, H. Ohno, S. Fukami, and S. N. Piramanayagam, "Spintronics based random access memory: a review," *Mater. Today*, **20**, 530 (2017).
- 87 H. Jaffrès and A. Fert, "Spin injection from a ferromagnetic metal into a semiconductor," *J. Appl. Phys.*, **91**, 8111 (2002).
- 88 T. Sarkar, A. K. Raychaudhuri, A. K. Bera, and S. M. Yusuf, "Effect of size reduction on the ferromagnetism of the manganite  $\text{La}_{1-x}\text{Ca}_x\text{MnO}_3$  ( $x=0.33$ )," *New J. Phys.*, **12**, 123026 (2010).
- 89 X. He, W. Zhong, C.-T. Au, and Y. Du, "Size dependence of the magnetic properties of Ni nanoparticles prepared by thermal decomposition method," *Nanoscale Res. Lett.*, **8**, 446 (2013).
- 90 W. J. M. Naber, S. Faez, and W. G. v. d. Wiel, "Organic spintronics," *J. Phys. D*, **40**, R205 (2007).
- 91 W. Ma, L. Xu, A. F. de Moura, X. Wu, H. Kuang, C. Xu, and N. A. Kotov, "Chiral Inorganic Nanostructures," *Chem. Rev.*, **117**, 8041 (2017).
- 92 J. Ahn, E. Lee, J. Tan, W. Yang, B. Kim, and J. Moon, "A new class of chiral semiconductors: chiral-organic-molecule-incorporating organic–inorganic hybrid perovskites," *Mater. Horiz.*, **4**, 851 (2017).
- 93 R. Naaman and D. H. Waldeck, "Chiral-Induced Spin Selectivity Effect," *J. Phys. Chem. Lett.*, **3**, 2178 (2012).
- 94 Z. Liang, W. Evans, and P. Keblinski, "Equilibrium and nonequilibrium molecular dynamics simulations of thermal conductance at solid-gas interfaces," *Phys. Rev. E*, **87**, 022119 (2013).
- 95 N. A. Kumar, M. A. Dar, R. Gul, and J.-B. Baek, "Graphene and molybdenum disulfide hybrids: synthesis and applications," *Mater. Today*, **18**, 286 (2015).

- 96 J.-U. Lee, D. Yoon, H. Kim, S. W. Lee, and H. Cheong, "Thermal conductivity of suspended pristine graphene measured by Raman spectroscopy," *Phys. Rev. B*, **83**, 081419 (2011).
- 97 J. H. Seol, I. Jo, A. L. Moore, L. Lindsay, Z. H. Aitken, M. T. Pettes, X. Li, Z. Yao, R. Huang, and D. Broido, "Two-dimensional phonon transport in supported graphene," *Science*, **328**, 213 (2010).
- 98 X. Tian, M. E. Itkis, E. B. Bekyarova, and R. C. Haddon, "Anisotropic thermal and electrical properties of thin thermal interface layers of graphite nanoplatelet-based composites," *Sci. Rep.*, **3**, 1710 (2013).
- 99 X. Xu, L. F. Pereira, Y. Wang, J. Wu, K. Zhang, X. Zhao, S. Bae, C. T. Bui, R. Xie, and J. T. Thong, "Length-dependent thermal conductivity in suspended single-layer graphene," *Nat. Commun.*, **5** (2014).
- 100 J. Zhang, Y. Hong, X. Wang, Y. Yue, D. Xie, J. Jiang, and Y. Xiong, "Phonon Thermal Properties of Transition-Metal Dichalcogenides MoS<sub>2</sub> and MoSe<sub>2</sub> Heterostructure," *J. Phys. Chem. C* (2017).
- 101 A. Majumdar, "SCANNING THERMAL MICROSCOPY," *Annu. Rev. Mater. Sci.*, **29**, 505 (1999).
- 102 C. Canetta and A. Narayanaswamy, "Sub-picowatt resolution calorimetry with a bi-material microcantilever sensor," *Appl. Phys. Lett.*, **102**, 103112 (2013).
- 103 S. Alaie, D. F. Goettler, K. Abbas, M. F. Su, C. M. Reinke, I. El-Kady, and Z. C. Leseman, "Microfabricated suspended island platform for the measurement of in-plane thermal conductivity of thin films and nanostructured materials with consideration of contact resistance," *Rev. Sci. Instrum.*, **84**, 105003 (2013).
- 104 Z. Wang, S. S. Adhikari, M. Kroener, D. Kojda, R. Mitdank, S. F. Fischer, W. Toellner, K. Nielsch, and P. Woias, " in *Electrical conductivity and Seebeck coefficient measurements of single nanowires by utilizing a microfabricated thermoelectric nanowire characterization platform*, 2013, p. 508.
- 105 A. Bar-Cohen, P. Wang, and E. Rahim, "Thermal management of high heat flux nanoelectronic chips," *Microgravity Sci Technol.*, **19**, 48 (2007).
- 106 X. Feng, X. Huang, and X. Wang, "Thermal conductivity and secondary porosity of single anatase TiO<sub>2</sub> nanowire," *Nanotechnology*, **23**, 185701 (2012).

- 107 J. Guo, X. Wang, and T. Wang, "Thermal characterization of microscale conductive and nonconductive wires using transient electrothermal technique," *J. Appl. Phys.*, **101**, 063537 (2007).
- 108 D. G. Cahill, "Thermal conductivity measurement from 30 to 750 K: the  $3\omega$  method," *Rev. Sci. Instrum.*, **61**, 802 (1990).
- 109 W. Liang, O. Rabin, A. I. Hochbaum, M. Fardy, M. Zhang, and P. Yang, "Thermoelectric properties of p-type PbSe nanowires," *Nano Res.*, **2**, 394 (2009).
- 110 A. I. Hochbaum, R. Chen, R. D. Delgado, W. Liang, E. C. Garnett, M. Najarian, A. Majumdar, and P. Yang, "Enhanced thermoelectric performance of rough silicon nanowires," *Nature*, **451**, 163 (2008).
- 111 M. Fardy, A. I. Hochbaum, J. Goldberger, M. M. Zhang, and P. Yang, "Synthesis and Thermoelectrical Characterization of Lead Chalcogenide Nanowires," *Adv. Mater.*, **19**, 3047 (2007).
- 112 A. Schmidt, M. Chiesa, X. Chen, and G. Chen, "An optical pump-probe technique for measuring the thermal conductivity of liquids," *Rev. Sci. Instrum.*, **79**, 064902 (2008).
- 113 D. Zhao, X. Qian, X. Gu, S. A. Jajja, and R. Yang, "Measurement Techniques for Thermal Conductivity and Interfacial Thermal Conductance of Bulk and Thin Film Materials," *J. Electron. Packag.*, **138**, 040802 (2016).
- 114 M. Timofeeva, A. Bolshakov, P. D. Tovee, D. A. Zeze, V. G. Dubrovskii, and O. V. Kolosov, "Scanning thermal microscopy with heat conductive nanowire probes," *Ultramicroscopy*, **162**, 42 (2016).
- 115 X. F. Liu, R. Wang, Y. P. Jiang, Q. Zhang, X. Y. Shan, and X. H. Qiu, "Thermal conductivity measurement of individual CdS nanowires using microphotoluminescence spectroscopy," *J. Appl. Phys.*, **108**, 054310 (2010).
- 116 H. Malekpour and A. A. Balandin, "Raman-based technique for measuring thermal conductivity of graphene and related materials," *J. Raman Spectrosc.*, **49**, 106 (2018).
- 117 M. Paillet, R. Parret, J.-L. Sauvajol, and P. Colomban, "Graphene and related 2D materials: An overview of the Raman studies," *J. Raman Spectrosc.*, **49**, 8 (2018).
- 118 P. Jiang, X. Qian, and R. Yang, "Tutorial: Time-domain thermoreflectance (TDTR) for thermal property characterization of bulk and thin film materials," *J. Appl. Phys.*, **124**, 161103 (2018).

- 119 G.-M. Choi and D. G. Cahill, "Kerr rotation in Cu, Ag, and Au driven by spin accumulation and spin-orbit coupling," *Phys. Rev. B*, **90**, 214432 (2014).
- 120 E. Kojima, R. Shimano, Y. Hashimoto, S. Katsumoto, Y. Iye, and M. Kuwata-Gonokami, "Observation of the spin-charge thermal isolation of ferromagnetic  $\text{{\rm{Ga}}}_{0.94}\text{{\rm{Mn}}}_{0.06}\text{{\rm{As}}}$  by time-resolved magneto-optical measurements," *Phys. Rev. B*, **68**, 193203 (2003).
- 121 G. P. Zhang, W. Hübner, G. Lefkidis, Y. Bai, and T. F. George, "Paradigm of the time-resolved magneto-optical Kerr effect for femtosecond magnetism," *Nat. Phys.*, **5**, 499 (2009).
- 122 G. Kresse and J. Hafner, "Ab initio molecular dynamics for liquid metals," *Phys. Rev. B*, **47**, 558 (1993).
- 123 D. C. Rapaport and D. C. R. Rapaport, *The art of molecular dynamics simulation* (Cambridge university press, 2004).
- 124 C. Van den Broeck and M. Esposito, "Ensemble and trajectory thermodynamics: A brief introduction," *Physica A*, **418**, 6 (2015).
- 125 J. Tersoff, "Empirical interatomic potential for silicon with improved elastic properties," *Phys. Rev. B*, **38**, 9902 (1988).
- 126 J. E. Jones and S. Chapman, "On the determination of molecular fields. &#x2014;II. From the equation of state of a gas," *Proc. R. Soc. A*, **106**, 463 (1924).
- 127 F. Müller-Plathe, "A simple nonequilibrium molecular dynamics method for calculating the thermal conductivity," *J. Chem. Phys.*, **106**, 6082 (1997).
- 128 J. Shiomi, "Nonequilibrium molecular dynamics methods for lattice heat conduction calculations," *Ann. Rev. Heat Transfer*, **17** (2014).
- 129 C. A. Paddock and G. L. Eesley, "Transient thermoreflectance from thin metal films," *J. Appl. Phys.*, **60**, 285 (1986).
- 130 A. J. Schmidt, X. Chen, and G. Chen, "Pulse accumulation, radial heat conduction, and anisotropic thermal conductivity in pump-probe transient thermoreflectance," *Rev. Sci. Instrum.*, **79**, 114902 (2008).
- 131 S. Yamamoto and I. Matsuda, "Measurement of the Resonant Magneto-Optical Kerr Effect Using a Free Electron Laser," *Appl. Sci.*, **7**, 662 (2017).

- 132 L. Zhong, R. C. Bruno, K. Ethan, L. Ruitao, R. Rahul, T. Humberto, A. P. Marcos, and T. Mauricio, "Defect engineering of two-dimensional transition metal dichalcogenides," *2D Mater.*, **3**, 022002 (2016).
- 133 J.-C. Zheng, L. Zhang, A. V. Kretinin, S. V. Morozov, Y. B. Wang, T. Wang, X. Li, F. Ren, J. Zhang, and C.-Y. Lu, "High thermal conductivity of hexagonal boron nitride laminates," *2D Mater.*, **3**, 011004 (2016).
- 134 F. Withers, O. Del Pozo-Zamudio, A. Mishchenko, A. P. Rooney, A. Gholinia, K. Watanabe, T. Taniguchi, S. J. Haigh, A. K. Geim, A. I. Tartakovskii, and K. S. Novoselov, "Light-emitting diodes by band-structure engineering in van der Waals heterostructures," *Nat Mater.*, **14**, 301 (2015).
- 135 D. Jariwala, T. J. Marks, and M. C. Hersam, "Mixed-dimensional van der Waals heterostructures," *Nat Mater.*, **16**, 170 (2017).
- 136 X. Li and H. Zhu, "Two-dimensional MoS<sub>2</sub>: Properties, preparation, and applications," *J Materiomics*, **1**, 33 (2015).
- 137 K. S. Novoselov, A. K. Geim, S. V. Morozov, D. Jiang, Y. Zhang, S. V. Dubonos, I. V. Grigorieva, and A. A. Firsov, "Electric field effect in atomically thin carbon films," *Science*, **306**, 666 (2004).
- 138 A. Pant, Z. Mutlu, D. Wickramaratne, H. Cai, R. K. Lake, C. Ozkan, and S. Tongay, "Fundamentals of lateral and vertical heterojunctions of atomically thin materials," *Nanoscale*, **8**, 3870 (2016).
- 139 A. C. Ferrari, F. Bonaccorso, V. Fal'Ko, K. S. Novoselov, S. Roche, P. Bøggild, S. Borini, F. H. Koppens, V. Palermo, and N. Pugno, "Science and technology roadmap for graphene, related two-dimensional crystals, and hybrid systems," *Nanoscale*, **7**, 4598 (2015).
- 140 E. Pop, V. Varshney, and A. K. Roy, "Thermal properties of graphene: Fundamentals and applications," *MRS Bull.*, **37**, 1273 (2012).
- 141 H. Mizuno, S. Mossa, and J.-L. Barrat, "Beating the amorphous limit in thermal conductivity by superlattices design," *Sci. Rep.*, **5**, 14116 (2015).
- 142 R. Venkatasubramanian, E. Siivola, T. Colpitts, and B. O'quinn, "Thin-film thermoelectric devices with high room-temperature figures of merit," *Nature*, **413**, 597 (2001).

- 143 J. S. Kang, M. Ke, and Y. Hu, "Ionic Intercalation in Two-Dimensional van der Waals Materials: In Situ Characterization and Electrochemical Control of the Anisotropic Thermal Conductivity of Black Phosphorus," *Nano Lett.*, **17**, 1431 (2017).
- 144 F. Xiong, H. Wang, X. Liu, J. Sun, M. Brongersma, E. Pop, and Y. Cui, "Li intercalation in MoS<sub>2</sub>: in situ observation of its dynamics and tuning optical and electrical properties," *Nano Lett.*, **15**, 6777 (2015).
- 145 G. Zhu, J. Liu, Q. Zheng, R. Zhang, D. Li, D. Banerjee, and D. G. Cahill, "Tuning thermal conductivity in molybdenum disulfide by electrochemical intercalation," *Nat. Commun.*, **7**, 13211 (2016).
- 146 Y.-H. Choi, D.-H. Lim, J.-H. Jeong, D. Park, K.-S. Jeong, M. Kim, A. Song, H.-S. Chung, K.-B. Chung, Y. Yi, and M.-H. Cho, "Characterization of Rotational Stacking Layers in Large-Area MoSe<sub>2</sub> Film Grown by Molecular Beam Epitaxy and Interaction with Photon," *ACS Appl. Mater. Interfaces*, **9**, 30786 (2017).
- 147 C. Dean, L. Wang, P. Maher, C. Forsythe, F. Ghahari, Y. Gao, J. Katoch, M. Ishigami, P. Moon, and M. Koshino, "Hofstadter's butterfly and the fractal quantum Hall effect in moiré superlattices," *Nature*, **497**, 598 (2013).
- 148 M. Flores, E. Cisternas, J. Correa, and P. Vargas, "Moiré patterns on STM images of graphite induced by rotations of surface and subsurface layers," *Chem. Phys.*, **423**, 49 (2013).
- 149 J. Jasinski, S. Dumpala, G. Sumanasekera, M. Sunkara, and P. Ouseph, "Observation and interpretation of adjacent Moiré patterns of different shapes in bilayer graphene," *Appl. Phys. Lett.*, **99**, 073104 (2011).
- 150 M. Pimenta, G. Dresselhaus, M. S. Dresselhaus, L. Cancado, A. Jorio, and R. Saito, "Studying disorder in graphite-based systems by Raman spectroscopy," *Phys. Chem. Chem. Phys.*, **9**, 1276 (2007).
- 151 L. Liu, J. Park, D. A. Siegel, K. F. McCarty, K. W. Clark, W. Deng, L. Basile, J. C. Idrobo, A.-P. Li, and G. Gu, "Heteroepitaxial growth of two-dimensional hexagonal boron nitride templated by graphene edges," *Science*, **343**, 163 (2014).
- 152 Q. Li, M. Liu, Y. Zhang, and Z. Liu, "Hexagonal Boron Nitride–Graphene Heterostructures: Synthesis and Interfacial Properties," *Small*, **12**, 32 (2016).

- 153 Z. Ding, Q.-X. Pei, J.-W. Jiang, W. Huang, and Y.-W. Zhang, "Interfacial thermal conductance in graphene/MoS<sub>2</sub> heterostructures," *Carbon*, **96**, 888 (2016).
- 154 W. Wei, Y. Dai, and B. Huang, "Straintronics in two-dimensional in-plane heterostructures of transition-metal dichalcogenides," *Phys. Chem. Chem. Phys.*, **19**, 663 (2017).
- 155 Z. Zhang, S. Hu, J. Chen, and B. Li, "Hexagonal boron nitride: a promising substrate for graphene with high heat dissipation," *Nanotechnology*, **28**, 225704 (2017).
- 156 C. Zhesheng, B. Johan, and S. Abhay, "Optimal light harvesting in 2D semiconductor heterostructures," *2D Mater.*, **4**, 025115 (2017).
- 157 Y. Gong, J. Lin, X. Wang, G. Shi, S. Lei, Z. Lin, X. Zou, G. Ye, R. Vajtai, and B. I. Yakobson, "Vertical and in-plane heterostructures from WS<sub>2</sub>/MoS<sub>2</sub> monolayers," *Nat. Mater.*, **13**, 1135 (2014).
- 158 V. NanoLab, " " *QuantumWise A/S* ([www.quantumwise.com](http://www.quantumwise.com)).
- 159 P. Trucano and R. Chen, "Structure of graphite by neutron diffraction," *Nature*, **258**, 136 (1975).
- 160 J. M. Campanera, G. Savini, I. Suarez-Martinez, and M. I. Heggie, "Density functional calculations on the intricacies of Moiré patterns on graphite," *Phys. Rev. B*, **75**, 235449 (2007).
- 161 S. Plimpton, "Fast parallel algorithms for short-range molecular dynamics," *J. Comput. Phys.*, **117**, 1 (1995).
- 162 L. Lindsay and D. A. Broido, "Optimized Tersoff and Brenner empirical potential parameters for lattice dynamics and phonon thermal transport in carbon nanotubes and graphene," *Phys. Rev. B*, **81**, 205441 (2010).
- 163 Z. Wei, J. Yang, W. Chen, K. Bi, D. Li, and Y. Chen, "Phonon mean free path of graphite along the c-axis," *Appl. Phys. Lett.*, **104**, 081903 (2014).
- 164 W. Humphrey, A. Dalke, and K. Schulten, "VMD: visual molecular dynamics," *J Mol Graph*, **14**, 33 (1996).
- 165 L. Li and G. E. Caldwell, "Coefficient of cross correlation and the time domain correspondence," *J Electromyogr Kinesiol*, **9**, 385 (1999).
- 166 Z. Wang and X. Ruan, "On the domain size effect of thermal conductivities from equilibrium and nonequilibrium molecular dynamics simulations," *J. Appl. Phys.*, **121**, 044301 (2017).

- 167 Z. Wang, S. Safarkhani, G. Lin, and X. Ruan, "Uncertainty quantification of thermal conductivities from equilibrium molecular dynamics simulations," *Int. J. Heat Mass Transfer*, **112**, 267 (2017).
- 168 J. P. Feser and D. G. Cahill, "Probing anisotropic heat transport using time-domain thermoreflectance with offset laser spots," *Rev. Sci. Instrum.*, **83**, 104901 (2012).
- 169 L. Lindsay, D. Broido, and N. Mingo, "Flexural phonons and thermal transport in multilayer graphene and graphite," *Phys. Rev. B*, **83**, 235428 (2011).
- 170 Z. Liang, A. Jain, A. J. McGaughey, and P. Keblinski, "Molecular simulations and lattice dynamics determination of Stillinger-Weber GaN thermal conductivity," *J. Appl. Phys.*, **118**, 125104 (2015).
- 171 L. Lindsay, D. Broido, and T. Reinecke, "First-principles determination of ultrahigh thermal conductivity of boron arsenide: a competitor for diamond?," *Phys. Rev. Lett.*, **111**, 025901 (2013).
- 172 T. Zhu and E. Ertekin, "Phonon transport on two-dimensional graphene/boron nitride superlattices," *Phys. Rev. B*, **90**, 195209 (2014).
- 173 P. E. Hopkins, P. M. Norris, M. S. Tsegaye, and A. W. Ghosh, "Extracting phonon thermal conductance across atomic junctions: Nonequilibrium Green's function approach compared to semiclassical methods," *J. Appl. Phys.*, **106**, 063503 (2009).
- 174 J. D. Gale, "GULP: A computer program for the symmetry-adapted simulation of solids," *J. Chem. Soc. Faraday Trans.*, **93**, 629 (1997).
- 175 L. Xiong, X. Chen, N. Zhang, D. McDowell, and Y. Chen, "Prediction of phonon properties of 1D polyatomic systems using concurrent atomistic-continuum simulation," *Arch. Appl. Mech.*, **84** (2014).
- 176 J. Turney, E. Landry, A. McGaughey, and C. Amon, "Predicting phonon properties and thermal conductivity from anharmonic lattice dynamics calculations and molecular dynamics simulations," *Phys. Rev. B*, **79**, 064301 (2009).
- 177 A. McGaughey and J. M. Larkin, "Predicting phonon properties from equilibrium molecular dynamics simulations," *Ann. Rev. Heat Transfer*, **17**, 49 (2014).
- 178 W. Li, J. Carrete, N. A. Katcho, and N. Mingo, "ShengBTE: A solver of the Boltzmann transport equation for phonons," *Comput. Phys. Commun*, **185**, 1747 (2014).

- 179 Y. Wang, C. Gu, and X. Ruan, "Optimization of the random multilayer structure to break the random-alloy limit of thermal conductivity," *Appl. Phys. Lett.*, **106**, 073104 (2015).
- 180 C. A. Polanco, R. Rastgarkafshgarkolaei, J. Zhang, N. Q. Le, P. M. Norris, and A. W. Ghosh, "Design rules for interfacial thermal conductance: Building better bridges," *Phys. Rev. B*, **95**, 195303 (2017).
- 181 P. B. Allen and J. L. Feldman, "Thermal conductivity of disordered harmonic solids," *Phys. Rev. B*, **48**, 12581 (1993).
- 182 J. M. Larkin and A. J. H. McGaughey, "Thermal conductivity accumulation in amorphous silica and amorphous silicon," *Phys. Rev. B*, **89**, 144303 (2014).
- 183 K. Kim, J. He, B. Ganeshan, and J. Liu, "Disorder enhanced thermal conductivity anisotropy in two-dimensional materials and van der Waals heterostructures," *J. Appl. Phys.*, **124**, 055104 (2018).
- 184 L. Lindsay, D. A. Broido, and T. L. Reinecke, "Ab initio thermal transport in compound semiconductors," *Phys. Rev. B*, **87**, 165201 (2013).
- 185 R. M. Costescu, M. A. Wall, and D. G. Cahill, "Thermal conductance of epitaxial interfaces," *Phys. Rev. B*, **67**, 054302 (2003).
- 186 R. Wilson and D. G. Cahill, "Anisotropic failure of Fourier theory in time-domain thermoreflectance experiments," *Nat. Commun.*, **5**, 1 (2014).
- 187 P. Jiang, X. Qian, X. Li, and R. Yang, "Three-dimensional anisotropic thermal conductivity tensor of single crystalline  $\beta$ -Ga<sub>2</sub>O<sub>3</sub>," *Appl. Phys. Lett.*, **113**, 232105 (2018).
- 188 C. Prada, D. Clorennec, and D. Royer, "Local vibration of an elastic plate and zero-group velocity Lamb modes," *J. Acoust. Soc. Am.*, **124**, 203 (2008).
- 189 S. Dalum and P. Hedegård, "Theory of Chiral Induced Spin Selectivity," *Nano Lett.*, **19**, 5253 (2019).
- 190 R. L. Milot, R. J. Sutton, G. E. Eperon, A. A. Haghghirad, J. Martinez Hardigree, L. Miranda, H. J. Snaith, M. B. Johnston, and L. M. Herz, "Charge-Carrier Dynamics in 2D Hybrid Metal–Halide Perovskites," *Nano Lett.*, **16**, 7001 (2016).
- 191 E. Medina, L. A. González-Arraga, D. Finkelstein-Shapiro, B. Berche, and V. Mujica, "Continuum model for chiral induced spin selectivity in helical molecules," *J. Chem. Phys.*, **142**, 194308 (2015).

- 192 J. Kimling, G.-M. Choi, J. T. Brangham, T. Matalla-Wagner, T. Huebner, T. Kuschel, F. Yang, and D. G. Cahill, "Picosecond Spin Seebeck Effect," *Phys. Rev. Lett.*, **118**, 057201 (2017).
- 193 K. Vandaele, S. J. Watzman, B. Flebus, A. Prakash, Y. Zheng, S. R. Boona, and J. P. Heremans, "Thermal spin transport and energy conversion," *Mater. Today Phys.*, **1**, 39 (2017).
- 194 X. Wang, C. D. Liman, N. D. Treat, M. L. Chabinyc, and D. G. Cahill, "Ultralow thermal conductivity of fullerene derivatives," *Phys. Rev. B*, **88**, 075310 (2013).

## **APPENDICES**

In the appendices, I wrote down the additional information for my dissertation. I showed the dispersion curve of the turbostratic graphite. I also showed the group velocity of the pristine graphite and the through-plane mass disorder. Finally, I figured out the frequency-dependent phonon lifetime of the graphite and the through-plane mass disorder using the GULP simulations.

## Appendix A

### 1. Phonon dispersion of the turbostratic graphite

The phonon dispersion of the turbostratic graphite (stacking disorder, SD,  $\Theta = 27.13^\circ$ ) was calculated using the GULP package with the same interatomic potential as in MD simulations. Figure S1a shows the phonon dispersions along the  $\Gamma$ -K direction (corresponds to the ab-plane in the real space) for the turbostratic graphite. The turbostratic graphite has much more branches and resembles a ‘folded’ version of that of the pristine graphite. Figure S1b shows the phonon dispersion along the  $\Gamma$ -A direction (corresponds to the c-axis in the real space). Comparing with the pristine graphite in this direction, the turbostratic graphite has the curves slightly shifted downwards, but similar with that of the pristine graphite.

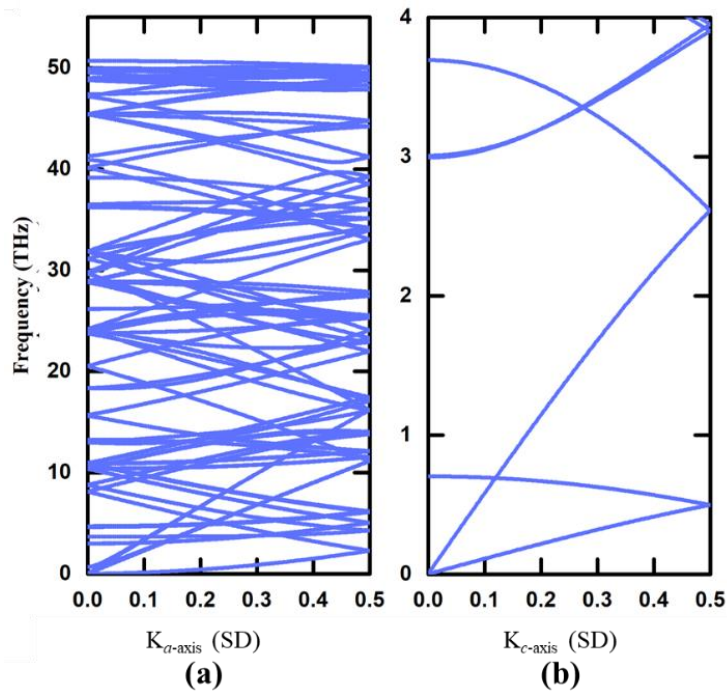


**Figure A.1.** Phonon group velocity of the graphite with the stacking disorder in the (a) ab-plane (b) along the c-axis.

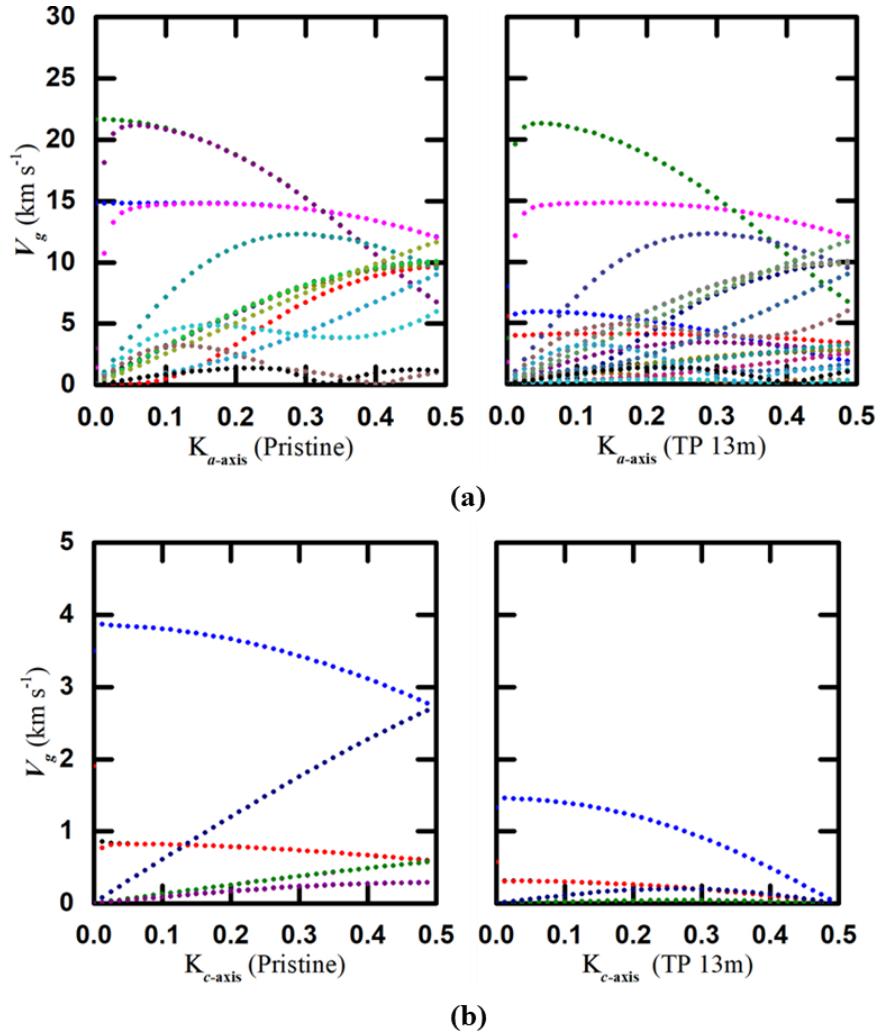


**Figure A.2.** Group velocity of the pristine graphite and the through-plane mass disorder (13m) (a) in the ab-plane (b) along the c-axis.

### A. Group velocity of the pristine graphite and the through-plane mass disorder in the ab-plane along the c-axis

Figure S2 shows the group velocity of all branches that was calculated using the equation,  $v_g = \partial\omega / \partial k$  from the phonon dispersions. Most of the high group velocity in the ab-plane branches remain the same as in pristine graphite, and the additional branches with lower group velocities originates from the layer with heavier mass (Figure S2a). The group velocity of acoustic branches along the c-axis is significantly suppressed (Figure S2b).

## B. Frequency-dependence of phonon lifetime

We calculated the phonon lifetime to further understand the reason for the thermal anisotropy ratio enhancement in graphite-like structures by the normal-mode analysis (NMA).<sup>1,2</sup> We project the trajectory of the atomic position and velocity in dump files on the eigenvectors of normal mode coordinate. The vibrational position trajectory of mode  $(\kappa)$  under the normal mode coordinates,  $q(\kappa; t)$ , is

$$q(\kappa; t) = \sum_{b,t} \left( \frac{m_b}{N} \right)^{1/2} \exp[i\kappa \cdot r_0^l] e_b^*(\kappa) \cdot u_b^l(t) \quad (S1)$$

, where the superscript \* denotes complex conjugate operation,  $\kappa$  and  $\nu$  are the wavevector and polarization of the phonon mode, respectively.  $u_b^l(t)$  is the real-space atomic displacement of the b-th atom in the l-th unit cell at time t,  $r_0$  is the equilibrium position,  $e_b$  is the eigenvector of the normal mode at atom b with mass  $m_b$ , and  $N$  is the total number of atoms in the simulation cell. Its time derivative,  $\dot{q}(\kappa; t)$  is the vibrational velocity trajectory. By using the velocity trajectory, we can obtain the kinetic energy of the normal modes  $(\kappa)$ :<sup>3</sup>

$$T(\kappa; t) = \frac{1}{2} \dot{q}^*(\kappa; t) \dot{q}(\kappa; t) \quad (S2)$$

From lattice dynamic theory, the phonon life time using the autocorrelation function of kinetic energy can be shown that<sup>3</sup>

$$\frac{\langle T(\kappa; t) T(\kappa; 0) \rangle}{\langle T(\kappa; 0) T(\kappa; 0) \rangle} = \cos^2 \left[ \omega_\alpha(\kappa) t \right] \exp \left[ -t / \tau(\kappa) \right] \quad (S3)$$

, where  $\omega_\alpha(\kappa)$  is the anharmonic frequency and  $\tau(\kappa)$  is the phonon life time of normal modes.

Here, the anharmonic frequency can be replace with the harmonic frequency since the harmonic frequency is insignificantly different from the anharmonic frequency,  $\omega_\alpha(\kappa) \cong \omega(\kappa)$ .<sup>4</sup>

The NMA for the pristine graphite and the TPMD in ab-plane is conducted on a rectangular pristine graphite structure (3584 carbon atoms) with the conventional cell numbers  $N_x = 14$ ,  $N_y = 8$ ,  $N_z = 4$  in the x, y, z directions, respectively. Thus, four reduced wavevectors exist along the  $\Gamma$ -K direction, which is from 0.125 to 0.5. The NMA for those along the c-axis is conducted on a rectangular pristine graphite structure (2240 carbon atoms) with the conventional cell numbers  $N_x = 7$ ,  $N_y = 4$ ,  $N_z = 10$  in the x, y, z directions, respectively. Thus, five reduced wavevectors exist along the  $\Gamma$ -A direction, which is from 0.1 to 0.5. Figure S3 shows the frequency-dependent phonon lifetime comparison between the pristine graphite and the TPMD with  $M_H=13m$  in the ab plane (Figure S3a) and those along the c-axis (Figure S3b).

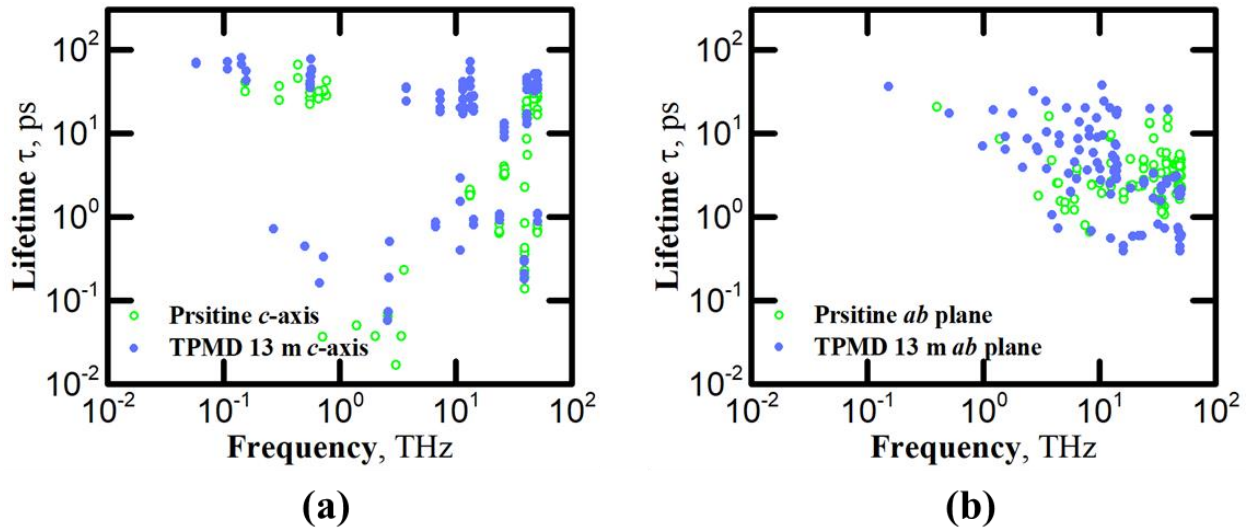


**Figure A.3.** Frequency-dependent phonon lifetime of the pristine graphite and the through-plane mass disorder (a) in the ab-plane (b) along the c-axis.

## 2. The phonon scattering rates

The scattering matrix elements,  $V_{\lambda\lambda'\lambda''}^{\pm}$ , can be expressed as<sup>5</sup>

$$V_{\lambda\lambda'\lambda''}^{\pm} = \sum_{i \in \text{u.c.}} \sum_{j,k} \sum_{\alpha\beta\gamma} \Phi_{ijk}^{\alpha\beta\gamma} \frac{e_{\lambda}^{\alpha}(i) e_{\lambda'}^{\beta}(j) e_{\lambda''}^{\gamma}(k)}{\sqrt{M_i M_j M_k}} \quad (\text{S4})$$

, which depends on the normalized eigenfunctions  $e_{p,q}$  of the three phonons involved and on the

anharmonic interatomic force constants (IFCs)  $\Phi_{ijk}^{\alpha\beta\gamma} = \frac{\partial^3 E}{\partial r_i^{\alpha} \partial r_j^{\beta} \partial r_k^{\gamma}}$ . In these equations, i, j, and k

denote atomic indices while  $\alpha$ ,  $\beta$ , and  $\gamma$  are Cartesian coordinates. In the sums, i is the atoms in the central unit cell, but j and k cover the whole system.  $r_i^{\alpha}$  and  $M_i$  denote the  $\alpha$  component of the displacement from the equilibrium position and the mass of the  $i$  th atom.  $e_{\lambda}^{\alpha}(i)$  is the  $\alpha$  component of the eigen function of mode  $\lambda$  at the  $i$  th atom.

The three phonon scattering rates,  $\Gamma_{\pm \lambda \lambda' \lambda''}$ , using the linearized BTE, can be expressed as<sup>5</sup>

$$\Gamma_{\lambda\lambda'\lambda''}^{+} = \frac{\hbar\pi}{4} \frac{f_0' - f_0''}{\omega_{\lambda} \omega_{\lambda'} \omega_{\lambda''}} |V_{\lambda\lambda'\lambda''}^{+}| \delta(\omega_{\lambda} + \omega_{\lambda'} - \omega_{\lambda''}) \quad (\text{S5})$$

$$\Gamma_{\lambda\lambda'\lambda''}^{-} = \frac{\hbar\pi}{4} \frac{f_0' + f_0'' + 1}{\omega_{\lambda} \omega_{\lambda'} \omega_{\lambda''}} |V_{\lambda\lambda'\lambda''}^{-}| \delta(\omega_{\lambda} + \omega_{\lambda'} - \omega_{\lambda''}) \quad (\text{S6})$$

, where  $f_0$  is  $f_0(\omega_{\lambda})$ .  $\Gamma_{+ \lambda \lambda' \lambda''}$  is the absorption process which leads to one phonon with the combined energy of two incident phonons ( $\omega_{\lambda} + \omega_{\lambda'} = \omega_{\lambda''}$ ).  $\Gamma_{- \lambda \lambda' \lambda''}$  is the emission process where the energy of one incident phonon is split among two phonons ( $\omega_{\lambda} = \omega_{\lambda'} + \omega_{\lambda''}$ ). The Dirac delta distribution in the above equations preserves the conservation of energy in the absorption and emission processes. From Eqs. S4, S5, and S6, we can predict that the phonon

lifetime is proportional to the square root of the atomic mass ( $\tau \sim \sqrt{(M_i M_j M_k)}$ ) because of  $\tau \sim 1/\Gamma$ .

### References

- 1 J. Turney, E. Landry, A. McGaughey, and C. Amon, Physical Review B 79, 064301 (2009).
- 2 L. Xiong, X. Chen, N. Zhang, D. McDowell, and Y. Chen, Archive of Applied Mechanics 84 (2014).
- 3 A. McGaughey and J. M. Larkin, Ann. Rev. Heat Transfer 17, 49 (2014).
- 4 X. Qian, X. Gu, M. S. Dresselhaus, and R. Yang, The Journal of Physical Chemistry Letters 7, 4744 (2016).
- 5 W. Li, J. Carrete, N. A. Katcho, and N. Mingo, Computer Physics Communications 185, 1747 (2014).